eXPRESS Polymer Letters Vol.5, No.11 (2011) 936
Available online at www.expresspolymlett.com
DOI: 10.3144/expresspolymlett.2011.91

Editorial corner – a personal view
Polyolefins for the 21st century

*M. Gahleitner**

Borealis Polyolefine GmbH, Innovation Headquarters, St. Peterstr. 25, 4021 Linz, Austria

After some decades of success, polymers have been going through a hard time recently. For the first time since the oil crisis of the early 1970s, global production decreased in 2008 as a result of the economic crisis. At the same time, public perception of 'plastics' deteriorated, with critical views on issues like the release of endocrine disruptors, littering and waste.

While some of these arguments may be justified, many remain superficial like the quarrel about single-use plastic shopping bags, where a total ban in Italy was the latest important news. The efficiency of these polyethylene (PE) bags is high in one-way systems already: In Austria, the amount of bags used per capita and year equals the energy content of just 0.7 litres of diesel fuel. In practice many of these bags are being re-used, and a comparably strong paper bag would have to be re-used about ten times more often to arrive at the same ecological footprint.

But polyolefins can do far more, in terms of lifetime, performance and energy efficiency. Bimodal high and medium density PE grades have revolutionized the water and gas distribution system, being light, corrosion-resistant and the safest choice in case of earthquakes. 'Smart' electrical power grids allowing the increased use of renewable energy sources call for high-performance insulation systems, and crosslinked LDPE will remain the material of choice. Efficient individual mobility requires cars combining low weight and high passenger safety, and only polymers will be able to fulfil that need at reasonable cost, with high-impact polypropylene (PP) copolymers at the frontline of development.

And polyolefins have certainly not reached their theoretical performance limit yet. Through continued research on the structure-property relations governing the performance of PP and PE, researchers in academia and industry contribute to a continuous expansion of the application range. Recent examples of previously impossible applications are replacement of glass-fibre reinforced polyamide for air-intake manifolds in cars by an advanced PP grade, and substitution of plasticized poly(vinyl chloride) (PVC) by advanced super-soft PP grades for medical applications. While future achievements will depend upon the availability of new catalyst generations giving better control over molecular weight distribution and comonomer incorporation, developments in processing technology will support this advance.

In 2008, 46% of the plastics processed in Europe were polyolefins, corresponding to a volume of 22.3 Mt/a. About 6% of the total crude oil consumption is employed for polymer production – and, from an efficiency perspective, that is a far better idea than just refining and burning the oil. While adaptation to new resources will be required in the long run, it remains to be seen whether bio-based and biodegradable polymers can challenge polyolefins for major market shares, given the mechanical and optical limitations exhibited by these materials so far.

Dr. Markus Gahleitner
Member of International Advisory Board

*Corresponding author, e-mail: markus.gahleitner@borealisgroup.com

eXPRESS Polymer Letters Vol.5, No.11 (2011) 937–949
Available online at www.expresspolymlett.com
DOI: 10.3144/expresspolymlett.2011.92

Modification of poly(lactic acid)/poly(propylene carbonate) blends through melt compounding with maleic anhydride

*M. Yao, H. Deng, F. Mai, K. Wang, Q. Zhang, F. Chen, Q. Fu**

College of Polymer Science and Engineering, State Key Laboratory of Polymer Materials Engineering, Sichuan University, Chengdu 610065, China

Received 18 February 2011; accepted in revised form 5 May 2011

Abstract. Maleic anhydride (MA) is incorporated into poly(lactic acid) (PLA)/poly(propylene carbonate) (PPC) blends to modify its properties through melt compounding. It is interesting to note that the toughness of PLA/PPC blends can be improved by 1355% while the strength is almost kept constant by adding very low content (as low as 0.9%) of MA into the blends. However, higher MA content in the blends leads to decrease in strength and further increase in toughness indicating an obvious plasticizing effect, while MA is shown to have no effect on the toughness of neat PLA. Rheological, scanning electron microscopy (SEM) and dynamic mechanical analysis (DMA) studies have been carried out to understand the above results. It is believed that the improvement in mechanical performance originated from the largely retained molecular weight of PPC and improved interfacial interaction after processing. And relative large amount of MA in the blends is shown to mainly plasticize the PPC phase rather than the PLA phase. Such an effective method could provide PLA based biodegradable polymer blends with novel properties for industrial applications.

Keywords: *biodegradable polymers, melt compounding, mechanical properties, poly(lactic acid), poly(propylene carbonate)*

1. Introduction

Poly(lactic acid) (PLA) is an example of a promising biopolymer prepared through a combination of biotechnology and chemistry. It is prepared from 100% renewable resources such as corn, sugar beets or rice [1, 2]. PLA degrades biologically into lactic acid, a product of the carbohydrate metabolism. Thanks to its biocompatibility, PLA is suitable for sutures [3, 4], drug delivery systems [5, 6], scaffold material [7], and implants for bone fixation [8, 9]. It offers a potential alternative to petrochemical plastics for many applications, partially because of its high strength and stiffness. However, its toughness is not satisfactory. Blending PLA with other polymers presents a practical and economic measure to obtain toughened products [10]. To retain the integrity of biodegradability, blending PLA with other biodegradable polymers is particularly interesting. PLA/poly(ε-caprolactone) (PCL) blends have been extensively studied and have shown greatly improved mechanical properties compared to neat PLA [11–13]. Previous researchers also have shown that the addition of plasticizers such as polyethylene glycol (PEG), glucosemonoesters, poly(vinyl acetate) and partial fatty acid esters successfully overcame the brittleness and widened the application of PLA [14–16]. Jacobsen and Fritz [14] revealed that plasticization played an important role in improving the elongation at break and impact strength of PLA.

Poly(propylene carbonate) (PPC) is a new thermoplastic polymer derived from carbon dioxide and propylene oxide [17]. It is also a biodegradable polymer, many studies concentrated on the biodegradability, we know the molecular weight would

*Corresponding author, e-mail: quiangfu@scu.edu.cn

decrease in specific solutions [18]. It has interesting physical and chemical properties, being an attractive green environmental material for many applications [19–22]. It can be used in adhesives, solid electrolytes, polyols, photoresists, propellants, barrier materials, flexibilizers and plasticizers. The ester units provide PPC with chain flexibility and good melt flow characteristics. Although PPC can be melt processed, its poor thermal stability has limited its application. Many efforts have been devoted to improve the thermal stability of the PPC [23–25]. Tao *et al*. [25] prepared UV-crosslinkable PPC through terpolymerization of CO_2, propylene oxide (PO), and allyl glycidyl ether (AGE). The crosslinked PPC showed obvious improvement in thermal and mechanical properties in comparison with pure PPC. However, its preparation process is very complicated.

Furthermore, PPC is an amorphous polymer, with about 40–50% of units in the PPC copolymer chain being carbonate. Recently, some efforts have been invested to apply PPC as plasticizer for rubber or thermoplastics, and surfactant [26–29]. PPC is an amorphous polymer with a chemical structure similar with PLA. In the study reported by Ma *et al*. [30], the compatibility of melt-mixed blends of PLA/PPC in different ratios was characterized. They illustrated that PLA and PPC are partially miscible and compatible to some extent due to their similarity in chemical structure. However, they reported that more than 40 wt% of PPC are needed in the PLA to modify its brittle fracture behavior. As a result, the strength of the blends is largely affected by the large content of PPC. Inevitably, the process-ability of the blends containing large content of PPC is quite poor due to the poor thermal stability of PPC.

The blend of PLA and PPC is a biodegradable polymer system, and it has potential as medical and packing materials. In our previous work, it was demonstrated that the mechanical and thermal properties of PPC can be improved dramatically through end-capping PPC with MA [31]. In this article, MA will be added to the binary blend of PLA and PPC to further improve the properties.

To the best of our knowledge, no systematic study has been reported so far to investigate the properties of MA end-capped PPC toughened PLA composites. Therefore, it is the aim of this study to investigate the effect of MA content on the mechanical, thermal and rheological properties of PLA/MA/PPC blends. The weight ratio between PLA and PPC ranges from 90:10 to 10:90, and the weight percentage of the MA was varied from 0 to 1.5 wt% of the total weight of the PLA/PPC blends. Scanning electron microscopy (SEM), Differential Scanning Calorimetry (DSC), Dynamic mechanical analysis (DMA), Gel permeation chromatography (GPC), tensile test and rheological study are carried out on these blends to perform systematic investigation. It is proposed that part of the MA is end-caped onto PPC, and the rest is present as a blend. Furthermore, possible homopolymerization of MA is also suggested.

2. Experimental

2.1. Materials

1. PLA is provided by Zhejiang Haizheng Biomaterial Co (Zhejiang, China). It is levorotatory, represents a semi-crystalline and biodegradability. Its GPC measured weight-average molecular weight is $1.59 \cdot 10^5$ g/mol, and $M_w/M_n = 2.75$. PPC is obtained from State Key Polymer Physics and Chemistry Laboratory, Changchun Institute of Applied Chemistry, China. Its weight-average molecular weight is $2.48 \cdot 10^5$ g/mol, and $M_w/M_n = 3.2$. MA (purity > 99.5 wt%) was purchased from Tianjin Bodi Chemical Co (Tianjin, China).

2.2. Preparation of PLA/PPC and PLA/MA/PPC blend

Blends containing PLA and PPC in the ratio of 90/10, 70/30, 50/50, 30/70, and blends containing PLA, MA and PPC with the ratio of 70/0/30, 70/0.15/30, 70/0.3/30, 70/0.6/30, 70/0.9/30, 70/1.5/30, 10/0.3/90, 30/0.3/70, 50/0.3/50, 70/0.3/30 and 90/0.3/10 were melt compounded using a Haake Rheomix internal mixer (Thermo Fisher Scientific, Waltham, MA, USA) at a barrel temperature of 150°C and a rotation speed of 50 rpm for 5 mins, respectively. PLA, PPC and MA were dried at 50°C overnight before the melt blending to prevent PLA and PPC from hydrolysis during blending. Then, PLA/MA/ PPC blends were ground into fine particles for further sample preparation. All specimens used were manufactured with a hot compression molding method. It was conducted at 160°C for 6 mins, with a holding pressure of 10 MPa.

2.3. Characterizations

2.3.1. Mechanical testing

Tensile properties were characterized with Universal Testing Machine (SANS company, Shenzhen, China) in tension mode. Specimens used for tensile test were cut from hot pressed films of PLA/MA/PPC. And the sample dimension was 4 mm in width, 0.4–0.5 mm in thickness and 75 mm in length. They are slabs with dog bone shapes. Five samples were used for each measurement and averaged results are reported. The cross-head speed used was 10 mm/min.

2.3.2. Gel permeation chromatography (GPC)

The molecular weight (M_w) and molecular weight distribution (MWD) of the blends were measured with gel permeation chromatography system (GPC, agilent1100, Agilent Technologies, Santal Clara, CA, USA) with tetrahydrofuran (THF) as solvent. Calibration was performed with polystyrene standards.

2.3.3. Scanning electron microscopy (SEM)

The morphologies of etched specimens and tensile fractured surfaces were examined under an acceleration voltage of 20 kV with SEM (JEOL JSM-5900 LV, Jeol, Tokyo, Japan). Prior to examination, the specimens of blends were cryogenically fractured in liquid nitrogen, then the fracture surfaces were etched with the acetone/ethanol (1:1) mixed solution to remove PPC and MA. For the tensile fractured specimens, a thin layer of gold was coated on their fracture surfaces before examination.

2.3.4. Dynamic mechanical analysis (DMA)

Dynamic mechanical properties of the prepared composites (storage modulus and tan) were characterized with DMA (Q800, TA Instruments, New Castle, DE, USA) in tension mode. Temperature scan was conducted from –20 to 120°C at a heating rate of 3°C/min. A fixed frequency of 1 Hz was used. A static force of 0.01 N and the force track of 120.0% were employed. The film was cut into the plates for DMA test. And the sample dimension of the film was 4 mm in width, 0.4–0.5 mm in thickness and 14–18 mm in length.

2.3.5. Differential scanning calorimetry (DSC)

A DSC (Perkin-Elmer Pyris I, Perkin Elmer Corp. Waltham, MA, USA) with nitrogen as the purge gas was used to investigate the melting and crystallization behaviors of the blends. The mass of tested sample was around 5 mg. The sample was heated from room temperature to 200°C at a heating rate of 10°C/min. This first heating process was regarded as melting scan for the analysis. The crystallization and melting temperatures were determined as the temperatures at the maximum values of crystallization and melting peaks.

2.3.6. Rheological measurement

Oscillatory shear measurements in the linear viscoelastic region were performed on a Gemini 200 dynamic rheometer (Malvern Instruments Ltd, Malvern, UK) using 2.5 cm diameter and 1.2 mm distance parallel plates at 160°C. Dynamic frequency sweep was performed in the region of linear viscoelastic response (LVR), with 1% strain for the blends, starting from high frequency, 100 down to 0.01 rad/s. Dynamic frequency sweep tests were subsequently performed to determine the dynamic properties of the materials. Test sample disks with a thickness of 1.5 mm and a diameter of 2.5 mm were prepared by compression molding at 160°C.

3. Results and discussion

3.1. Mechanical properties

Mechanical test was performed to investigate the mechanical performance of PLA and blends. Neat PLA exhibits yielding with a short quasi constant stress regime, and fails at a strain around 3.6% (see Figure 1a). It is noted that all the neat PLA specimens fractures without necking. In the binary PLA/PPC blends, the strain at break is increased from 10.1 to 82% with PPC content increasing from 10 to 70%. However, the tensile strength is decreasing with increasing PPC loading, and the blends fracture in an almost brittle manner without yielding, except the one containing 70% PPC. This is slightly different from the work reported by Ma *et al.* [30], as the strain at break is much smaller in the current work. It might be caused by the difference in the neat PLA used. For PLA/MA/PPC blends containing the same amount of MA (see Figure 1b), the

elongation at break is obviously improved comparing with their original binary blends, respectively. Nevertheless, their strength is almost the same with the previous values (see Figure 2a).

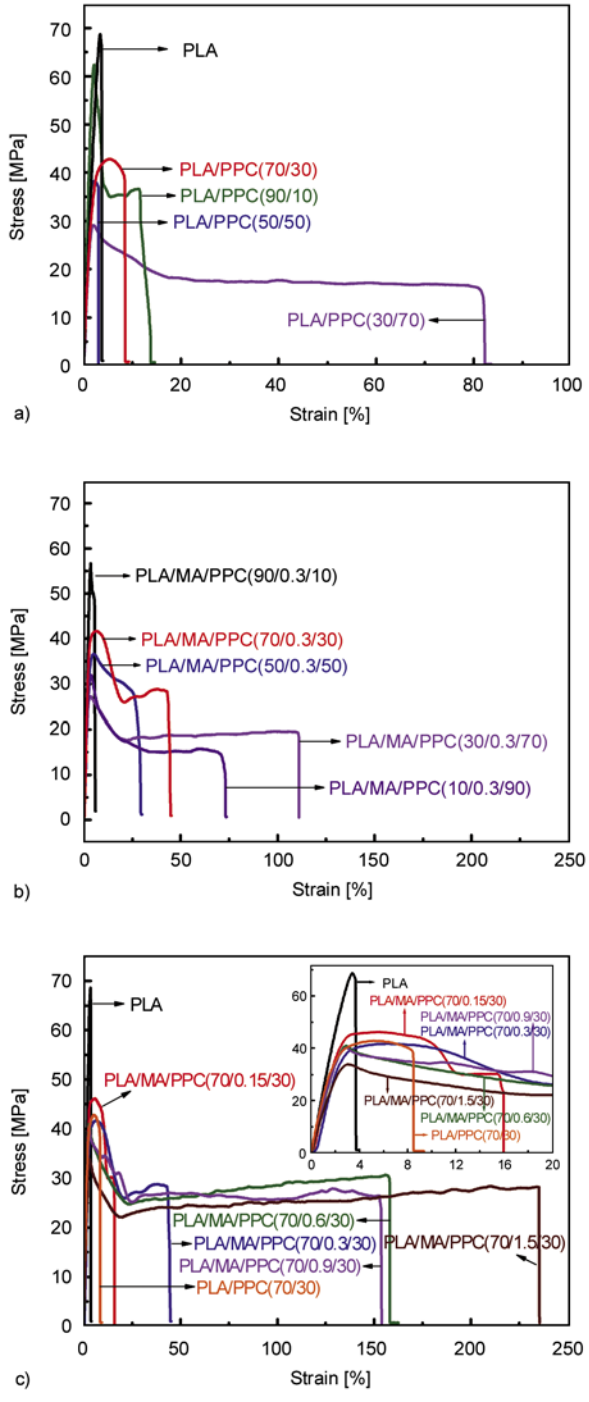

Figure 1. Stress–strain curves for (a) PLA, PLA/PPC blends in the ratio of 90/10, 70/30, 50/50 and 30/70, (b) PLA/MA/PPC blends in the ratio of 90/0.3/10, 70/0.3/30, 50/0.3/50, 30/0.3/70 and 10/0.3/90, (c) PLA/MA/PPC blends in the ratio of 70/0.15/30, 70/0.3/30, 70/0.6/30, 70/0.9/30 and 70/1.5/30

To investigate the effect of MA content on the properties of ternary blends, PLA/MA/PPC blends with PLA/PPC in the ratio of 70/30 containing different amount of MA is characterized (see Figure 2b). The addition of 0.15 wt% MA results in a slight increase in tensile strength compared with the PLA/PPC binary blend. Interestingly, the specimens show intense stress whitening followed by necking, resulting in a large yielding regime and hence slight increase in strain at break (20.4%). With the addition of 0.3, 0.6 and 0.9 wt% MA, the strain at break is dramatically increased to 59.3, 164.3 and 142.5%, respectively. Consequently, the toughness which are calculated from the definite integrals of the strain -stress curves is 1.5, 3.1, 5.8, 13.4, 44.7, 42.0 and 60.6 MJ/m^3 for neat PLA, PLA/PPC (70/30), PLA/MA/PPC (70/0.15/30), PLA/MA/PPC (70/0.3/30), PLA/MA/PPC (70/0.6/30), PLA/MA/PPC (70/0.9/30), PLA/MA/PPC (70/1.5/30), respectively. It is interesting to notice that the mechanical properties including toughness and strength is improved (8.2% increase in strength, 188.7% increase in toughness) by adding very low content (as low as 0.15%) of MA into the blends. While a maximum of 1961.2% increase in toughness is obtained for the blends containing 1.5% of MA. And the toughness can be improved by 1355% while the strength was almost kept constant by adding very low content (as low as 0.9%) of MA into the blends. All the PLA/MA/PPC blends yields with noted stress whitening across the whole gauge length accompanied with necking. However, there is little improvement in tensile strength compared with the binary blend.

Above results are summarized in Table 1, it can be concluded that the PLA/MA/PPC ternary blends experience significant necking. This indicates the presence of shear yielding. The improvement in toughness with additional MA shows the interface between PLA and PPC polymer chains may be effectively enhanced by end-capping MA onto PPC, MA can be grafted onto PPC molecules by reactive blending. The scheme is shown in Figure 3 [31]. Furthermore, the increased molecular weight of the PPC component (as discussed in our previous work [31]) could also be partially responsible for this significant increase in toughness, as more entanglements between polymer chains might be formed at higher molecular weight. Nevertheless, the tensile strength shows an obvious decrease with increasing

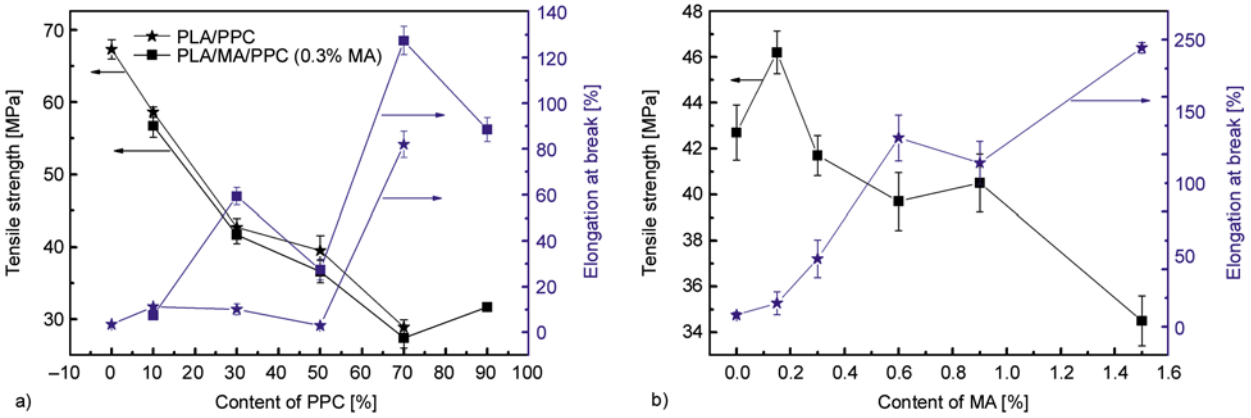

Figure 2. (a) Tensile strength and elongation at break of PLA/PPC, PLA/MA/PPC (0.3 phr MA is loaded) blends as a function of PPC content. (b) tensile strength and elongation at break of PLA/MA/PPC(PLA/PPC wt. ratio is 70/30) blends as a function of MA content.

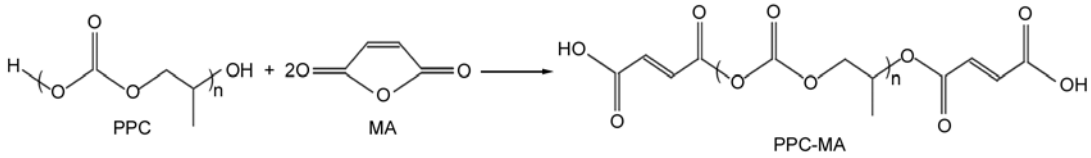

Figure 3. Melt end-capping PPC with MA

Table 1. Summary of mechanical properties of the specimens shown in Figure 1.

	Tensile strength [MPa]	Elongation at break [%]	Toughness [MJ/m^3]
PLA	67.3±1.33	3.6±0.31	1.5
PLA/PPC (90/10)	58.6±0.74	11.2±0.37	4.9
PLA/ PPC (70/30)	42.7±1.21	10.1±2.43	3.1
PLA/ PPC (50/50)	39.5±2.03	3 ±0.65	0.9
PLA/ PPC (30/70)	28.9±1.00	82±5.76	15.0
PLA/MA/PPC (90/0.3/10)	56.7±1.58	7.5±1.51	2.2
PLA/MA /PPC (70/0.3/30)	41.7±1.25	59.3±3.79	13.4
PLA/MA /PPC (50/0.3/50)	36.6±1.54	27.4±4.55	8.6
PLA/MA /PPC (30/0.3/70)	27.4±1.40	127.4±6.08	21.4
PLA/MA /PPC (10/0.3/90)	31.7±0.40	88.5±5.21	12.6
PLA/MA/PPC(70/0.15/30)	46.2±0.94	20.4±9.95	5.8
PLA/MA/PPC(70/0.3/30)	41.7±0.88	59.3±16.35	13.4
PLA/MA/PPC(70/0.6/30)	39.7±1.36	164.3±20.07	44.7
PLA/MA/PPC(70/0.9/30)	40.5±1.26	142.5±18.35	42.0
PLA/MA/PPC(70/1.5/30)	34.5±1.10	243.1±4.55	60.6

MA content. For the PLA/MA/PPC blends containing 1.5 wt% MA, the tensile yield strength is decreased dramatically, meanwhile the strain at break is significantly increased to 243.1%. The excess MA may act as plasticizer, which might be responsible for the decrease in strength and the increase in strain at break. In order to further investigate the effect of MA on the blends, PLA is compounded with different contents of MA. The mechanical properties of these compounds are summarized in Table 2. It is obvious to note that MA is not acting as plasticizer for neat PLA. The excess MA may only act as plasticizer to PPC component. As interesting behavior has been demonstrated by blends containing different amounts of MA, following characterization is mainly carried out to investigate the effect of MA content on different properties.

Table 2. mechanical properties of the PLA/MA blends with different content of MA

	Tensile strength [MPa]	Elongation at break [%]
PLA	67.3±1.33	3.6±0.31
PLA/MA (100/0.15)	65.39±2.69	3.8±0.39
PLA/MA (100/0.3)	61.72±4.58	3.6±0.70
PLA/MA (100/0.6)	54.22±3.82	3.5±0.33
PLA/MA (100/0.9)	62.65±1.45	3.7±0.29
PLA/MA (100/1.5)	61.88±1.49	3.7±0.45

3.2. GPC measurement

To understand the effect of processing and the addition of MA on the molecular weight of PPC and PLA, blends were studied by GPC measurements. The weight average molecular weight (M_w) and the molecular weight distribution (MWD) of PLA/PPC (70/30) and PLA/MA/PPC blends are summarized in Table 3. It is well known that the thermal degradation of PPC molecular chain is likely to occur during melt compounding [31]. However, M_w for PLA/MA/PPC (70/0.15/30, 70/0.3/30) is obviously higher than that of processed neat blends. This indicates that the addition of MA prevents the thermal degradation of PPC. As MA serves as end capping agent, which inhibits initial chain unzipping and prevents the thermal decomposition of PPC [32]. It is noted that the M_w is obviously decreasing with increasing more MA content (see the M_w for the blend PLA/MA/PPC (70/0.6/30, 70/0.9/30, 70/1.5/30)). It might be due to the fact that the end capping reaction is better performed at lower MA contents. Since the chance for homo-polymerization of MA increases with increasing MA content, which competes with end-capping reaction. This results in improvement in the molecular weight (especially for PLA/MA/PPC (70/1.5/30)), where the excessive MA could even promotes the degradation of the polymer during processing (in our previous work have proved it [31]).

3.3. Morphology analysis

To explore the mechanism for toughening observed in the blends, the morphology of tensile specimens and etched specimens were investigated with SEM. PLA/MA/PPC ternary blends with different content of MA and PLA/PPC (70/30) binary blend were selected to be investigated as shown in Figure 4 and 5.

It can be observed from the fractured surfaces of specimens taken from tensile test that a smooth surface without obvious plastic deformation is obtained in PLA/PPC (70/30) (Figure 4a). It clearly reveals that some PPC spheres remains at the fracture surface. This indicates that the weak interfacial adhesion associated with the incompatibility in PLA/PPC blend. The applied stress could not be efficiently transferred through the interface between polymers, which in turn result in a limited improvement in mechanical properties. The morphology of the tensile fractured surface from PLA/MA/PPC (70/0.9/30) ternary blend is distinctly different from binary blend, exhibiting considerable ductile behavior. In Figure 1c, PLA/MA/PPC (70/0.9/30) demonstrates necking behavior and a large strain at break

Table 3. The weight average molecular weight (M_w), distributing index (D) of PLA/PPC and PLA/MAPPC blends

	PLA/PPC (70/30)	PLA/MA/PPC (70/0.15/30)	PLA/MA/PPC (70/0.3/30)	PLA/MA/PPC (70/0.6/30)	PLA/MA/PPC (70/0.9/30)	PLA/MA/PPC (70/1.5/30)
M_w	$4.67 \cdot 10^4$	$5.45 \cdot 10^4$	$6.17 \cdot 10^4$	$5.20 \cdot 10^4$	$4.61 \cdot 10^4$	$3.88 \cdot 10^4$
D	2.35	2.35	2.18	2.19	2.33	2.56

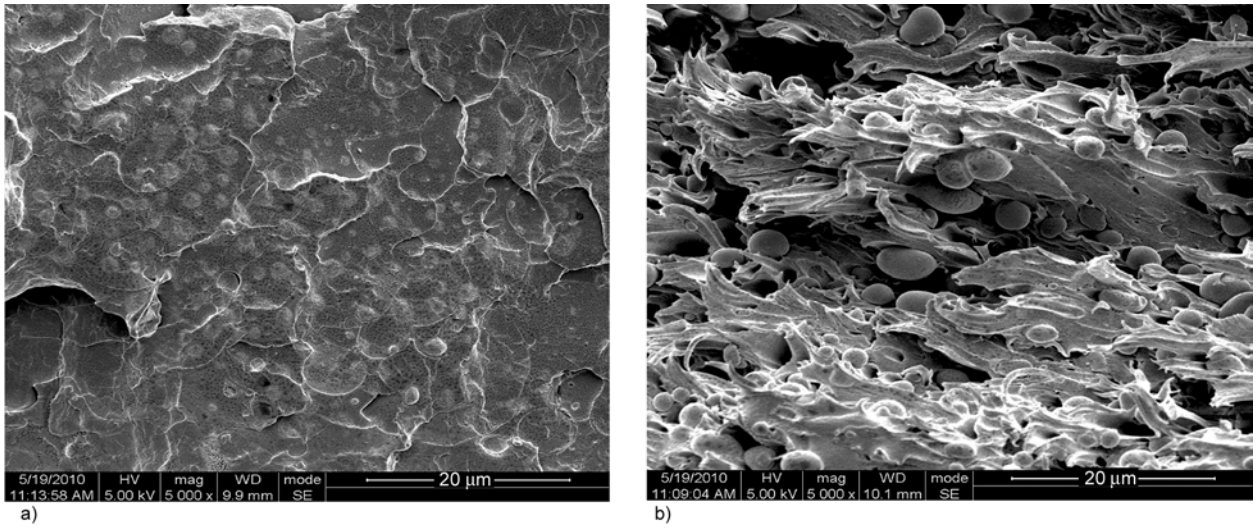

Figure 4. Tensile-fractured surface morphology of the blends: (a) PLA/PPC (70/30), 5000×; (b) PLA/MA/PPC (70/0.9/30), 5000×

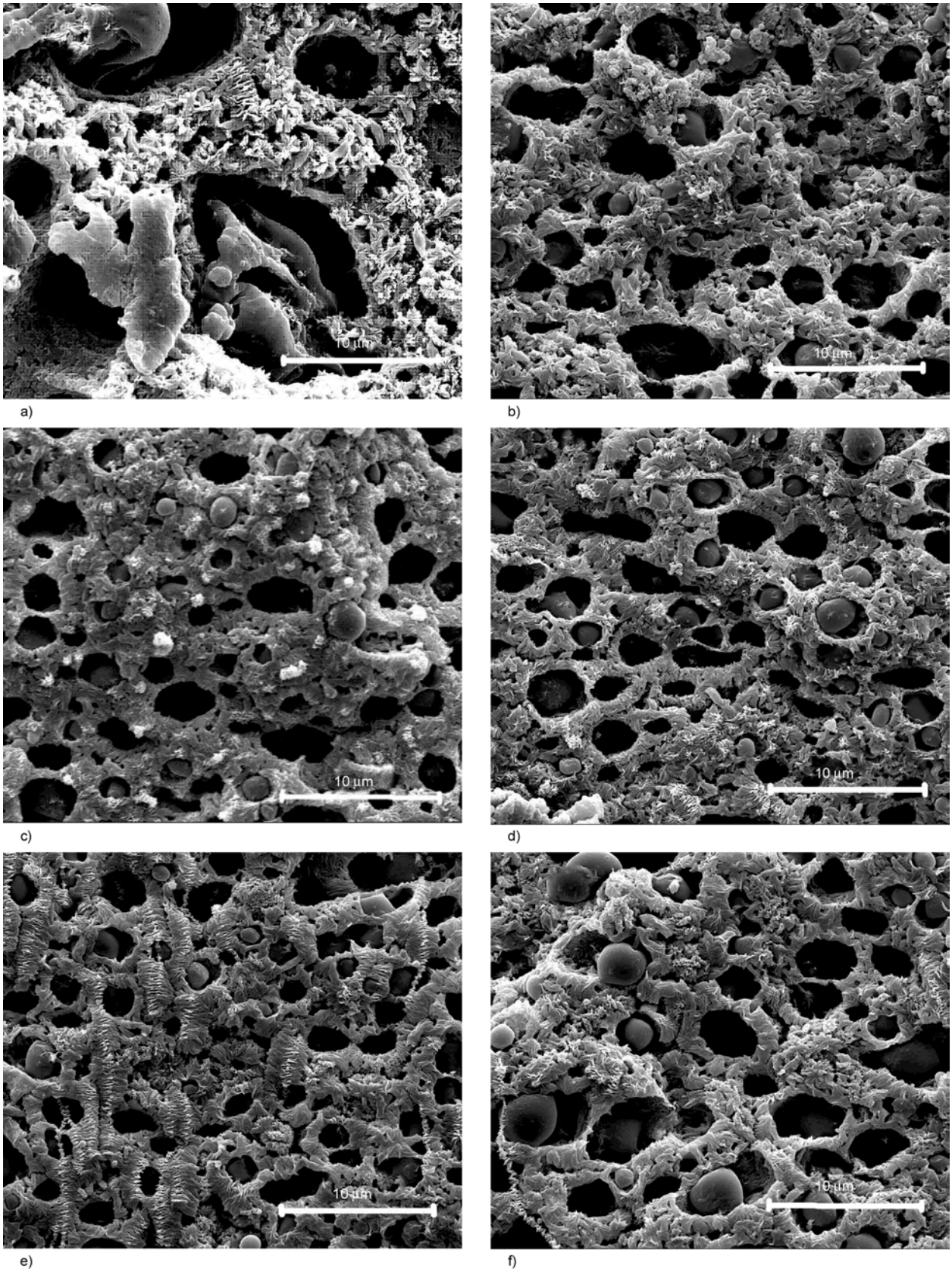

Figure 5. SEM micrographs of the surfaces of PLA/PPC (70/30 w/w) blends with varying MA contents. The surfaces were prepared by etched with the acetone/ethanol (1:1) mixed solution to remove PPC and MA. (a) PLA/PPC (70/30), (b) PLA/MA/PPC (70/0.15/30), (c) PLA/MA/PPC (70/0.3/30), (d) PLA/MA/PPC (70/0.6/30), (e) PLA/MA/PPC (70/0.9/30), (f) PLA/MA/PPC (70/1.5/30).

value. Correspondingly, its SEM micrograph exhibits intensive plastic deformation (Figure 4b), indicating the presence of large deformation in the blend. The rough fracture surface suggesting that the cracking propagation absorbs considerable amount of strain energy before failure [33]. And the addition of MA increases the interfacial adhesion between PLA and PPC components, leading to a significant improvement in toughness.

PPC component is etched out to investigate the phase morphology in the blends as shown in Figure 5. The size of PPC component is quite large for the binary blend (see Figure 5a). It decreases with the addition of MA, indicating the compatibility between PPC and PLA is improved. With further increase in MA content, the size of the PPC component is almost kept constant (see Figure 5b–f), indicating only a small amount of MA is needed to achieve compatibilization.

3.4. Dynamic mechanical analysis

DMA study was carried out to study the thermal mechanical properties and glass transition temperature of these blends. Figure 6a shows the dynamic storage modulus (E') of neat PLA matrix, PLA/PPC and PLA/MA/PPC blends over a temperature range of -20–80°C. The storage modulus (E') is plotted against temperature. For most samples, a decrease in E' can be observed for the investigated temperature range comparing with that of neat PLA, indicating elastic properties is reduced by additional PPC. All samples lost most of their stiffness at temperatures above their T_g. The stiffness of blends and pure polymers below T_g is governed by the glassy phase, where polymer chain movement is restricted. Above 60°C, the E' curves for the blends display a short plateau comparing with pure PLA. This indicates a decrease in thermal-mechanical stability with additional PPC in PLA. The addition of impact modifier and plasticizer in PLA is often reported to decrease the stiffness, where a dramatic decrease in E' of PLA is noted with the addition of polyethylene glycol (PEG) as plasticizer [34]. Comparing PLA/PPC with PLA/MA/PPC, the storage modulus gradually decreases with further increasing MA content. Accordingly, the temperatures corresponding to a relative modulus (the ratio of storage modulus to initial modulus) of 0.8 are 34.7, 34.7, 34.7, 31.7, 28.8 and 26.1°C (Figure 6b) for PLA/PPC, PLA/MA/PPC (30/0.15/70, 30/0.3/70, 30/0.6/70, 30/0.9/70, 30/1.5/70), respectively. This indicates that the

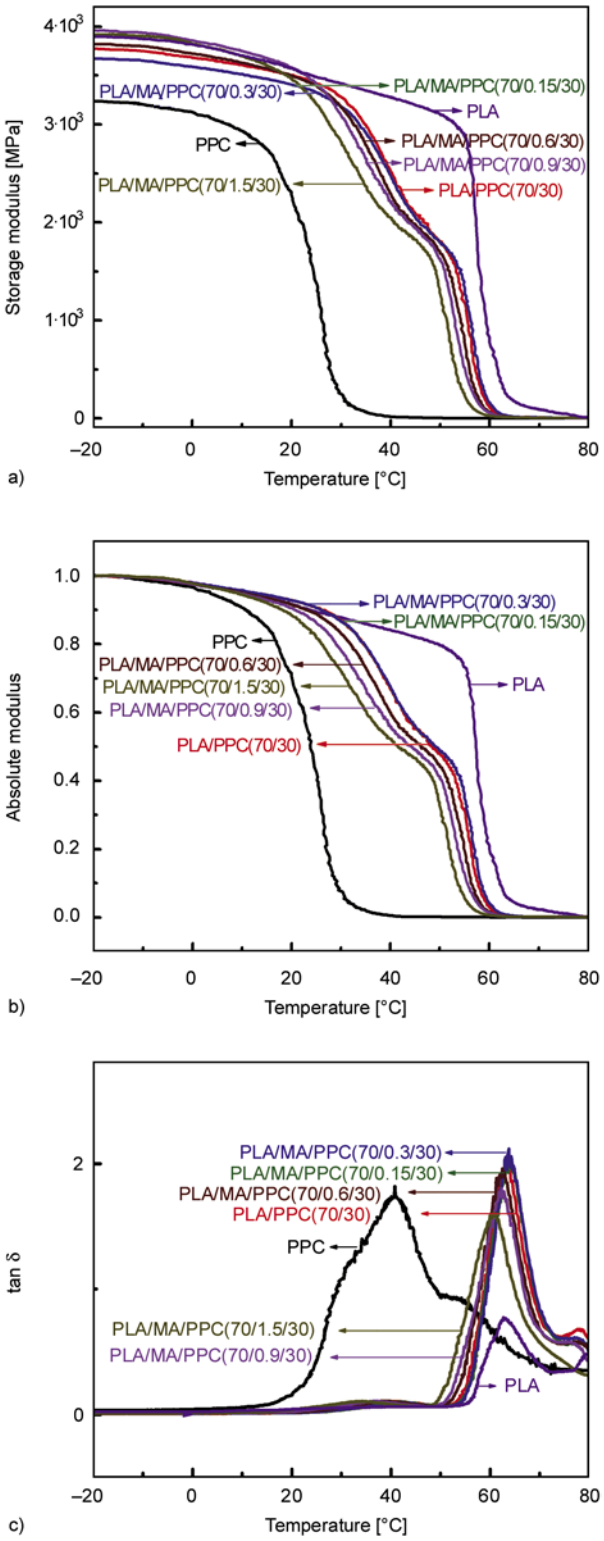

Figure 6. DMA curves including (a) storage modulus, (b) ralative modulus (the ratio of storage modulus to initial modulus) and (c) tanδ as a function of temperature for PPC, PLA, PLA/PPC (70/30) and PLA/MA/PPC blends with different MA content

stiffness of PLA/MA/PPC blends is decreasing with the addition of large amount of MA. This result agrees well with the above results from mechanical test.

Figure 6c shows tanδ as a function of temperature for the pure polymer, PLA/PPC and PLA/MA/PPC blends. Two relaxation peaks, *a* and *a'* corresponding to T_{g1} of the PPC-rich phase and T_{g2} of the PLA-rich, respectively, are observed in each tanδ curve. T_{g1} and T_{g2} are summarized in Table 4. For PLA/PPC (70/30) and PLA/MA/PPC (70/0.15/30, 70/0.3/30), the tanδ peak is shifted to slightly higher temperatures comparing with pure polymers. T_g is shifted to lower temperatures with further increasing MA content. This may be due to the fact that excessive MA serve as plasticizer. However, T_{g1} decreases from 41 to 33.6°C, showing a much larger drop than T_{g2} (which decreases only 3°C). It indicates that most of the excessive MA mainly plasticize PPC phase. In the blends, the plasticized PPC plasticize PLA phase. This agrees well with the mechanical behavior observed in Figure 1 and Table 2. Furthermore, no improvement in toughness is observed while MA is added into neat PLA (see Table 2). Therefore, it is concluded that most of the excessive MA mainly plasticize PPC phase as the toughness of the blends is significantly improved with the addition of MA.

We know that, if the blends is completely compatible, the T_g calculated from the compositions by applying Fox's equation is 55.96°C, when the T_{g1} and T_{g2} close to it, indicate the compatibility is improved [17]. As shown in Table 4, only for the PLA/MA/PPC (70/0.15/30) blend have the trend that T_g close to each other comparing with neat binary blend, and the T_{g1} corresponding to the PPC-rich phase increase suggesting that the blend is partially miscible. This result agrees well with the above mechanical property result, where the tensile strength and elongation at break for PLA/MA/PPC (70/0.15/30) is increased. In addition, the T_g for other blends move farther indicating the poorer compatibility is obtained while more MA is added. As a result, decreasing tensile strength is obtained with increasing MA content.

3.5. Differential scanning calorimetry

To further understand the mechanical behavior observed, DSC was carried out to investigate the melting and crystallization behavior of these blends. Figure 7 shows the DSC results of PLA binary and ternary blends from the first heat scan at a rate of

Table 4. The T_{g1} for PPC, T_{g2} for PLA obtained from the tanδ curve of PPC, PLA, PLA/PPC (70/30) and PLA/MA/PPC blends with different MA content

	PLA	PPC	PLA/PPC (70/30)	PLA/MA/PPC (70/0.15/30)	PLA/MA/PPC (70/0.3/30)	PLA/MA/PPC (70/0.6/30)	PLA/MA/PPC (70/0.9/30)	PLA/MA/PPC (70/1.5/30)
T_{g1} [°C]		40.7±0.2	41.0±0.2	41.9±0.2	41.4±0.2	38.9±0.2	37.0±0.2	33.6±0.2
T_{g2} [°C]	62.5±0.2		63.6±0.2	63.7±0.2	63.7±0.2	62.3±0.2	62.3±0.2	60.7±0.2

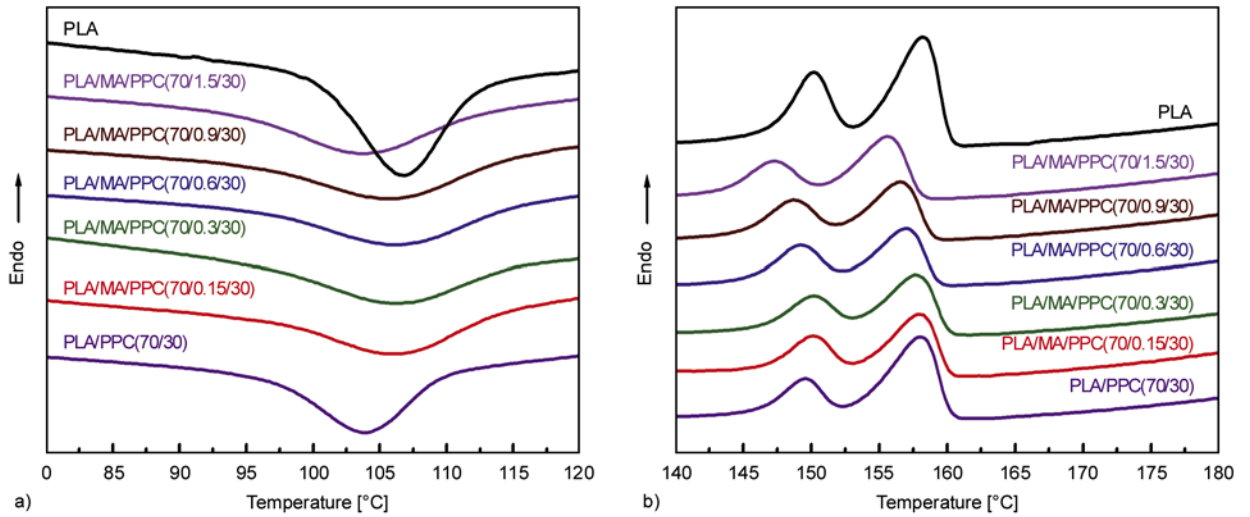

Figure 7. DSC traces of the PLA, PLA/PPC (70/30) and PLA/MA/PPC (70/0.15/30, 70/0.3/30, 70/0.6/30, 70/0.9/30, 70/1.5/30) blends at a heating rate of 10°C/min

10°C/min. The exothermic peaks can be correlated to the crystallization of PLA due to the amorphous nature of PPC and semi-crystalline nature of PLA. As the processed PLA is heated upon testing, some of the molecular chains in the amorphous regions gain enough mobility to rearrange into an ordered crystalline phase, giving out energy and forming an exothermic re-crystallization peak. In Figure 7a the cold crystallization temperature (106.7°C) of the neat PLA is clearly decreased with the incorporation of PPC, the reason may be the presence of PPC increase the mobility of PLA chains. The presence of PPC result in a lower cold crystallization temperature (T_c) without additional MA. This could be caused by the increased number of low molecular polymer arising from the decomposition of PPC [35]. For the blends, the decomposition of PPC is largely avoided during processing thanks to the addition of MA. Therefore, the T_c observed for the blends is higher than that of neat binary blend.

In Figure 7b, neat PLA shows a melting peak at 150.1°C (T_{m1}) and 158.3°C (T_{m2}). The increase in additional MA content gradually decreases the melting temperature. This bimodal melting peak is induced during slow DSC scan while the less perfect crystals have enough time to be melted and reorganized into crystals with higher structural perfection, and re-melted at higher temperature [36, 37]. Low-melting-temperature crystals have similar structure with high-melting-temperature ones, but with smaller lamellar thickness. For PLA/PPC binary blend, the decrease in the first peak temperatures (T_{m1}) suggesting larger number of less perfect crystals are nucleated at the particle surface. They are reorganized into a more stable form at higher temperature (T_{m2}) and melted again at around the same temperature. By comparing PLA/PPC (70/30) with PLA, the melting enthalpy of these is almost the same. This suggests that the amorphous PPC has no apparent effect on the crystallinity. For PLA/MA/PPC (70/0.15/30, 70/0.3/30, 70/0.6/30, 70/0.9/30), T_{m1} is kept almost constant, but T_{m2} is decreased due to the crystallization of perfect PLA crystalline is hindered by high molecule weight PPC component. With increasing MA content, a decrease in melting temperature is observed. This agrees with above results that excessive MA serves as plasticizer in the blends.

3.6. Rheological properties

The rheological properties of the blends are investigated in this study to understand the properties variations shown in Figure 1c. As shown in Figure 8, the shear storage moduli (G'), shear loss moduli (G''), and complex viscosities (η^*) are plotted versus the applied shear frequency, respectively. All

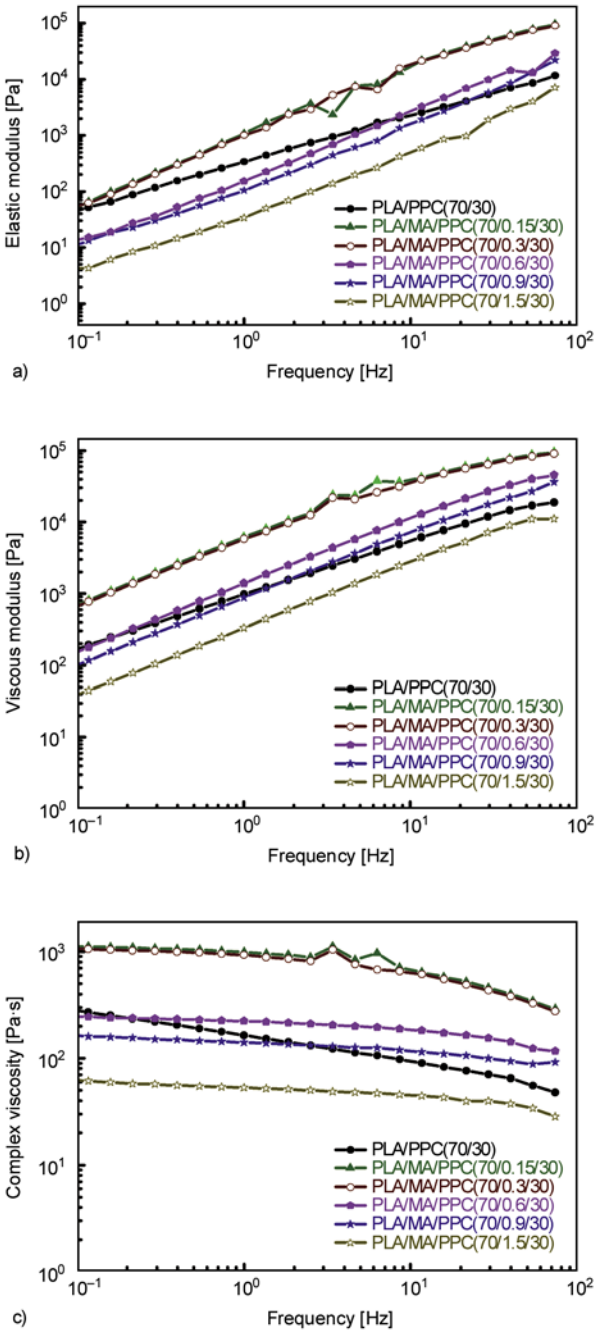

Figure 8. (a) storage modulus (G'); (b) loss modulus (G''); (c) complex viscosity (η^*) versus frequency for the PLA/PPC (70/30) and PLA/MA/PPC (70/0.15/30, 70/0.3/30, 70/0.6/30, 70/0.9/30, 70/1.5/30) blends

the samples are featured by a typical increase in G' and G'' with increasing frequency (ω). At the frequency scanned area for all the samples the G' is smaller than G'', indicating a classical liquid-like behavior of polymer melt.

The complex viscosities of the PLA/MA/PPC (70/0.6/30, 70/0.9/30, 70/1.5/30) blends exhibit a Newtonian behavior (η^* is independent of frequency) with values around 250, 170 and 60 Pa·s, respectively. Then, a shear-thinning takes place at frequency above 30 rad/s. In Figure 8, the increase in moduli and viscosity obtained for PLA/MA/PPC (70/0.15/30, 70/0.3/30) demonstrates the reinforcing effect from additional MA on the polymer melt. It is thought that such an effect originates from the higher molecular weight of PPC and better interfacial adhesion in these specimens. Furthermore, the lowest moduli and viscosity is obtained for PLA/MA/PPC (70/1.5/30). This agrees well with the results observed above as excessive MA serve as plasticizer in the system. It is also interesting to note that neat binary blend is demonstrating stronger shear thinning effect comparing with other blends, especially the ones containing higher MA content. It is reported in literature that low molecular weight polymer shows Newtonian-like behavior at shear rates similar with film extrusion [38]. Therefore, such an effect is likely caused by the presence of low molecular PPC chains which come from the decomposition of PPC.

4. Conclusions

In order to improve the mechanical performance of PLA, PPC and MA is melt compounded with PLA. The PLA/MA/PPC blends yield with noted stress whitening across the whole gauge length accompanied with necking with the addition of MA. The strain-at-break is dramatically increased comparing with PLA/PPC binary blend. It is interesting to note that the toughness can be improved by 1355% while the strength is almost kept constant by adding very low content (as low as 0.9%) of MA into the blends. DMA study shows that the T_g of PPC and PLA decrease with the addition of relative large amount of MA, indicating the plasticizing effect of MA in the blends. However, the magnitude of such a decrease is more pronounced in PPC. By considering the results from both mechanical test and DMA, it is believed that MA mainly plasticize PPC component in the blends. SEM results indicate that the addition of MA increases the interfacial adhesion between PLA and PPC phases, leading to ductile fracture behavior and decrease in the size of PPC domain. Rheological analysis demonstrates that the viscosity is increased by adding small amount of MA into the polymer melt. Such an increase is thought to be caused by the largely retained molecular weight of PPC during processing and improved interfacial adhesion between PLA and PPC phases. As a result, enhanced mechanical properties for PLA/PPC blends are observed.

Acknowledgements

We would like to express our sincere thanks to the National Natural Science Foundation of China for Financial Support (51003063, 51011130160).

References

[1] Vink E. T. H., Rábago K. R., Glassner D. A., Gruber P. R.: Applications of life cycle assessment to NatureWorks™ polylactide (PLA) production. Polymer Degradation and Stability, **80**, 403–419 (2003). DOI: 10.1016/s0141-3910(02)00372-5

[2] Kakiage M., Ichikawa T., Yamanobe T., Uehara H., Sawai D.: Structure and property gradation from surface to bulk of poly(L-lactic acid)/poly(D-lactic acid) blended films as estimated from nanoscratch tests using scanning probe microscopy. ACS Applied Materials and Interfaces, **2**, 633–638 (2010). DOI: 10.1021/am900896q

[3] Penning J. P., Dijkstra H., Pennings A. J.: Preparation and properties of absorbable fibres from L-lactide copolymers. Polymer, **34**, 942–951 (1993) DOI: 10.1016/0032-3861(93)90212-S

[4] Lam K. H., Nijenhuis A. J., Bartels H., Postema A. R., Jonkman M. F., Pennings A. J., Nieuwenhuis P.: Reinforced poly(L-lactic acid) fibres as suture material. Journal of Applied Biomaterials, **6**, 191–197 (1995). DOI: 10.1002/jab.770060308

[5] Holland S. J., Tighe B. J., Gould P. L.: Polymers for biodegradable medical devices. 1. The potential of polyesters as controlled macromolecular release systems. Journal of Controlled Release, **4**, 155–180 (1986). DOI: 10.1016/0168-3659(86)90001-5

[6] Pitt C. G., Jeffcoat A. R., Zweidinger R. A., Schindler A.: Sustained drug delivery systems. I. The permeability of poly(ε-caprolactone), poly(DL-lactic acid), and their copolymers. Journal of Biomedical Materials Research, **13**, 497–507 (1979). DOI: 10.1002/jbm.820130313

[7] Lahiri D., Rouzaud F., Namin S., Keshri A. K., Valdés J. J., Kos L., Tsoukias N., Agarwal A.: Carbon nanotube reinforced polylactide–caprolactone copolymer: Mechanical strengthening and interaction with human osteoblasts in vitro. ACS Applied Materials and Interfaces, **1**, 2470–2476 (2009).
DOI: 10.1021/am900423q

[8] Leenslag J. W., Pennings A. J., Bos R. R. M., Rozema F. R., Boering G.: Resorbable materials of poly(L-lactide). VI. Plates and screws for internal fracture fixation. Biomaterials, **8**, 70–73 (1987).
DOI: 10.1016/0142-9612(87)90034-2

[9] Majola A., Vainionpää S., Vihtonen K., Mero M., Vasenius J., Törmälä P., Rokkanen P.: Absorption, biocompatibility, and fixation properties of polylactic acid in bone tissue: An experimental study in rats. Clinical Orthopaedics and Related Research, **268**, 260–269 (1991).

[10] Gajria A. M., Davé V., Gross R. A., McCarthy S. P.: Miscibility and biodegradability of blends of poly(lactic acid) and poly(vinyl acetate). Polymer, **37**, 437–7444 (1996).
DOI: 10.1016/0032-3861(96)82913-2

[11] Aslan S., Calandrelli L., Laurienzo P., Malinconico M., Migliaresi C.: Poly (D,L-lactic acid)/poly (ε-caprolactone) blend membranes: Preparation and morphological characterisation. Journal of Materials Science, **35**, 1615–1622 (2000).
DOI: 10.1023/A:1004787326273

[12] Dell'Erba R., Groeninckx G., Maglio G., Malinconico M., Migliozzi A.: Immiscible polymer blends of semicrystalline biocompatible components: Thermal properties and phase morphology analysis of PLLA/PCL blends. Polymer, **42**, 7831–7840 (2001).
DOI: 10.1016/S0032-3861(01)00269-5

[13] Kim C-H., Cho K. Y., Choi E-J., Park J-K.: Effect of P(/LA-*co*-εCL) on the compatibility and crystallization behavior of PCL/PLLA blends. Journal of Applied Polymer Science, **77**, 226–231 (2000).
DOI: 10.1002/(SICI)1097-4628(20000705)77:1<226::AID-APP29>3.0.CO;2-8

[14] Jacobsen S., Fritz H. G.: Plasticizing polylactide – The effect of different plasticizers on the mechanical properties. Polymer Engineering and Science, **39**, 1303–1310 (1999).
DOI: 10.1002/pen.11517

[15] Baiardo M., Frisoni G., Scandola M., Rimelen M., Lips D., Ruffieux K., Wintermantel E.: Thermal and mechanical properties of plasticized poly(L-lactic acid). Journal of Applied Polymer Science, **90**, 1731–1738 (2003).
DOI: 10.1002/app.12549

[16] Kulinski Z., Piorkowska E.: Crystallization, structure and properties of plasticized poly(L-lactide). Polymer, **46**, 10290–10300 (2005).
DOI: 10.1016/j.polymer.2005.07.101

[17] Li Y., Shimizu H.: Compatibilization by homopolymer: Significant improvements in the modulus and tensile strength of PPC/PMMA blends by the addition of a small amount of PVAc. ACS Applied Materials and Interfaces, **1**, 1650–1655 (2009).
DOI: 10.1021/am900314k

[18] Li B., Yu J., Jung J., Ree M.: Amidolysis of some biodegradable polymers. Polymer Degradation and Stability, **65**, 161–163 (1999).
DOI: 10.1016/S0141-3910(98)00224-9

[19] Zhu Q., Meng Y. Z., Tjong S. C., Zhao X. S., Chen Y. L.: Thermally stable and high molecular weight poly (propylene carbonate)s from carbon dioxide and propylene oxide. Polymer International, **51**, 1079–1085 (2002).
DOI: 10.1002/pi.847

[20] Du L. C., Meng Y. Z., Wang S. J., Tjong S. C.: Synthesis and degradation behavior of poly(propylene carbonate) derived from carbon dioxide and propylene oxide. Journal of Applied Polymer Science, **92**, 1840–1846 (2004).
DOI: 10.1002/app.20165

[21] Meng Y. Z., Du L. C., Tiong S. C., Zhu Q., Hay A. S.: Effects of the structure and morphology of zinc glutarate on the fixation of carbon dioxide into polymer. Journal of Polymer Science Part A: Polymer Chemistry, **40**, 3579–3591 (2002).
DOI: 10.1002/pola.10452

[22] Li X. H., Meng Y. Z., Zhu Q., Tjong S. C.: Thermal decomposition characteristics of poly(propylene carbonate) using TG/IR and Py-GC/MS techniques. Polymer Degradation and Stability, **81**, 157–165 (2003).
DOI: 10.1016/S0141-3910(03)00085-5

[23] Li X. H., Meng Y. Z., Wang S. J., Rajulu A., Tjong S. C.: Completely biodegradable composites of poly (propylene carbonate) and short, lignocellulose fiber *Hildegardia populifolia*. Journal of Polymer Science Part B: Polymer Physics, **42**, 666–675 (2004).
DOI: 10.1002/polb.10761

[24] Li X. H., Tjong S. C., Meng Y. Z., Zhu Q.: Fabrication and properties of poly(propylene carbonate)/calcium carbonate composites. Journal of Polymer Science Part B: Polymer Physics, **41**, 1806–1813 (2003).
DOI: 10.1002/polb.10546

[25] Tao Y., Wang X., Zhao X., Li J., Wang F.: Crosslinkable poly(propylene carbonate): High-yield synthesis and performance improvement. Journal of Polymer Science Part A: Polymer Chemistry, **44**, 5329–5336 (2006).
DOI: 10.1002/pola.21595

[26] Huang Y. H., Yang X. H., Zhao S. L., Lin G., Chen M. C., Liao B., Wang C. Q., Cong G. M., Chen L. B.: Studies on the blends of carbon dioxide copolymer. III. NBR/PPC systems. Journal of Applied Polymer Science, **61**, 1479–1486 (1996).
DOI: 10.1002/(SICI)1097-4628(19960829)61:9<1479::AID-APP7>3.0.CO;2-G

[27] Wang S., Huang Y., Cong G.: Study on nitrile-butadiene rubber/poly(propylene carbonate) elastomer as coupling agent of poly (vinyl chloride)/poly (propylene carbonate) blends. I. Effect on mechanical properties of blends. Journal of Applied Polymer Science, **63**, 1107–1111 (1997).
DOI: 10.1002/(SICI)1097-4628(19970228)63:9<1107::AID-APP2>3.0.CO;2-L

[28] Huang Y., Wang J., Liao B., Chen M., Cong G.: Epoxy resins toughened by poly(propylene carbonate). Journal of Applied Polymer Science, **64**, 2457–2465 (1997).
DOI: 10.1002/(SICI)1097-4628(19970620)64:12<2457::AID-APP20>3.0.CO;2-X

[29] Pang H., Liao B., Huang Y., Cong G.: Studies on the blends of CO_2 copolymer. IV. Natural rubber/poly (propylene carbonate) systems. Journal of Applied Polymer Science, **86**, 2140–2144 (2002).
DOI: 10.1002/app.11018

[30] Ma X., Yu J., Wang N.: Compatibility characterization of poly(lactic acid)/poly(propylene carbonate) blends. Journal of Polymer Science Part B: Polymer Physics, **44**, 94–101 (2006).
DOI: 10.1002/polb.20669

[31] Yao M., Mai F., Deng H., Ning N., Wang K., Fu Q.: Improved thermal stability and mechanical properties of poly(propylene carbonate) by reactive blending with maleic anhydride. Journal of Applied Polymer Science, **120**, 3565–3573 (2011).
DOI: 10.1002/app.33565

[32] Peng S., An Y., Chen C., Fei B., Zhuang Y., Dong L.: Thermal degradation kinetics of uncapped and end-capped poly(propylene carbonate). Polymer Degradation and Stability, **80**, 141–147 (2003)
DOI: 10.1016/S0141-3910(02)00395-6

[33] Bhardwaj R., Mohanty A. K.: Modification of brittle polylactide by novel hyperbranched polymer-based nanostructures. Biomacromolecules, **8**, 2476–2484 (2007).
DOI: 10.1021/bm070367x

[34] Pluta M., Paul M-A., Alexandre M., Dubois P.: Plasticized polylactide/clay nanocomposites. I. The role of filler content and its surface organo-modification on the physico-chemical properties. Journal of Polymer Science Part B: Polymer Physics, **44**, 299–311 (2006).
DOI: 10.1002/polb.20694

[35] Lu X. L., Zhu Q., Meng Y. Z.: Kinetic analysis of thermal decomposition of poly(propylene carbonate). Polymer Degradation and Stability, **89**, 282–288 (2005).
DOI: 10.1016/j.polymdegradstab.2004.12.025

[36] Sarasua J-R., Prud'Homme R. E., Wisniewski M., Le Borgne A., Spassky N.: Crystallization and melting behavior of polylactides. Macromolecules, **31**, 3895–3905 (1998).
DOI: 10.1021/ma971545p

[37] Zhao Y-Q., Cheung H-Y., Lau K-T., Xu C-L., Zhao D-D., Li H-L.: Silkworm silk/poly(lactic acid) biocomposites: Dynamic mechanical, thermal and biodegradable properties. Polymer Degradation and Stability, **95**, 1978—71987 (2010).
DOI: 10.1016/j.polymdegradstab.2010.07.015

[38] Cooper-White J. J., Mackay M. E.: Rheological properties of poly(lactides). Effect of molecular weight and temperature on the viscoelasticity of poly(L-lactic acid). Journal of Polymer Science Part B: Polymer Physics, **37**, 1803–1814 (1999).
DOI: 10.1002/(SICI)1099-0488(19990801)37:15<1803::AID-POLB5>3.0.CO;2-M

eXPRESS Polymer Letters Vol.5, No.11 (2011) 950–958
Available online at www.expresspolymlett.com
DOI: 10.3144/expresspolymlett.2011.93

Injection molding micro patterns with high aspect ratio using a polymeric flexible stamper

S. H. Park[1], *W. I. Lee*[1*], *S. N. Moon*[1], *Y.-E. Yoo*[2], *Y. H. Cho*[3]

[1]Division of WCU Multiscale Mechanical Design, Department of Mechanical and Aerospace Engineering, Seoul National University, Seoul 151-742, Korea
[2]Korea Institute of Machinery and Materials, Daejon 305-343, Korea
[3]School of Mechanical Design & Automation Engineering, Seoul National University of Technology, Seoul 139-743, Korea

Received 21 February 2011; accepted in revised form 8 May 2011

Abstract. Poor filling occurs during the injection molding process of micro- or nano- scale patterns mainly because the hot polymer melt rapidly cools and its skin quickly solidifies upon contact with the mold surface. In this study, it is proposed to use Polyethylene terephthalate (PET) film coated with patterned polyurethane acrylate (PUA) as an effective thermal barrier. It can significantly hinder heat transfer into the mold during the molding process and thus may keep the melt viscosity low for longer duration. As a result, the replication would be improved not only during the filling phase but also during the packing phase. In order to verify the validity of the use of polymeric stamper, the melt-film interface temperature was evaluated by numerical simulation. Experimental results indicated that patterns possessing widths within the range of one to tens of micrometers and a height of approximately 10 μm were successfully filled and demolded.

Keywords: *processing technologies, micro-injection mold, flexible stamper*

1. Introduction

In recent years, fabrication of polymer based micro components for optical and biomedical applications has gained increasing attention [1]. Micro-molding of polymer-based materials has the advantages of low cost, good biocompatibility, high optical clarity and high impact strength. Hot embossing and micro injection molding are the most industrially viable processes used for molding micro- and nano-patterns. The hot embossing process uses a pre-heated mold in an evacuated chamber, and is subsequently brought into contact with the thermoplastic polymer melt. After pressing the mold onto the polymer melt, the system that consists of the tool and part is cooled down, after which the part is demolded. The hot embossing process is suitable for replicating complex or high aspect ratio (>2) microstructures [2, 3]. However, a major inconvenience encountered through this process is the need of long cycle times for heating and cooling both the mold and the material [4]. In comparison, micro injection molding possesses promising possibilities for mass production due to the short cycle time and the process ability to be easily automated. In this context, micro-injection molding of polymer materials is a key technology for micro-and nano molding. With the existing injection molding equipment and techniques, complete replication of the micro- and sub-micron structures with aspect ratios larger than 2 are hard to obtain for various reasons [5]. In order to avoid incomplete filling of micro- and nano-patterns, the mold temperature should be near or higher than the softening temperature of the polymer during the filling and packing phases. This is due to the

*Corresponding author, e-mail: wilee@snu.ac.kr

fact that polymer melt above the glass transition temperature exhibits sufficient fluidity, and thus the polymer melt can adequately fill the sub-micron patterns before entering the glassy state. [6, 7]. As the aspect ratio increases, the mold temperature must also increase [8, 9]. The variotherm system [10] can satisfactorily reach such temperatures without a dramatic increase in cycle time. However, this process ultimately reduces the mold lifetime [11] and demands expensive tools. Liou and Suh [12] proposed an insulated mold insert that was coated with Teflon for retaining the heat in the mold cavity. Kim *et al*. [13] introduced nano-pattern insert molding (NPIM) in which the nano-pattern is molded using the poly(vinly alcohol) (PVA) template film with nano-patterns on its surface. The temperature near the mold surface would be maintained above no-flow temperature for a relatively long duration by the polymeric stamper or coating material that acted as a thermal barrier, inevitably delaying the solidification of the polymer near the mold surface. As a result, transcription would be continued during the packing phase improving the quality of replication. Recently, polymeric stampers using PDMS have also been used for hot embossing due to their economic and straightforward approach to fabricate micro feature [14].

This study demonstrated the viability of a method to use polymeric film as a stamper for injection molding of micro patterns with a high aspect ratio (> 9). The polymeric stamper patterned with polyurethane acrylate (PUA) on the surface effectively delayed solidification near the mold surface. PUA resin used in this study is an ultra-violet (UV)-curable polymer and forms cross-links after cure. Therefore, the polymeric stamper using the PUA does not have a melting temperature. In addition to the thermal stability, PUA is a Rigiflex polymer that possesses relatively high rigidity (>40 MPa) compared to PDMS and has low surface energy.

The effects of the polymeric stamper on the temperature profiles of the polymer melt and cavity surface were analyzed using commercial software Moldex3D. In order to verify the effect of the packing pressure and packing time on the transcription during the delayed solidification provided by the polymeric stamper, we fabricated micro-patterns that have a width within the range of one to tens of micrometers with a height of approximately 10 μm.

2. Experiment and heat transfer analysis

2.1. Fabrication of polymeric stamper

The polymeric stamper was prepared using polyethylene terephthalate (PET) film as a substrate with

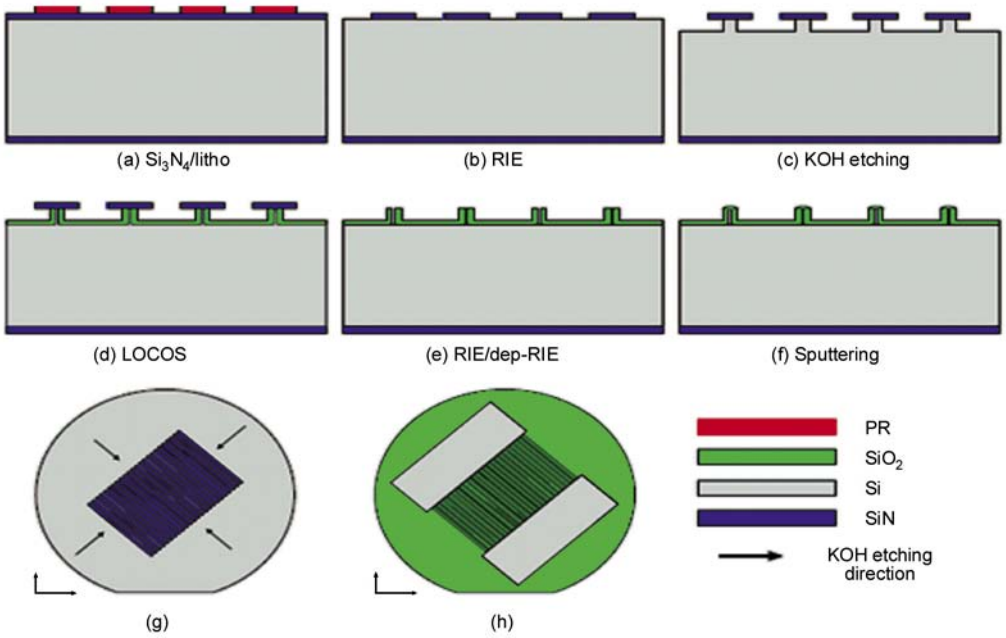

Figure 1. Illustration of silicon master fabrication process. (a) Si_3N_4 deposition and photolithography. (b) RIE. (c) Anisotropic KOH etching. Si is vertically etched. (d) LOCOS. (e) RIE for removal of Si_3N_4 mask and RIE or deep-RIE for Si etching. (f) Dioxide layer deposition for sealing. (g) Illustration showing the top side view of anisotropic KOH etching. (h) Schematic view of microchambers at the end of nanochannel arrays.

PUA forming micro-patterns on the film surface. First, a silicon master to imprint the micro pattern was fabricated. The fabrication process comprises a combination of anisotropic etching, the local oxidation of silicon and the plasma etching of silicon [15]. Figure 1 shows the fabrication process of the silicon master using a 3-inch <100> oriented single crystalline silicon wafer.

Once the silicon master is ready, the polymeric stamper was prepared by imprinting micro pattern

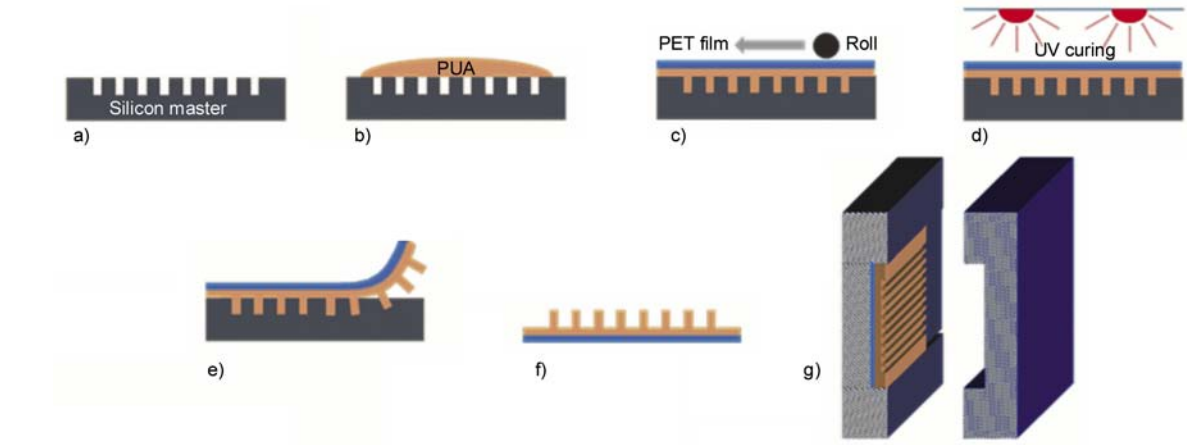

Figure 2. Illustration of fabrication process of flexible polymeric stamper and its installation on the mold wall. (a) Silicon master is prepared. (b) PUA is dispensed on the silicon master. (c) PET film is pressed against the silicon master with liquid PUA resin dispensed. (d) PUA resin is cured by irradiating ultraviolet light. (e) Pet film with PUA micro pattern on the surface (polymeric stamper) is detached from the silicon master. (f) Polymeric stamper is ready. (g) Polymeric stamper is attached on the mold wall.

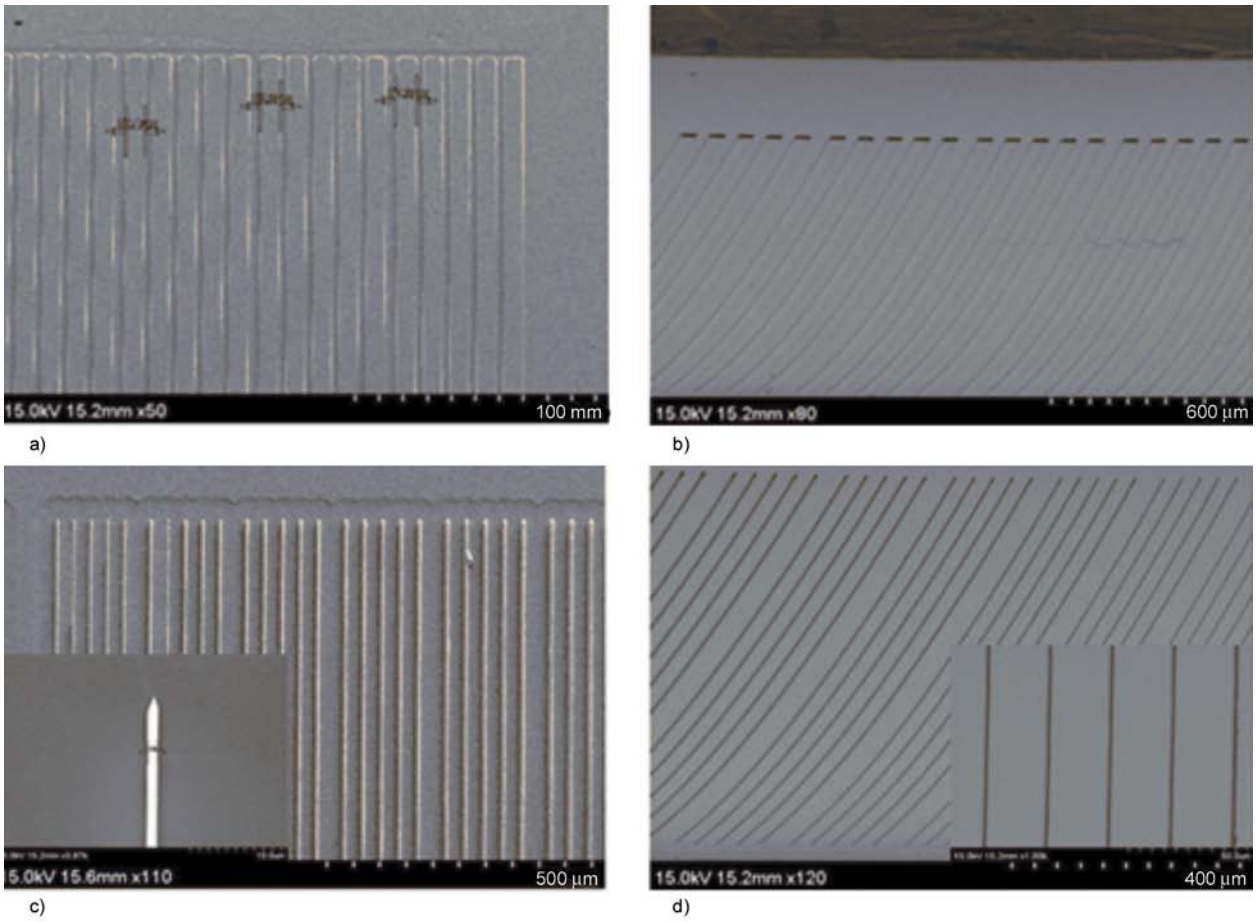

Figure 3. The SEM surface image of the silicon master patterns and replicated PUA patterns. The pattern widths are about 90 µm (a and b) and about 1 µm (c and d). The height of the patterns is 10 µm

of PUA resin using the silicon master on PET film. As illustrated in Figure 2, PUA (MINS 311RM, Minuta Tech, Korea) resin was dispensed on the silicon master. The silicon master was composed of lines structure of varying channel widths, between 80 and 1.0 μm, with a channel depth of 10 μm (Figure 2a). Once the photocurable PUA was drop-dispensed onto a master pattern (Figure 2b), a flexible 50 μm thick PET film was pressed against the liquid drop (Figure 2c). A roller was used to distribute the resin evenly. The film was then exposed to ultraviolet light (wavelength: 250~356 nm) for 4 minutes, at an intensity of 90 mW/cm^2 (Figure 2d). After UV curing, the fabricated stamper was peeled off from the master using tweezers (Figure 2e). The patterned stamper thus prepared was installed on one side of the injection mold cavity (Figure 2f).

Different micro patterns were used in this study as shown in Figure 3. Above mentioned technique allowed self-replication of the mold even for very fine patterns (less than 100 nm) with high aspect ratio. The scanning electron microscopic (SEM) micrographs are presented in Figures 3a and 3c for the master and Figures 3b and 3d for the replicated patterns with PUA. These micrographs demonstrate the replication capability of the proposed method for various pattern widths and aspect ratios.

2.2. Replication by injection molding

The injection molded plate used in this study was rectangular in shape having dimensions of 60.0 mm × 60.0 mm×1.0 mm. Polymethylmethacrylate (PMMA) was injected into the cavity using an injection molding machine (SE150 by Sumimoto). The injection molding conditions are listed in Table 1. The injection speed, filling time, and melt temperature were set to 250 mm/s, 0.09 s and 265°C, respectively. In addition, three different packing pressures were selected and two different packing times were considered to see the effect of these parameters. The above mentioned molding conditions were chosen to evaluate the quality of transcription for cases in which the patterns were less than 4 μm. Patterns with channel width greater than 5 μm were completely filled for the packing pressure above 5 MPa and the packing time of 0.5 s (Figure 4).

Table 1. Injection molding process parameters

Mold temperature [°C]	25
Melt temperature [°C]	265
Injection speed [mm/s]	250
Packing time [s]	0.5, 2
Packing pressure [MPa]	5, 10, 40
Filling time [s]	0.09

The replication of the micro pattern was quantified using the ratio between the micro pattern depth and the filling depth. The degree of transcription (*DOT*) was defined as Equation (1):

$$DOT = \frac{h_f}{h_m} \tag{1}$$

where h_f is the depth of filling and h_m is the depth of the pattern in the stamper.

It is noted that the polymeric stampers lasted more than 100 injections for the patterning without causing significant deformation. Investigations of replicated polymer surfaces by SEM and atomic force microscopy (AFM) provided no evidence for abra-

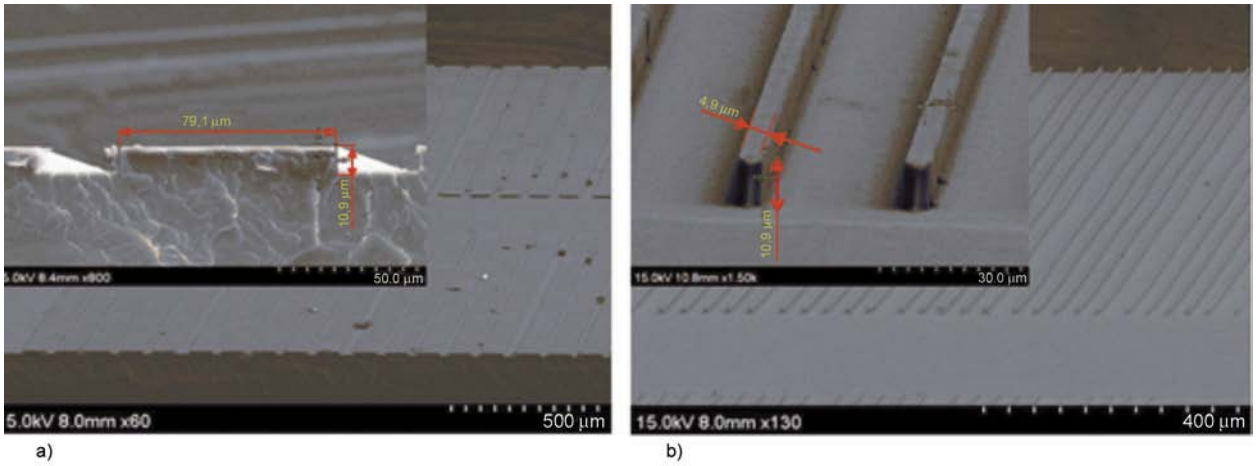

Figure 4. SEM image of the replicated pattern. Packing time was 0.5 s and packing pressure was 40 MPa: (a) Pattern with low aspect ratio; (b) pattern with high aspect ratio.

sion residues of the PUA master on the polymer surface.

2.3. Numerical analysis of temperature

In order to investigate further the effectiveness of the polymeric stamper as a thermal barrier, heat transfer analysis was done numerically. The injection molding analysis software Moldex3D was used to simulate the polymeric stamper effects on the temperature variation during injection molding by setting similar boundary and initial conditions to the real processes. During the mold filling in the injection molding, due to the thermal contact resistance between the mold and the melt, the mold-melt interface temperature (T_{mt}) is usually higher than the set mold temperature (T_{mb}). In many cases, however, T_{mt} may not be so different from T_{mb} [16]. In this study, T_{mb} was used to represent T_{mt} in the molding simulations. In the simulations, initial mold temperatures and the resin temperature were set to be 30 and 265°C, respectively. Various film thicknesses (50, 75, and 100 μm) were also assumed for the simulations. Thermophysical properties used in the calculations are listed in Table 2.

For the energy equation, the boundary condition is defined as Equations (2) and (3):

$$q = h_c(T_{mt} - T_{mb}) \qquad (z = p, \text{ Figure 5}) \qquad (2)$$

$$k_m \frac{\partial T_m}{\partial z} = k_f \frac{\partial T_f}{\partial z} \qquad (z = p + f, \text{ Figure 5}) \qquad (3)$$

The heat transfer coefficient h_c between the part and mold base depends on materials, temperature, and process conditions. The default value in Moldex3D was used and the heat transfer coefficient in this study was 5000 W/m^2·K.

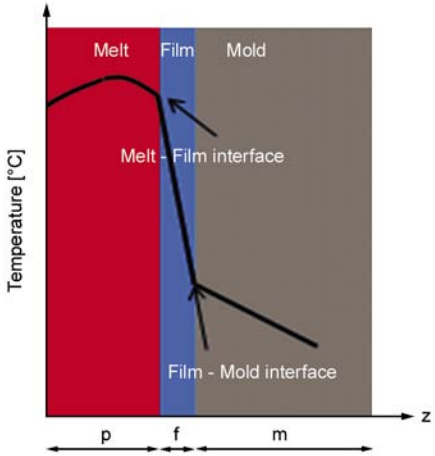

Figure 5. Illustration of temperature profiles with the polymeric stamper as a thermal barrier

Table 2. Thermophysical properties used for heat transfer anaysis

	Mold (Steel)	PMMA	PET
Density [kg/m^3]	7820	1160	1405
Thermal conductivity [W/m°C]	50.2	0.15	0.2745
Specific heat [J/kg°C]	485	2050	1924

3.Results and discussion

3.1. Heat transfer analysis

The influence of the polymeric stamper on heat transfer is identified by comparing the rate of temperature increase on the mold surface with and without the polymeric stamper and shows the effect of PET film thickness (Figure 6). For conventional injection molding, mold surface temperature rapidly rises when the melt contacts the mold surface during the filling phase. For the case in which the polymeric stamper is used, it retards heat flow into the mold surface, resulting in a slower rise in the mold surface temperature. As a result, the temperature of the polymer near the polymeric stamper surface was maintained above no-flow temperature for longer duration than the conventional injection molding process, as shown in Figure 7 and Figure 8. Because the viscosity is a function of temperature, the fluidity of the polymer melt improved markedly. Also, the fluidity was maintained for a relatively longer period of time. This improvement indicates that the polymer melt near the polymeric stamper easily flows into the micro patterns even during the packing phase as well as the filling phase.

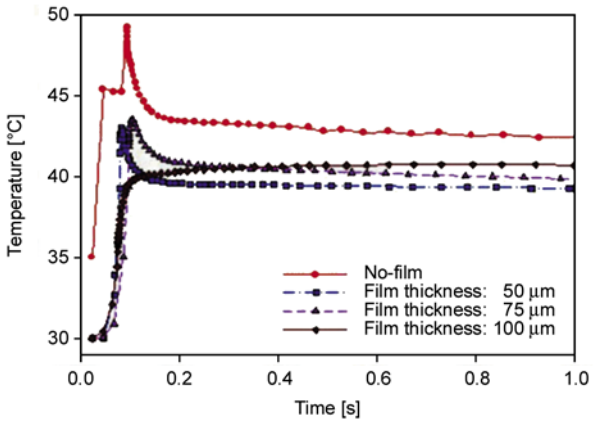

Figure 6. Change in mold cavity surface temperature with time. Comparison of numerical results with and without polymeric stamper.

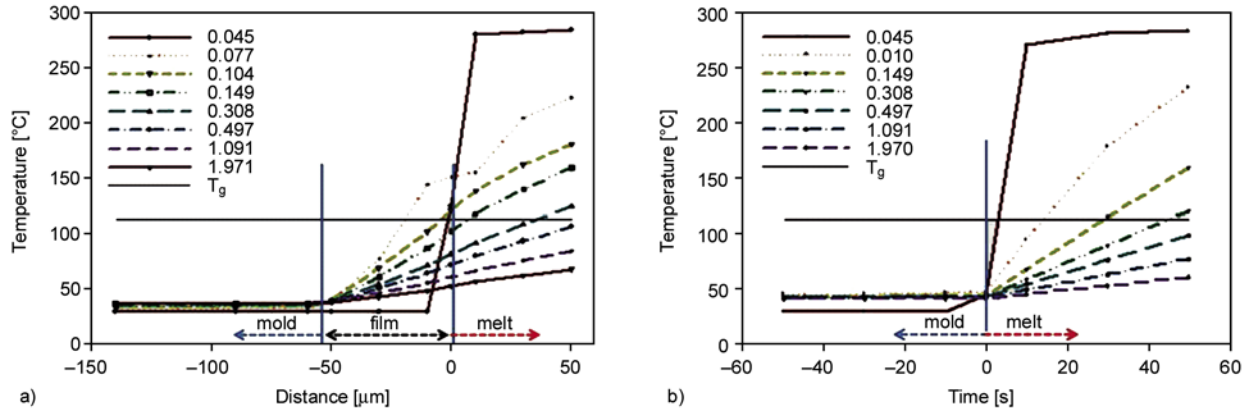

Figure 7. Temperature profile near the polymeric stamper right after contact with the melt (0.01 to 2.0 s after the contact): (a) with 50 μm thickness polymeric stamper, (b) without polymeric stamper. Results of numerical simulation

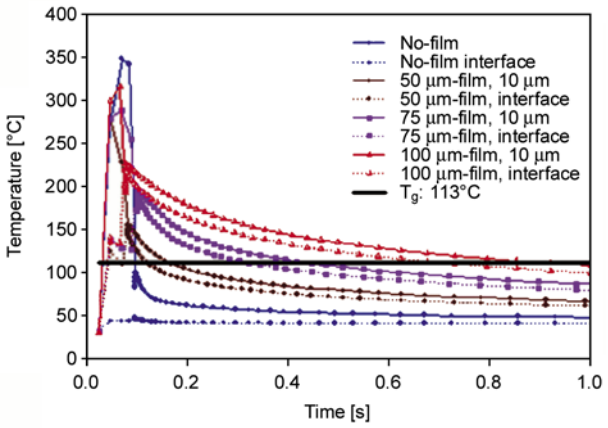

Figure 8. Temperature profile near the polymeric stamper (10 μm from the mold or polymer stamper) and in the interface between mold and melt right after contact with the melt (0.01 to 1.0 s after the contact). Results of numerical simulation.

3.2. Effect of the packing pressure and packing time

A key to better transcription of micro patterns during injection molding would be high fluidity of the melt especially near the mold wall where the micro patterns are located. The parameters related to fluidity of the melt would be, among others, the injection velocity and the melt temperature, and the mold temperature. At higher melt temperature, the polymer flows longer because of lower viscosity of the melt and thus the degree of transcription and pattern definition will be improved. Higher injection velocity also reduces cooling of the melt during filling, and thus, improves pattern replication. While higher mold temperatures will slow the cooling and allow more melt to flow into the micro patterns, the mold temperature significantly affects how the packing pressure and packing time influ-

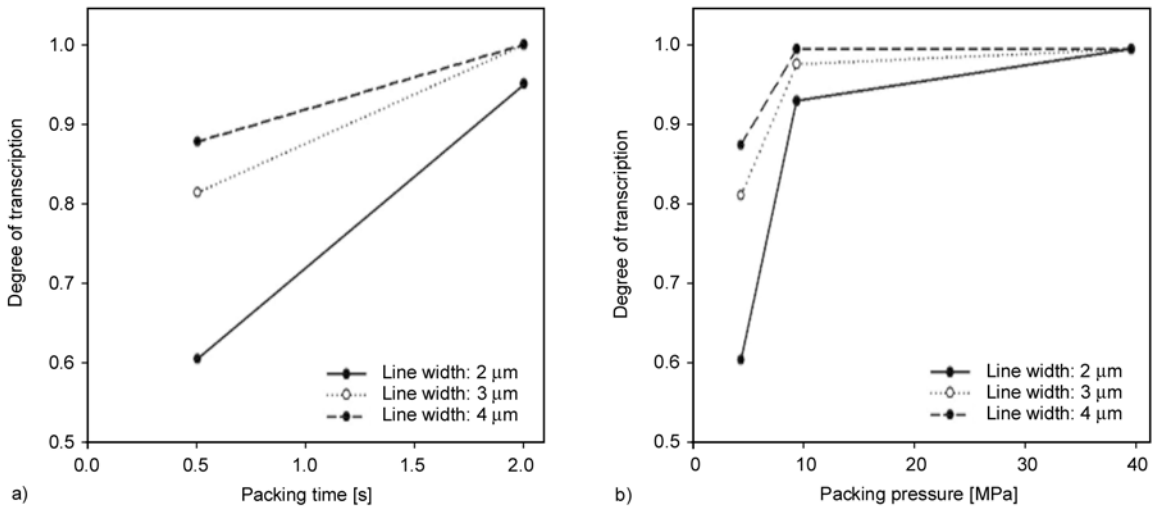

Figure 9. Effect of the packing pressure and the packing time on the degree of transcription. Experimental data. (a) Degree of transcription in relation to the packing time for the packing pressure of 5 MPa. (b) Degree of transcription in relation to the packing pressure for the packing time of 0.5 s.

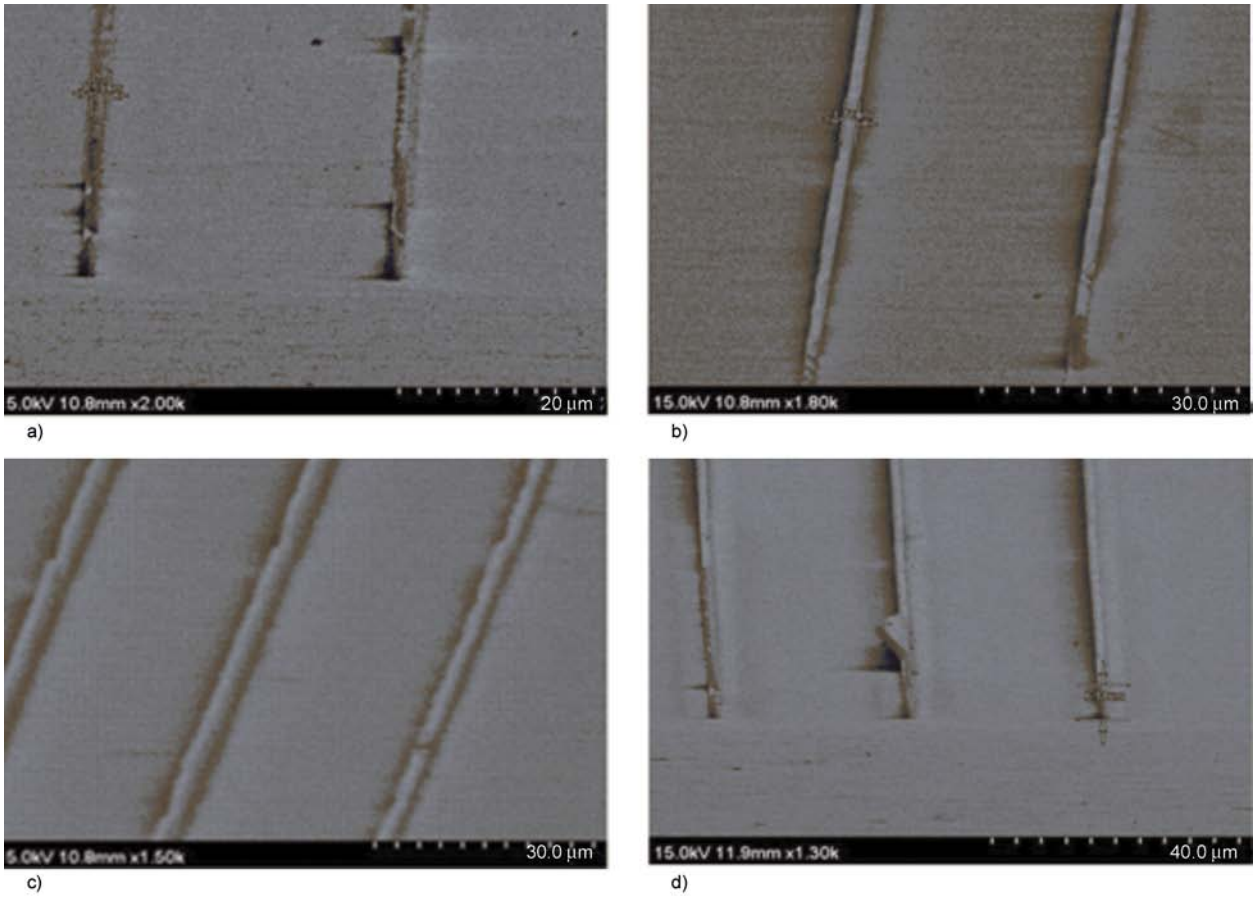

Figure 10. SEM image of the replicated patterns under various packing pressures and times pattern width of 1 µm. As can be seen, replication quality was not consistent (a–d).

ences the transcription [17]. For cases in which the mold temperature is low, packing pressure and packing time do not significantly influence the filling depth in comparison to other conditions. It is because the solidified layer near the mold wall prevents polymer melt from flowing into the micro patterns. As a result, if the temperature of the polymer near the stamper surface is maintained above the no-flow temperature for a long period of time, packing pressure would improve the transcription.

The relationship between transcription and the packing time is shown in Figure 9a. While the packing pressure was maintained, the degree of transcription increased. The degree of transcription in relation to the packing pressure is shown in Figure 9b. As the packing pressure increased from 5 to 40 MPa, micro-patterns were completely replicated without increasing the packing time. In addition, the patterns with larger line-width were completely filled at lower packing pressure and packing time. For patterns with width less than 1µm, replication quality was not consistent as can be seen from Figure 10. In summary, at relatively high packing pressure (40 MPa) and long packing time (5 s), micro patterns with narrow line width (down to about 1 µm) and high aspect ratio (above 9) was successfully replicated (Figure 11).

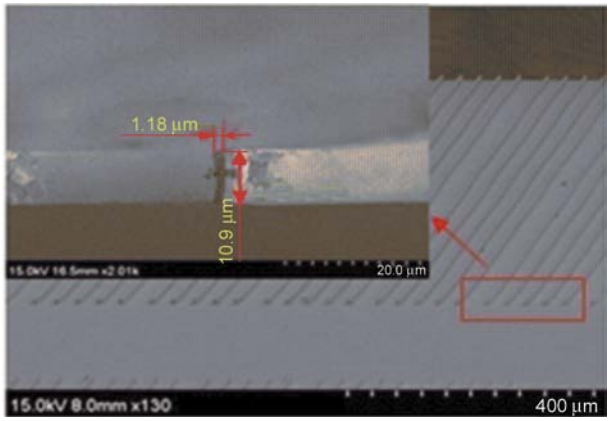

Figure 11. SEM image of the replicated pattern with high aspect ratio of 9.24.

4. Conclusions

This study demonstrates the viability to fabricate micro patterns with high aspect ratios (>9) using the polymeric stamper patterned with PUA on the surface. The silicon master was made with a novel fabrication technique for generating silicon dioxide channel arrays without the use of the nanolithography technique and polymeric stamper was used instead of the nickel mold insert. The temperature of the polymer melt near the polymeric stamper surface was maintained above the no-flow temperature for a longer duration in comparison to conventional injection molding. As a result, delaying the development of the solidified layer and increasing the fluidity of the polymer melt during the packing phase as well as the filling phase near the stamper surface improved the transcription quality for patterns with a high aspect ratio (>9). The life of the polymer stamper well exceeded 100 cycles, which suggest a possibility of practical application. Compared with conventional hard masters, durability can be an issue for polymeric molds used in this study. In order for the proposed method to be used in the applications with high production runs, durability of the polymer stampers should be investigated thoroughly.

Another important point is that the micro patterns with high aspect ratio were fabricated without fracture. The PUA mold used in this study had low surface energy. Because of these advantages, the polymer stamp using PUA had good demolding characteristics and releasing the polymer from the stamper was easy.

Acknowledgements

This work was supported by the Korea Research Foundation Grant funded by the Korean Government (MOEHRD) (Grant KRF-J03003) and by WCU (World Class University) program (R31-2008-000-10083-0).

References

[1] Weber L., Ehrfeld W., Freimuth H., Lacher M., Lehr H., Pech B.: Micromolding: A powerful tool for large-scale production of precise microstructures. in 'Proceedings of the SPIE 2879, Austin, USA' 156–167 (1996).
DOI: 10.1117/12.251203

[2] Becker H., Heim U.: Hot embossing as a method for the fabrication of polymer high aspect ratio structures. Sensors and Actuators A: Physical, **83**, 130–135 (2000).
DOI: 10.1016/S0924-4247(00)00296-X

[3] Mekaru H., Yamada T., Yan S., Hattori T.: Microfabrication by hot embossing and injection molding at LASTI. Microsystem Technologies, **10**, 682–688 (2004).
DOI: 10.1007/s00542-004-0401-8

[4] Heckele M., Schomburg W.: Review on micro molding of thermoplastic polymers. Journal of Micromechanics and Microengineering, **14**, 1–14 (2004).
DOI: 10.1088/0960-1317/14/3/R01

[5] Mönkkönen K., Pakkanen T. T., Hietala J., Pääkkönen E. J., Pääkkönen P., Jääskeläinen T., Kaikuranta T.: Replication of sub-micron features using amorphous thermoplastics. Polymer Engineering and Science, **42**, 1600–1608 (2002).
DOI: 10.1002/pen.11055

[6] Ong N. S., Koh Y. H.: Experimental investigation into micro injection molding of plastic parts. Materials and Manufacturing Processes, **20**, 245–253 (2005).
DOI: 10.1081/AMP-200042004

[7] Su Y-C., Shah J., Lin L.: Implementation and analysis of polymeric microstructure replication by micro injection molding. Journal of Micromechanics and Microengineering, **14**, 415–422 (2004).
DOI: 10.1088/0960-1317/14/3/015

[8] Whiteside B. R., Martyn M. T., Coates P. D., Allan P. S., Hornsby P. R., Greenway G.: Micromoulding: Process characteristics and product properties. Plastics, Rubber and Composites, **32**, 231–239 (2003).
DOI: 10.1179/146580103225002650

[9] Whiteside B. R., Martyn M. T., Coates P. D., Greenway G., Allen P., Hornsby P.: Micromoulding: Process measurements, product morphology and properties. Plastics, Rubber and Composites, **33**, 11–17 (2004).
DOI: 10.1179/146580104225018346

[10] Chang P-C., Hwang S-J.: Simulation of infrared rapid surface heating for injection molding. International Journal of Heat and Mass Transfer, **49**, 3846–3854 (2006).
DOI: 10.1016/j.ijheatmasstransfer.2006.04.014

[11] Tseng S-C., Chen Y-C., Kuo C-L., Shew B-Y.: A study of integration of LIGA and M-EDM technology on the microinjection molding of ink-jet printers' nozzle plates. Microsystem Technologies, **12**, 116–119 (2005).
DOI: 10.1007/s00542-005-0014-x

[12] Liou M. J., Suh N. P.: Reducing residual stresses in molded parts. Polymer Engineering and Science, **29**, 441–447 (1989).
DOI: 10.1002/pen.760290703

[13] Kim S. H., Jeong J. H., Youn J. R.: Nanopattern insert molding. Nanotechnology, **21**, 205302/1–205302/6 (2010).
DOI: 10.1088/0957-4484/21/20/205302

[14] Malek C. K., Coudevylle J-R., Jeannot J-C., Duffait R.: Revisiting mic ro hot-embossing with moulds in non-conventional materials. Microsystem Technologies, **13**, 475–481 (2007).
DOI: 10.1007/s00542-006-0184-1

[15] Cho Y. H., Lee S. W., Kim B. J., Fujii T.: Fabrication of silicon dioxide submicron channels without nanolithography for single biomolecule detection. Nanotechnology, **18**, 465303/1–465303/6 (2007).
DOI: 10.1088/0957-4484/18/46/465303

[16] CoreTech System Co. Ltd.: Moldex3D/solid-RIM reference manual. HsinChu, Taiwan (2003).

[17] Lee B-K., Hwang C-J.: Replication quality of flow-through microfilters in microfluidic lab-on-a-chip for blood typing by microinjection molding. Journal of Manufacturing Science and Engineering, **130**, 021010/1–021010/8 (2008).
DOI: 10.1115/1.2896142

eXPRESS Polymer Letters Vol.5, No.11 (2011) 959–969
Available online at www.expresspolymlett.com
DOI: 10.3144/expresspolymlett.2011.94

Rigid and flexible azopolymers modified with donor/acceptor groups. Synthesis and photochromic behavior

A. Raicu Luca[1], *L. Rocha*[2], *A.-M. Resmerita*[1,3], *A. Macovei*[4], *M. Hamel*[2], *A.-M. Macsim*[3], *N. Nichita*[4], *N. Hurduc*[1*]

[1]'Gheorghe Asachi' Technical University of Iasi, Department of Natural and Synthetic Polymers, Prof. Dimitrie. Mangeron Street, 73, 700050-Iasi, Romania
[2]CEA, LIST Saclay, Laboratoire Capteurs et Architectures Électroniques, F-91191 Gif-sur-Yvette Cedex, France
[3]Institute of Macromolecular Chemistry Petru Poni, Gica Voda Alley 41A, 700487 Iasi, Romania
[4]Institute of Biochemistry of the Romanian Academy, Department of Viral Glycoproteins, Splaiul Independentei 296, Sector 6, Bucharest, Romania

Received 16 March 2011; accepted in revised form 18 May 2011

Abstract. The aim of this work is to investigate the photochromic behavior and nano-structuration capacity of azo-polymers with different architectures and main chain flexibilities, modified with donor/acceptor groups. As a function of the chemical structure and the substitution degree, the azo-polymers can generate physical interactions and lead to different polymer chain conformational re-organization under optical excitation. Nano-structuration experiments were performed on samples with different chemical structures. Surface relief gratings have been realized both in poly(chloromethyl styrene) and polysiloxanes polymers. The complexity of the phenomena that take place under optical excitation of the azo-benzene molecules are reflected by the samples behavior during the nano-structuration process. Preliminary tests to determine the ability of the azo-polysiloxanic films to support cell growth were performed. The films showed remarkable properties to sustain both cell adhesion and proliferation.

Keywords: *smart polymers, photochromic behavior, cell cultures, SRG, azobenzene*

1. Introduction

Azobenzene-containing polymers have received increasing attention due to their unique properties allowing various applications, such as in micro-fluidic or in membrane based separation systems, to optically change the materials surfaces wettability [1–5], in biology, to generate photosensitive micellar systems for drug delivery purposes, for example [6, 7], in optics or optoelectronics, to generate optical switching and data storage functions [8–13]. The distinct properties of these materials are attributed to the photo-isomerization of azobenzene molecules which undergo reversible *trans–cis* isomerization of the double bond [14], under external stimuli. It should be emphasized that isomerization of the azobenzene is accompanied by large changes in both geometry and dipole moment [15–19]. These photo responsive properties are determined by both azo-chromophore structure and polymeric architecture.

One of the most interesting applications is connected to the possibility to induce a certain type of relief on the surface of azo-polymeric film, by laser irradiation, [20–22]. This surface nano-structura-

*Corresponding author, e-mail: nhurduc@ch.tuiasi.ro

tion can be used, for example, to improve the performances of devices such as organic light emitting diodes (OLEDs), organic photovoltaic devices (OPV cells) [23, 24] or in biological applications as a support to modify the behavior of cell cultures [25].

It is known that the relief formation is based on a directional flowing process [26]; however, despite the nano-structuration procedure being investigated for more than 15 years [5, 6] the mechanism has not been completely elucidated yet. Indeed, the photo-induced mass-transport process, at the base of the surface deformation, enables direct production of surface relief gratings, through exposition of the films to a spatially modulated intensity pattern. This method appears thus as a simple tool enabling the realization of complex surface structures, through a single step procedure [27]. An important aspect concerning the relief quality is the geometrical surface stability, directly connected with the glass transition temperature (T_g) value of the polymer. Especially in the case of polysiloxane main-chain systems, some problems concerning the surface relief stability can appear due to T_g values close to room temperature. While the high flexibility of the polysiloxane backbone should provide an increased sensitivity of the azopolymer film topography to light stimulation, a competition between the optically controlled mass transport and the isotropic thermal redistribution of the material at ambient temperature can occur. This phenomenon will then limit the potential of such materials for applications involving nanostructured films. In this case, the physical interactions between donor/acceptor (D/A) groups connected to the polymeric chains can offer a supplementary stability of the surface relief.

In this context, the aim of this work was to investigate the photochromic behavior and nano-structuration capacity of azo-polymers with different architectures and main chain flexibilities, modified with D/A groups. Two types of polymer architectures were investigated: flexible main-chain polysiloxanes and rigid poly(chloromethyl styrene) derivatives. Herein, we studied the photo-isomerization process in solution and solid states, and the effect of polymers backbone and substitution degree with azobenzene and D/A groups in these processes. Preliminary tests concerning the nano-structuration capacity were also performed at room temperature, using the intensity modulations of an interference pattern produced with laser irradiation [28]. The interest to obtain azo-polysiloxane nano-structured films is moreover justified by their potential biological applications. Thus, preliminary cell proliferation experiments using two different cell lines evidenced not only a normal attachment to the substrate, but also, a division rate similar to controls, even on the plane films. This behavior is very encouraging, especially in the light of the literature data published so far in the field. To our knowledge, there is only one study reporting the possibility to use azopolymer films as cell growth support. This showed that a commercial copolymer poly[(methylmethacrylate)-co-(disperse red 1 acrylate)], was not able to sustain the development of fibroblast cells on the plane surface of the azopolymeric films, only the structured region allowing cell adhesion and growth [25].

2. Experimental part

Methylene chloride (code 270997), dimethylsulfoxide (code 494429), methanol (code 494437), chloroform (code 472476) 4-phenylazophenol (code 131083) and 2,4-dinitrophenol (code 42170) were purchased from Aldrich, Steinheim, Germany and used without supplementary purification. The ((chloromethyl)phenylethyl)methyldichlorosillane (AB110958) was purchased from ABCR GmbH & Co. KG, Karlsruhe, Germany and used without supplementary purification. The azopolymers were synthesized in two steps by nucleophilic substitution of chlorobenzyl groups with the sodium salt of 4-(phenylazo) phenol or 2,4-dinitrophenol as shown in Figure 1. More details concerning polymer synthesis can be found in our previous reports [29, 30]. All polymers were characterized by ^{1}H-NMR, differential scanning calorimetry (DSC), UV spectroscopy and surface contact angle measurements. The photochromic behavior (azobenzene *trans-cis* isomerization and the *cis-trans* relaxation phenomena) was investigated in solid state by UV spectroscopy using a Shimadzu spectrophotometer (Shimadzu UV 1700 Pharma Spy, Kyoto, Japan). For the measurements in solid state, thin film were coated on the surface of a quartz cuvette. The azopolymer solutions and films were irradiated using a UV lamp (100 W) equipped with 365 nm filter and during irradiation experiments the surface of the films was cooled with compressed air, the tempera-

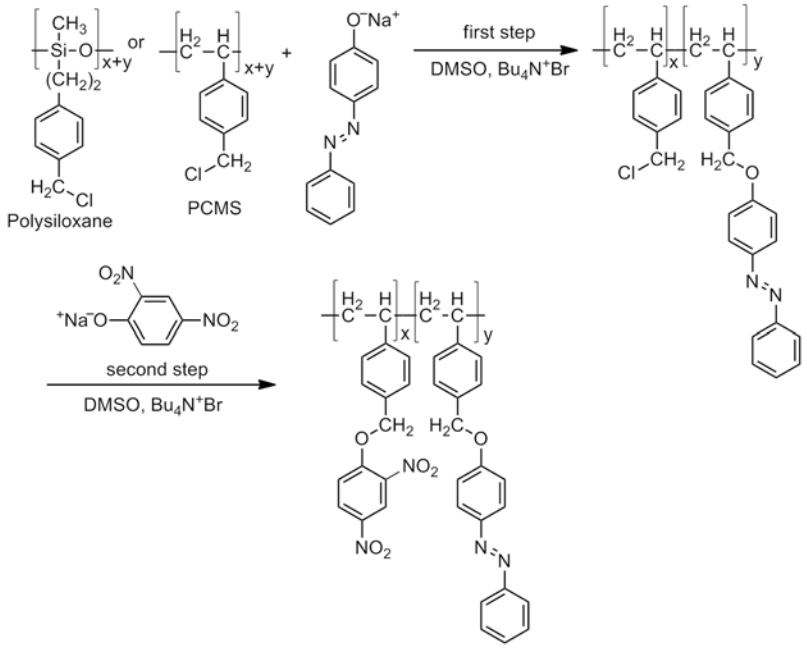

Figure 1. Synthesis of azopolymers modified with 2,4-dinitrophenol

ture being maintained at 22°C (±1°C). The isomerization kinetics of azobenzene can be investigated due to the fact that the *trans* and the *cis* isomers absorption occurs at different wavelengths: a strong absorption peaking at 350 nm, attributed to the π-π* of azobenzene chromophore and a weak broad band in the visible region with a maximum at 440 nm, corresponding to the n-π* electronic transition of the same moiety. During UV irradiation at 365 nm the absorbance corresponding to the π-π* transition of azobenzene strongly decreases, whereas intensity of the n-π* electronic transition slightly increases. Subsequently, visible light irradiation leads to recovery of the shape of the absorbance spectra, but only partially. ^{1}H-NMR spectra were recorded on Bruker 400 MHz apparatus (Bruker, Rheinstetten, Germany). DSC analysis was performed with a Mettler DSC-1 machine (METTLER-TOLEDO GMB, Switzerland) with a heating rate 10°C/min under N_2 atmosphere. The GPC (Polymer Laboratories PL-GPC 129 United Kingdom) measurements were effectuated in THF using polystyrene standard. The isomerization phenomena were measured with the Shimadzu spectrophotometer. The static contact angle values were measured using EasyDrop Shape Analysis System (KRUSS Easy Drop Standard, Hamburg, Germany) equipped with DSA 1 evaluation software. A drop of liquid (10 μl) is placed on the film surface.

The nanostructured surfaces were obtained by illumination of the polymer films with an interference pattern produced by the superposition of two coherent light beams absorbed by the azo-molecules. The beams were incident with a θ angle on the film surface, schematically show in Figure 2, resulting in a pattern with a sinusoidal modulated intensity. The excitation was performed in the visible range, with a laser diode delivering a 488 nm wavelength beam. The intensity of irradiation was 170 mW/cm^2 and the beams were p-polarized, i.e. with a polarization in the beams incidence plane. In this configuration the polarization axes are perpendicular to the fringes of the interference pattern, in order to favor a migration of the material from the high intensity regions of the interference pattern to the low ones [31].

The HepG2 (human hepatoblastoma) and HeLa (human ovarian cancer) cells were maintained at 37°C, in RPMI medium supplemented with 10% fetal calf serum, 50 units/ml penicillin, 50 μg/ml streptomycin and 2 mM GlutaMAX (Gibco® Cell Culture,

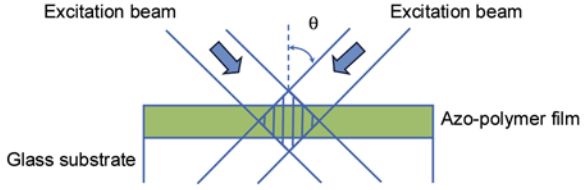

Figure 2. Excitation configuration for the induction of surface relief gratings in azo-polymer films

USA) in a 5% CO_2 atmosphere. An equal number of cells were seeded onto the azo-polymer film and control (microscope cover glass) substrates. Cell attachment and multiplication were visualized 24 hours later, using an inverted Nikon microscope (Nikon Instruments Europe B.V.)

3. Results and discussion

Two different polymer groups (having a flexible or a rigid main-chain) modified with 4-(phenyl-azo) phenol and 2,4-dinitrophenol were investigated, in order to identify the best candidates concerning the nano-structuration process. Some characteristics of the synthesized polymers are presented in Table 1.

The synthesized polymers were modified with azobenzene and 2,4-dinitrophenol, to a 45–90 and 22–56% substitution degree, respectively, The molecular weights (M_n) of the polymers are situated in the range of 5900 to 8800. The glass transitions T_g values are strongly influenced by the main-chain flexibility being located between 15 and 30°C, in the case of polysiloxanes and from 106 to 123°C, in the case of modified PCMS.

The UV-Vis spectra (in solid state) corresponding to the synthesized polymers are presented in Figure 3. All the films, except sample 9, are characterized by two peaks of absorbance. The weak broad peak, in the visible region at 440 nm, corresponds to both the *trans* and the *cis* isomers and the strong peak, with maximum at 343–345 nm is attributed to the *trans* isomer absorption. These two configurations can be easily inter-converted by light, involving large changes in dipole moment and geometry. When the films are exposed to UV light, the stable *trans* form (lower energy) can be photo-isomerized

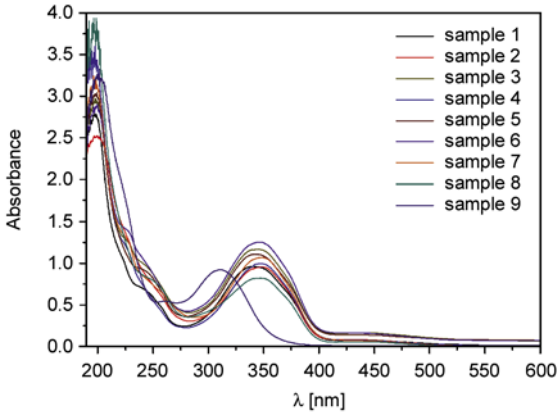

Figure 3. UV-Vis spectra in solid state of azo-polymers

to the methastable *cis* form (higher energy), the *cis-trans* relaxation process is occurring thermally or/and photo-chemically (induced by visible light). In the case of samples 7 and 8 a red-shift displacement of the maximum absorption corresponding to the *trans*-azobenzene isomer can be observed, suggesting some association processes between azo- and 2,4-dinitrophenol groups.

Upon irradiation of the film at 365 nm, the strong absorption band (345 nm) decreases in intensity, reflecting the isomerization process and the *cis*-isomer formation. Based on this absorption band at 345 nm, the percentage of the *cis*-isomer can be calculated and the kinetic curves of the isomerization process can be plotted. In Figure 4, for similar substitution degrees of the polysiloxane and the poly (chloromethyl styrene), the main-chain flexibility influences significantly the photochromic behavior only if the substitution degree is lower than 50% (samples 2 and 4). In the other cases, only the chemical structure of the substituents influences the maximum conversion degree in *cis*-isomer. For

Table 1. Characteristics of the synthesized polymers

Sample no.	Polymer	Substituents	Substitution degree [%]	M_n	T_g [°C]
1	Polysiloxanes	Azobenzene	90	7500	30
2	Polysiloxanes	Azobenzene	46	5900	15
3	PCMS	Azobenzene	82	7320	115
4	PCMS	Azobenzene	45	8800	112
5	Polysiloxanes	Azobenzene 2,4-dinitrophenol	73 22	8000	29
6	PCMS	azobenzene 2,4-dinitrophenol	60 23	6800	123
7	Polysiloxanes	Azobenzene 2,4-dinitrophenol	50 24	7500	23
8	PCMS	Azobenzene 2,4-dinitrophenol	51 26	7000	112
9	Polysiloxanes	2,4-dinitrophenol	56	5900	–

M_n – molecular weight
T_g – glass transition temperature

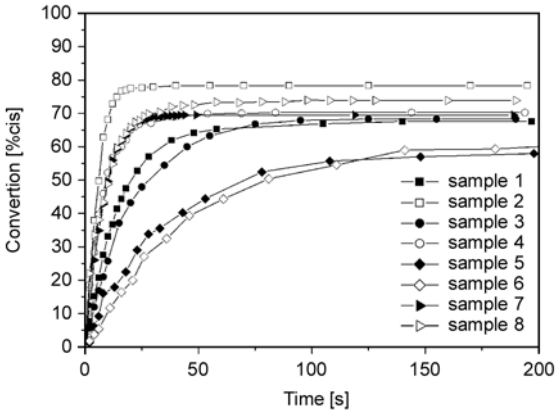

Figure 4. The kinetic curves corresponding to the trans-cis isomerization in solid state of the synthesized azo-polymerst

materials with 2,4-dinitrophenol, a strong difference concerning the maximum *cis*-isomer content and the time constant to reach the plateau value was observed when the azobenzene groups content decreased (samples 5 and 6 compared to samples 7 and 8). An increase of the maximum content of azobenzene molecules in the *cis* form also occurs for the polymers substituted with azobenzene molecules only, when the substitution degree is reduced. However, the isomerization kinetic modifications are smaller for high substitution degrees. For example, the maximum content of azobenzene molecules in the *cis* form can be 11% higher for sample 2 compared to sample 1 while the substitution degree of azobenzene molecules in sample 2 is almost the half of sample 1. Comparison of samples 5 and 7, shows that for equivalent 2,4-dinitrophenol substitution degrees, a similar increase (12%) of the maximum content of azobenzene molecules in the *cis* form results from only a 23% decrease of the azobenzene substitution degree. This suggests some association processes between 2,4-dinitrophenol and azobenzene groups, in agreement with UV-VIS spectral information. To verify this assumption, an associate between samples 2 and 9 (gravimetric ratio 1:1) was prepared, dissolving both polymers in chloroform and evaporating the solvent. Figure 5 shows the difference concerning the photochromic behavior of this associate compared to sample 2. In the case of the associate, the maximum *cis*-isomer content is 44, by 32% lower than that of sample 2.

Sample 9 (a polymer substituted only with 2,4-dinitrophenol) was preferred to verify the association capacity of the azo-polymers, taking into consideration the potential steric hindrance generated by the length differences between azobenzene and 2,4-dinitrophenol groups.

The associations between azo and 2,4-dinitrophenol groups are more evident during the *cis-trans* relaxation processes (Figure 6 and Figure 7). Moreover, the association influences are more evident in the case of the thermal relaxations which take place much slower compared with the visible light induced one. For the visible light induced relaxation in Figure 6, a step-way process was also observed for samples 5 and 6.

This step-way relaxation is very clearly reflected when the cis-trans isomerization is activated only thermally (Figure 6, samples 5 and 6). In the case of samples 7 and 8, the relaxation rate is strongly diminished by the interactions between 2,4-dinitrophenol and azo-groups. Thus, more than 12 and 10 days, respectively, were necessary for samples 7 and 8 to obtain a 100% *trans*-isomer. The samples behavior during relaxation suggests a complicated

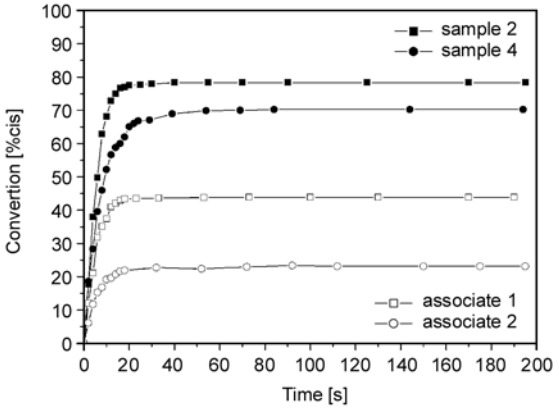

Figure 5. The kinetic curves corresponding to the trans-cis isomerization process (in solid state) of the associate 1 between sample 2 and sample 9, associate 2 between sample 4 and sample 9.

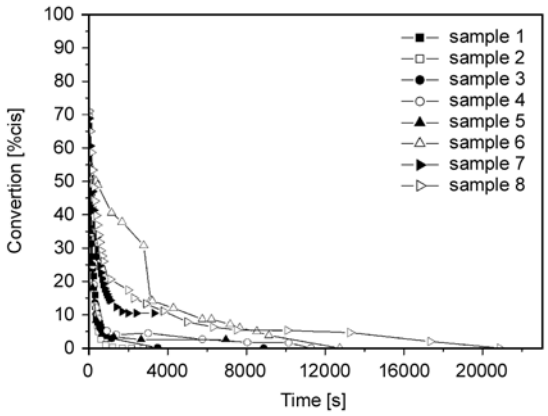

Figure 6. The kinetic curves corresponding to the *cis-trans* relaxation in visible light of azo-polymers

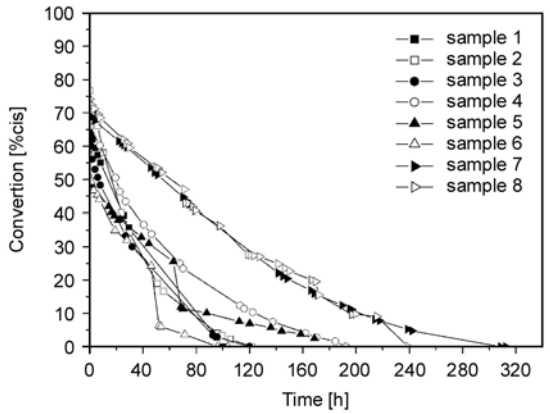

Figure 7. The kinetic curves corresponding to the *cis-trans* thermal relaxation of azo-polymers

chain re-ordering process that imposes supplementary studies.

The complexity of the re-ordering processes was also confirmed by the contact angle measurement. During the azobenzene isomerization, the wettability of the surface was also modified, as a result of geometry and dipole moment changes. Previous molecular modeling studies [32] evidenced a dipole-moment value for the *trans*-azophenol of 1.6 D that increases to 4.5 D in the *cis* configuration. These molecular modeling studies showed the displacement of the azo-groups at the film surface. In addition, we carried out contact angle experiments for the non-irradiated polymeric film and during the relaxation process (Figure 8).

The contact angle values of the non-irradiated sample are placed at $t = 0$ min, the first point after irradiation corresponding to the value $t = 2$ min. After 2 minutes of irradiation, important modifications of the surface properties take place as a consequence of the *trans-cis* isomerization process of the azo-groups.

Another conclusion is connected to the chains re-organization processes; this is more evident in the case of the flexible main-chain polymer, the contact angle value continuously decreasing during the 30–240 min interval, after irradiation. In the case of the rigid main-chain (PCMS) the changing of the surface properties is only the consequence of the dipole-moment increasing from 1.6 to 4.5 D, due to the *trans-cis* isomerization process.

Preliminary studies concerning the nano-structuration capacity under visible laser irradiation (λ = 488 nm) were performed. The typical modulation dynamics representing the evolution of the modulation amplitudes in function of the irradiation time is shown in Figure 9. The curve is obtained by recording with a photodiode the diffracted intensity of a He-Ne laser beam sent onto the irradiated area of the polymer film, during the irradiation as a probe. The 633 nm wavelength of the He-Ne laser was chosen since it is not absorbed by the azobenzene molecules and thus would not perturb the film structuration process.

The curve presented in Figure 9 shows a sigmoidal shape, with a slow increase in the first minutes followed by a rapid increase, reaching finally a plateau value. The slow increase in the first minutes can be related to a periodical re-organization of the azobenzene molecules occurring in the bulk, while for longer irradiation times the increase of the dif-

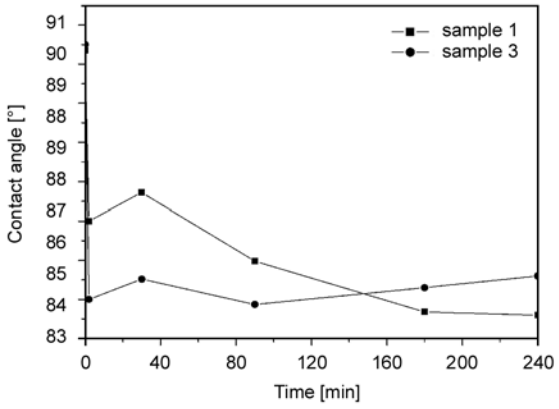

Figure 8. Evolution of contact angle over time for the azo-polysiloxanes and azo-PCMS in dark; non-radiated, 30, 90, 180 and 240 min after irradiation, solvent water (Samples 1 and 3 – Table 1)

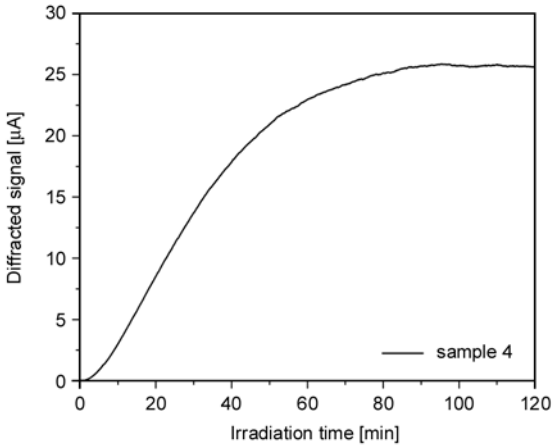

Figure 9. Evolution of the He-Ne laser beam intensity diffracted by a polymer film of sample 4 exposed to an interference pattern in function of the irradiation time. The curve is related to the evolution of the modulation amplitudes recorded in film surface during the irradiation.

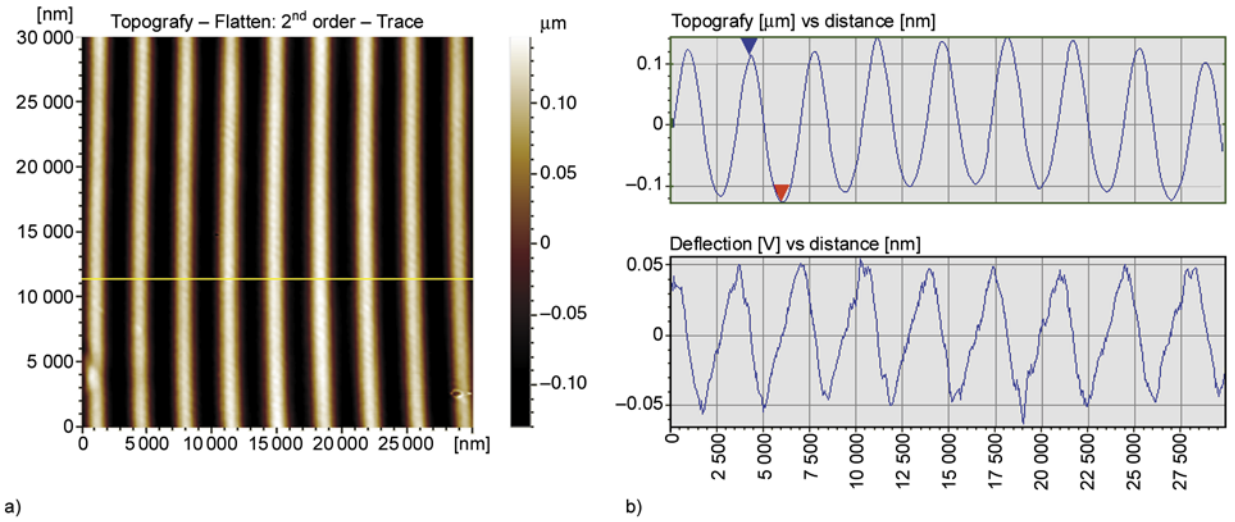

Figure 10. AFM topographic image (a) and cross section (b) of a surface grating induced in a thin film of sample 4 after laser irradiation in the visible range (λ = 488 nm)

fracted intensity has been correlated to an increase of the modulation amplitudes.

When the signal reached the plateau value, the experiment was stopped and the topography of the irradiated surface was characterized by atomic force microscopy (AFM). The next figure shows an image of the surface topography of an irradiated area of the film.

Figure 10 shows a sinusoidal modulation of the film surface, as a result of the excitation, with the interference pattern presenting a sinusoidal modulated intensity profile. The period corresponds to the fringes spacing of the interference pattern, which is set by the θ incidence angle. In the present case gratings with a period of Λ = 3390 nm and a modulation amplitude of Δh = 235 nm were obtained.

The sample with similar azo-benzene content (46%) but having a flexible polymeric main-chain (sample 2) was irradiated under the experimental conditions described above. The He-Ne diffracted intensity-time curve in Figure 11 shows a small increase of the diffracted signal intensity (three orders of magnitude lower than that of the PCMS) limited to the first minutes before a stable signal intensity is reached. AFM measurements confirmed that any surface grating has been inscribed in sample 2. An explanation lays probably in the very low T_g value of this material (T_g = 15°C), which does not allow sufficient stability onto the polymer film, the induced surface deformations being continuously erased at ambient temperature, during the irradiation.

This hypothesis was confirmed by experiments performed on sample 7, with an azobenzene substitution degree close to that of sample 2, but with additional 2,4-dinitrophenol groups (substitution degree 24%). In this case, the material has a T_g close to 23°C, higher than the T_g of sample 2. For this material, we were able to record a variation of the diffracted He-Ne intensity with a similar shape to that of sample 4. The result is illustrated in Figure 12 for both samples and normalized intensities.

The evolution of the diffracted intensities shows a sigmoidal shape for both samples, however, it is important to note that a significantly slower evolution of the intensity is observed for sample 7. Indeed, the saturation is reached after 70 minutes for sample 4, while for sample 7 almost 2 hours are needed.

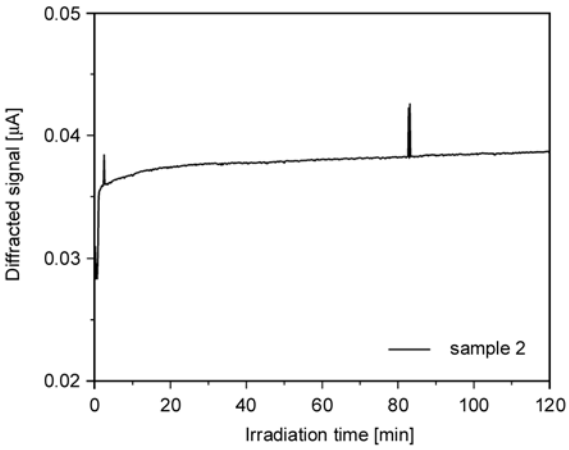

Figure 11. Plot of the He-Ne laser intensity diffracted by the film as a function of irradiation time

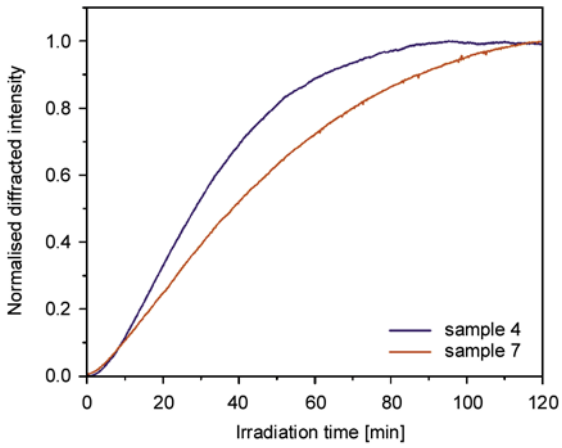

Figure 12. Normalized diffracted He-Ne laser beam intensity in function of the irradiation time for sample 4 and sample 7

A first explanation for this behavior may rely on the polymer chain properties. The different flexibilities of the poly(chloromethyl styrene) and the polysiloxane matrices resulting in different T_g can indeed have strong consequences on the stability of the surface relief grating formation and thus on the efficiency of the process, as highlighted by sample 2. Another possible explanation concerns an effect of association between the 2,4-dinitrophenol and the azobenzene molecules on the *trans-cis-trans* isomerization of the azobenzene, which is the driving force in the nano-structuration process. Indeed, while a direct influence of the 2,4-dinitrophenol additional groups on the azobenzene molecules isomerization is not visible when comparing samples 4 and 7; since these materials present similar *trans* to *cis* conversion kinetics and efficiencies (Figure 4), the photo-induced relaxation appears to be less efficient for sample 7, as evidenced in Figure 5. A reduction of the isomerization complete cycle efficiency is coherent with a slower modulation dynamics for sample 7. As well, the influence of the 2,4-dinitrophenol groups on the flexibility and the conformational reorganization process of the polysiloxane chains around the azobenzene molecules could play an important part in the structuration process. A competition between physical associations occurring in the azo-polymers containing donor/acceptor groups (as evidenced by Figures 4 and 5) and the polymer main chain flexibility is thus expected to take place. The precise identification of the parameters influencing the surface structure is not an easy task and will need further experiments involving azo-polymers with different donor/acceptor groups and substitution degrees, in order to selectively modify each feature of the materials. Additionally, the investigation of the relative contributions of the birefringence grating, resulting from the photo-induced azobenzene molecules angular redistribution, and the surface grating can be an efficient tool in understanding the influence of the material chemical structure on the nano-structuration mechanisms [33–35].

Preliminary tests to determine the ability of the azo-polysiloxanic films to support cell growth were also performed using the HepG2 and HeLa cell lines, of human hepatic and epithelial origin. The films showed remarkable properties to sustain both cell adhesion and proliferation, as revealed by microscopy analysis of the cell cultures at 24 hours post-seeding (Figure 13). Importantly, the films were easily sterilized by incubation in 100% ethanol, for 30 minutes and were stable during all cell culture procedures. These promising results make the azo-polymer films important candidates for future biological applications.

4. Conclusions

The possibility to obtain azo-polymers with flexible or rigid main-chain, containing D/A group was presented. The chemical structure, photochromic behavior and surface nano-structuration capacity of the polymers were characterized. Depending on the chemical structure and the substitution degree, the azo-polymers can generate physical interactions and modify the materials conformational re-organization, after optical excitation, with important consequences on the nano-structure of the azo-polymer films. These associations were evidenced by UV/VIS spectroscopy or by a specific photochromic behavior, especially during the cis-trans relaxation processes. The complex reorganization process after the UV irradiation, especially in the case of flexible main-chain polymers, was evidenced by the photochromic behavior study related to the contact angle measurements. The complex phenomena that take place during the nano-structuration process were reflected in the behavior of three samples during laser irradiation. A significantly faster modulation was observed in the case of PCMS rigid main-chain, suggesting that interactions between azo-benzene and dinitro-phenol groups coupled to

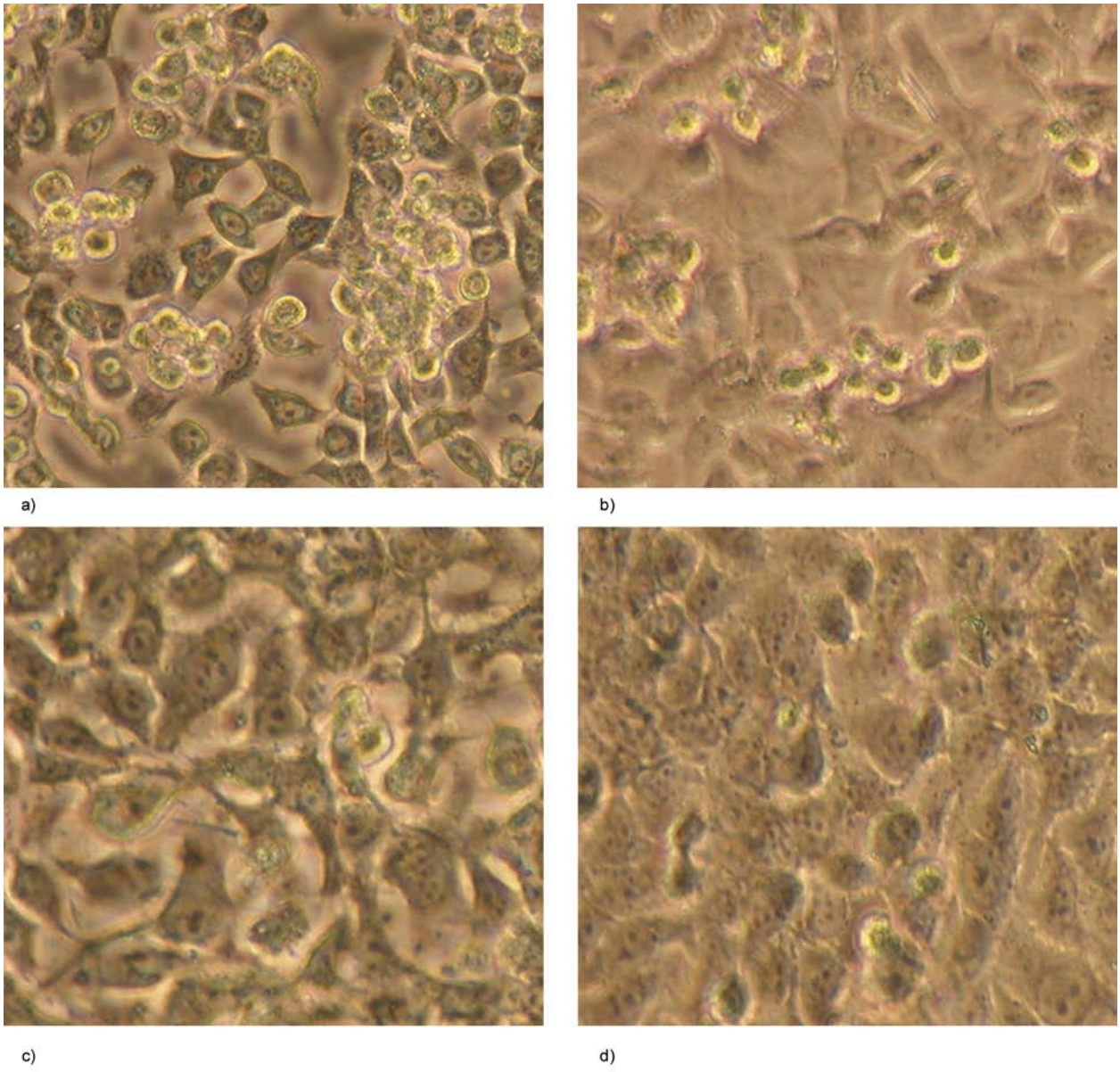

Figure 13. Equal number of HepG2 (a, b) and HeLa (c, d) cells were seeded on either azo-polymer (Sample 1) film (a, c) or microscope cover glass, as control (b, d). Cell development was visualized at 24 hours post-seeding, using an inverted microscope (20× magnification).

supplementary re-ordering phenomena permitted by the chain flexibility in polysiloxane based azo-polymers can play an important role in the differences observed on the relief formation processes. The first results reported on the nano-structuration properties are promising, as concerns the use of additional donor/acceptor groups to control the structuration properties of flexible azo-polysiloxanes films. These preliminary experiments represent a first step towards the development of materials with high sensitivity to optical stimulation, due to a flexible polymer backbone, and efficient and stable structure properties, at the same time. A better understanding of the phenomena involved azo-polysiloxanes will require further optimization studies regarding the nano-structuration properties of such polymer films. Preliminary tests to determine the ability of the azo-polysiloxanic films to support cell growth were performed. The films showed remarkable properties to sustain both cell adhesion and proliferation. These promising results make the azo-polymer films important candidates for future biological applications.

Acknowledgements

The Romanian authors want to thank to ANCS for financial support of this research (Grant CEA - C1- 01/2010) and to project BRAIN "Doctoral scholarships as an investment in intelligence", financed by the European Social Found and Romanian Government

References

[1] Feng C. L., Zhang Y. J., Jin J., Song Y. L., Xie L. Y., Qu G. R., Jiang L., Zhu D. B.: Reversible wettability of photoresponsive fluorine-containing azobenzene polymer in langmuir−blodgett films. Langmuir, **17**, 4593–4597 (2001).
DOI: 10.1021/la010071r

[2] Jiang W., Wang G., He Y., Wang X., An Y., Song Y., Jiang L.: Photo-switched wettability on an electrostatic self-assembly azobenzene monolayer. Chemical Communications, **2005**, 3550–3552 (2005).
DOI: 10.1039/B504479K

[3] Lim H. S., Han J. T., Kwak D., Jin M., Cho K.: Photoreversibly switchable superhydrophobic surface with erasable and rewritable pattern. Journal of the American Chemical Society, **128**, 14458–14459 (2006).
DOI: 10.1021/ja0655901

[4] Cao H. Z., Zhang W., Zhu J., Chen X. R., Cheng Z. P., Wu J. H., Zhu X. L.: Azo polymers with electronical push and pull structures prepared via RAFT polymerization and its photoinduced birefringence behavior. Express Polymer Letters, **2**, 589–601 (2008).
DOI: 10.3144/expresspolymlett.2008.71

[5] Zhao X. Y., Wang M. Z.: Structure dependence of photochromism and thermochromism of azobenzene-functionalized polythiophenes. Express Polymer Letters, **1**, 450–455 (2007).
DOI: 10.3144/expresspolymlett.2007.63

[6] Wang G., Tong X., Zhao Y.: Preparation of azobenzene-containing amphiphilic diblock copolymers for light-responsive micellar aggregates. Macromolecules, **37**, 8911–8917 (2004).
DOI: 10.1021/ma048416a

[7] Moleavin I., Grama S., Cârlescu I., Scutaru D., Hurduc N.: Photosensitive micelles based on polysiloxanes containing azobenzene moieties. Polymer Bulletin, **65**, 69–81 (2010).
DOI: 10.1007/s00289-010-0247-4

[8] Jiang X., Wang H., Chen X., Li X., Lei L., Mu J., Wang G., Zhang S.: A novel photoactive hyperbranched poly(aryl ether ketone) with azobenzene end groups for optical storage applications. Reactive and Functional Polymers, **70**, 699–705 (2010).
DOI: 10.1016/j.reactfunctpolym.2010.06.005

[9] Natansohn A., Rochon P.: Photoinduced motions in azo-containing polymers. Chemical Reviews, **102**, 4139–4175 (2002).
DOI: 10.1021/cr970155y

[10] Pan X., Wang C., Xu H., Wang C., Zhang X.: Polarization holographic gratings in an azobenzene side-chain liquid-crystalline polymer. Applied Physics B: Lasers and Optics, **86**, 693–697 (2007).
DOI: 10.1007/s00340-006-2482-9

[11] Wu S., Yao S., She W., Luo D., Wang H.: All-optical switching properties of poly(methyl methyacrylate) azobenzene composites. Journal of Materials Science, **38**, 401–405 (2003).
DOI: 10.1023/A:1021878710507

[12] Ikeda T., Tsutsumi O.: Optical switching and image storage by means of azobenzene liquid-crystal films. Science, **268**, 1873–1875 (1995).
DOI: 10.1126/science.268.5219.1873

[13] Berg R. H., Hvilsted S., Ramanujam P. S.: Peptide oligomers for holographic data storage. Nature, **383**, 505–508 (1996).
DOI: 10.1038/383505a0

[14] Dürr H., Bouas-Laurent H.: Photochomism: Molecules and systems. Elsevier, Amsterdam (2003).

[15] Xue X., Zhu J., Zhang Z., Zhou N., Zhu X.: Synthesis and photoresponsive behavior of the high-T_g azobenzene polymers via RAFT polymerization. Reactive and Functional Polymers, **70**, 456–462 (2010).
DOI: 10.1016/j.reactfunctpolym.2010.04.006

[16] Pei S., Chen X., Wang F., Jiang Z., Peng W.: Dynamics of the photo-induced orientation and relaxation of a novel hyperbranched poly(aryl ether) containing azobenzene groups. Laser Physics, **20**, 1144–1148 (2010).
DOI: 10.1134/S1054660X1009015X

[17] Sun M., Que W., Hu X.: Preparation and *trans–cis* isomerization of azobenzene-containing TiO_2/ormosils hybrid films derived at a low temperature sol–gel process for photonic applications. Journal of Sol-Gel Science and Technology, **50**, 415–420 (2009).
DOI: 10.1007/s10971-009-1918-1

[18] Bobrovsky A., Shibaev V., Hamplova V., Kaspar M., Glogarova M.: Chirooptical and photooptical properties of a novel side-chain azobenzene-containing LC polymer. Monatshefte für Chemie, **140**, 789–799 (2009).
DOI: 10.1007/s00706-009-0108-8

[19] Kumar G. S., Neckers D. C.: Photochemistry of azobenzene-containing polymers. Chemical Reviews, **89**, 1915–1925 (1989).
DOI: 10.1021/cr00098a012

[20] Rochon P., Batalla E., Natansohn A.: Optically induced surface gratings on azoaromatic polymer films. Applied Physics Letters, **66**, 136–138 (1995).
DOI: 10.1063/1.113541

[21] Kim D. Y., Tripathy S. K., Li L., Kumar J.: Laser-induced holographic surface relief gratings on nonlinear optical polymer films. Applied Physics Letters, **66**, 1166–1168 (1995).
DOI: 10.1063/1.113845

[22] Sobolewska A., Miniewicz A., Grabiec E., Sek D.: Holographic grating recording in azobenzene functionalized polymers. Central European Journal of Chemistry, **4**, 266–284 (2006).
DOI: 10.2478/s11532-006-0003-7

[23] Hubert C., Fiorini-Debuisschert C., Hassiaoui I., Rocha L., Raimond P., Nunzi J-M.: Emission properties of an organic light-emitting diode patterned by a photoinduced autostructuration process. Applied Physics Letters, **87**, 191105–191107 (2005).
DOI: 10.1063/1.2126793

[24] Cocoyer C., Rocha L., Sicot L., Geffroy B., de Bettignies R., Sentein C., Fiorini-Debuisschert C., Raimond P.: Implementation of submicrometric periodic surface structures toward improvement of organic-solar-cell performances. Applied Physics Letters, **88**, 133108–133110 (2006).
DOI: 10.1063/1.2188600

[25] Choi C-H., Heydarkhan-Hagvall S., Wu B. M., Dunn J. C. Y., Beygui R. E., Kim C-J.: Cell growth as a sheet on three-dimensional sharp-tip nanostructures. Journal of Biomedical Materials Research Part A, **89**, 804–817 (2009).
DOI: 10.1002/jbm.a.32101

[26] Karageorgiev P., Neher D., Schulz B., Stiller B., Pietsch U., Giersig M., Brehmer L.: From anisotropic photo-fluidity towards nanomanipulation in the optical near-field. Nature Materials, **4**, 699–703 (2005).
DOI: 10.1038/nmat1459

[27] Hubert C., Malcor E., Maurin I., Nunzi J-M., Raimond P., Fiorini C.: Microstructuring of polymers using a light-controlled molecular migration processes. Applied Surface Science, **186**, 29–33 (2002).
DOI: 10.1016/S0169-4332(01)00658-4

[28] Rocha L., Dumarcher V., Malcor E., Fiorini C., Denis C., Raimond P., Geffroy B., Nunzi J-M.: Photo-induced microstructured polymers for the optimisation and control of organic devices emission properties. Synthetic Metals, **127**, 75–79 (2002).
DOI: 10.1016/S0379-6779(01)00599-9

[29] Hurduc N., Enea R., Scutaru D., Sacarescu L., Donose B. C., Nguyen A. V.: Nucleobases modified azo-polysiloxanes, materials with potential application in biomolecules nanomanipulation. Journal of Polymer Science Part A: Polymer Chemistry, **45**, 4240–4248 (2007).
DOI: 10.1002/pola.22165

[30] Enea R., Resmerită A-M., Petraru L., Grigoraş C., Scutaru D., Simionescu C. I., Hurduc N.: Synthesis and photochromic behavior of some azo-polysiloxanes modified with nucleobases or donor-acceptor groups. Central European Journal of Chemistry, **5**, 981–995 (2007).
DOI: 10.2478/s11532-007-0042-8

[31] Bian S., Li L., Kumar J., Kim D. Y., Williams J., Tripathy S. K.: Single laser beam-induced surface deformation on azobenzene polymer films. Applied Physics Letters, **73**, 1817–1819 (1998).
DOI: 10.1063/1.122292

[32] Resmerita A-M., Epure L., Hurduc N., Adès D., Siove A.: Surface properties, thermal behavior, and molecular simulations of azo-polysiloxanes under light stimuli. Insight into the relaxation. Macromolecular Research, **8**, 721–729 (2010).
DOI: 10.1007/s13233-010-0806-4

[33] Holme N. C. R., Nikolova L., Ramanujam P. S., Hvilsted S.: An analysis of the anisotropic and topographic gratings in a side-chain liquid crystalline azobenzene polyester. Applied Physics Letters, **70**, 1518–1520 (1997).
DOI: 10.1063/1.118605

[34] Lagugné Labarthet F., Buffeteau T., Sourisseau C.: Analyses of the diffraction efficiencies, birefringence, and surface relief gratings on azobenzene-containing polymer films. The Journal of Physical Chemistry B, **102**, 2654–2662 (1998).
DOI: 10.1021/jp980050e

[35] Sobolewska A., Miniewicz A.: Analysis of the kinetics of diffraction efficiency during the holographic grating recording in azobenzene functionalized polymers. The Journal of Physical Chemistry B, **111**, 1536–1544 (2007).
DOI: 10.1021/jp067021l

eXPRESS Polymer Letters Vol.5, No.11 (2011) 970–976
Available online at www.expresspolymlett.com
DOI: 10.3144/expresspolymlett.2011.95

Electron beam immobilization of functionalized poly(vinyl methyl ether) thin films on polymer surfaces – Towards stimuli responsive coatings for biomedical purposes

S. Gramm[1,2*], *J. Teichmann*[1,2,3], *M. Nitschke*[1,2], *U. Gohs*[1], *K.-J. Eichhorn*[1], *C. Werner*[1,2,4]

[1]Leibniz Institute of Polymer Research Dresden, Hohe Str. 6, 01069 Dresden, Germany
[2]Max Bergmann Center of Biomaterials Dresden, Budapester Str. 27, 01069 Dresden, Germany
[3]University Hospital Dresden Carl Gustav Carus, Anatomy, Fetscherstr. 74, 01307 Dresden, Germany
[4]Center for Regenerative Therapies Dresden, Tatzberg 47, 01187 Dresden, Germany

Received 17 March 2011; accepted in revised form 19 May 2011

Abstract. Thin films of poly(vinyl methyl ether) (PVME) were immobilized on polystyrene surfaces by low energy electron beam cross-linking. Structure retention as well as the thermo-responsive swelling behavior in aqueous media were studied by attenuated total reflection Fourier transform infrared spectroscopy (ATR-FTIR) and spectroscopic ellipsometry respectively. The physical properties of the thermo-responsive coatings can be controlled in a wide range by adjusting the irradiation parameters. To allow for a variety of biomolecular functionalization strategies, the concept was extended by adding reactive sites to the system. For that purpose a mixture of PVME and the copolymer of PVME and maleic acid was applied, that possesses a similar stimuli-responsive behavior.

Keywords: *polymer gels, stimuli responsive polymers, poly(vinyl methyl ether), maleic anhydride, low energy electrons*

1. Introduction

Stimuli responsive polymers (SRP) are materials that exhibit dramatic changes of their properties upon slight changes in the environmental conditions [1, 2]. For biomedical purposes surface-immobilized SRP films with a thermally stimulated phase transition close to the physiological range are of particular interest [3]. When immersed in aqueous media, the abrupt change in solubility at the lower critical solution temperature (LCST) leads to a reversible swelling and collapsing of the immobilized film upon small temperature changes [4]. To meet the specific requirements for sophisticated applications like the control of cell surface adhesion, there is a strong need to fine-tune the physicochemical properties of the SRP coating [5, 6]. While the most popular thermo-responsive material for this purpose is poly(N isopropylacrylamide) (PNiPAAm, LCST = 32°C) [7, 8], the approach reported here is based on poly(vinyl methyl ether) (PVME, LCST = 34°C) [9, 10]. The distinct thermo-responsive behavior with a LCST only a few Kelvin below the standard cell cultivation temperature predestines PVME as a coating for thermo-responsive cell culture carriers. However, there are only few studies on the application of polyvinylether based hydrogels for this purpose [11]. Contrary to PNiPAAm, PVME possesses a high affinity to electron beam cross-linking [12, 13]. This allows to immobilize PVME films on polymeric substrates like polystyrene with a defined thickness and swelling behavior in wide range.

Beyond that, the functional modulation of a thermo-responsive coating with bioactive molecules can

*Corresponding author, e-mail: gramm@ipfdd.de

further improve the performance. Hatakeyama *et al*. demonstrate the promotion of cell adhesion and proliferation on thin PNiPAAm films by the immobilization of cell adhesive peptides and growth factors [14]. On the other hand, Kwon *et al*. [15] show the acceleration of cell detachment from PNiPAAm-based cell culture carriers by the introduction of poly(ethylene glycol) chains. Altogether, these strategies allow to adjust initial adhesion and detachment properties for a particular type of cell culture. Towards this goal, PVME-based thermo-responsive coatings can be chemically functionalized by cross-linking as a mixture with other (co)polymers. In particular, the introduction of anhydride moieties allows for a number of biomolecular functionalization strategies without toxic coupling agents [16]. This is demonstrated for the binding of laminin and chondroitin-6-sulphate to promote initial cell attatchment of immortalized, adult human corneal endothelial cells (HCEC). This cell type established by Bednarz *et al*. [17] and further characterized by Valtink *et al*. [18] was cultivated on maleic anhydride (MA) functionalized SRP substrates either with covalently bound or physisorbed proteins.

2. Experimental

2.1. Materials and sample preparation

For the experiments of this work two SRP materials were investigated (Figure 1): i) Poly(vinyl methyl ether) (TCI Europe, Zwijndrecht, Belgium) and ii) a mixture of PVME and the alternating copolymer of PVME and maleic anhydride (Sigma-Aldrich, Munich, Germany) with a copolymer content of 10% wt/wt (PVME-MA). Electron beam irradiation was carried out with the low energy electron facility ADU (Advanced Electron Beams, Wilmington, USA) under nitrogen atmosphere at room temperature. The electron energy of 150 keV corresponds to a maximum penetration depth of about 200 μm in polymeric materials.

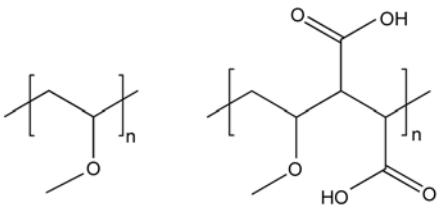

Figure 1. Poly(vinyl methyl ether) and poly(vinyl methyl ether–co–maleic acid)

To study the effect of electron beam cross-linking on the structure of the SRP, thin films of about 70 nm were applied by spin coating (solution 2% wt/wt in methanol, 2000 rpm, 1500 rpm/s, 30 s) onto internal reflection elements for ATR-FTIR spectroscopy. Subsequently, the samples were irradiated with an absorbed dose of 260 kGy in 11 steps in order to reduce temperature increase during electron treatment.

To allow *in situ* investigations of the swelling behavior of immobilized SRP layers by spectroscopic ellipsometry, polystyrene coated silicon wafers were used as substrates for the experiments of this work. For that purpose polystyrene coatings (PS, type 148H, BASF, Ludwigshafen, Germany) of about 30 nm thickness were applied by spin coating onto silicon wafers 15×20 mm^2 (solution 1% wt/wt in toluene, 2000 rpm, 1500 rpm/s, 30 s). PS surfaces were treated in air plasma to obtain an appropriate wetting behavior (Harrick Plasma Cleaner PDC 002, 1 min). Subsequently, a SRP layer was prepared by spin coating (solution 2% wt/wt in methanol, 2000 rpm, 1500 rpm/s, 30 s) on top of the PS film. The samples were irradiated with different absorbed doses (118–780 kGy) in steps of 23.6 kGy in order to reduce the temperature increase during electron treatment. Finally, they were rinsed in water to remove unbound material. For the cell culture experiments cover slips (Menzel-Gläser, Braunschweig, Germany) with a diameter of 20 mm were used instead of silicon wafers.

2.2. Spectroscopic ellipsometry

Ellipsometric measurements were performed using a variable angle spectroscopic ellipsometer M-2000VI (J. A. Woollam Co., Inc., Lincoln, USA). It is a Diode Array Rotating Compensator Ellipsometer (DARCE™) in polarizer compensator sample analyzer configuration equipped with a computer-controlled goniometer and a horizontally mounted sample stage. The light source is a 50 W mercury lamp. For a given angle of incidence, the M-2000VI measures 500 wavelengths simultaneously covering the spectral range from 370–1700 nm. Accurate measurements over the full Δ and Ψ range were acquired ($\Delta = 0°–360°$; $\Psi = 0°–90°$).

In case of dry samples, values from three angles of incidence, 65, 70 and 75° were acquired. To investigate swollen hydrogel layers, a liquid media cell

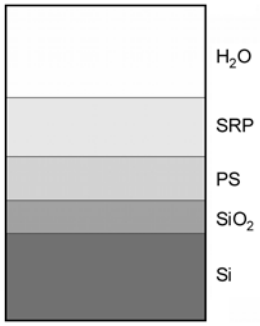

Figure 2. Multilayer model for ellipsometric investigations

(angle of incidence 68°) with de-ionized water (pH 6.5) was used. For the variation of temperature with a rate of 1 K·min^{-1}, a computer-controlled heating device for the liquid media cell was used.

To calculate the thickness and the optical properties of the polymer films under investigation, fit procedures based on Cauchy multilayer models were applied to the the ellipsometric data (Figure 2). An effective medium approximation was used in case of swollen hydrogel layers.

The swelling degree was calculated as $Q = d_T/d_{dry}$, were d_T corresponds to the swollen film thickness at a given temperature and d_{dry} to the dry film thickness.

2.3. Infrared spectroscopy

FTIR-ATR spectra were obtained with a Vector 22 FTIR spectrometer (Bruker, Ettlingen, Germany) using trapezoidal shaped internal reflection elements (IRE) made of chalcogenide glass IRG100 [19] with 45° incident angle and 17 reflections (9 effective reflections on the coated side). Sample spectrum and background spectrum were acquired with the coated IRE and the clean IRE respectively. For the film thickness used in this work, the thin-film case of ATR spectroscopy applies [20]. In this case the film thickness limits the sampling depth, i.e., there is no variation of the sampling depth with wavelength. Consequently, absorbance units are given instead of ATR units.

2.4. Cell cultivation

Sterilization of the SRP-coated cover slips was performed by incubating for 24 h in 0.02% ProClin® 300 Preservative (Supleco, Sigma-Aldrich, Munich, Germany) diluted in phosphate buffered saline (PBS, w/o Mg^{2+}, Ca^{2+}) at room temperature, followed by a rinsing step and incubation in PBS (w/o Mg^{2+}, Ca^{2+}) for 24 h. MA containing surfaces were either tempered under sterile conditions overnight at 90°C to activate the MA moieties witch allows the covalent binding of proteins. Control surfaces were not tempered which allows only physisorptive protein binding. The samples were incubated for 2 h at 37°C with the protein mixture of 10 mg/ml laminin (Invitrogen, Karlsruhe, Germany) and 10 mg/ml chondroitin-6-sulphate (Sigma-Aldrich, Munich, Germany). Then samples were rinsed with pre-warmed PBS (w/o Mg^{2+}, Ca^{2+}) and conditioned with the growth medium for 30 min. Finally, cells were seeded at a density of 5000 cells per cm^2.

They were grown serum-supplemented in $F99_{HCEC}$ [Nutrient Mixture Ham's F12/Medium 199 (Biochrom AG, Berlin, Germany) with 5% FCS (Invitrogen), 20 mg/ml ascorbic acid (Sigma-Aldrich), 10 ng/ml human recombinant FGF-2 (Invitrogen), 20 mg/ml human recombinant insulin (Sigma-Aldrich) and antibiotics (2.5 mg/ml amphotericin B and 50 mg/ml gentamycin; Biochrom)] at 37°C and 5% CO_2.

3. Results and discussion

Figure 3 shows the efficiency of PVME immobilization as a function of the absorbed dose. At an absorbed dose of at least 500 kGy the material of a pre-deposited PVME thin film is fully immobilized on a polystyrene carrier. For lower dose values a part of the pre-deposited and electron beam irradiated PVME is removed when immersed in distilled water. However, the known fraction according to

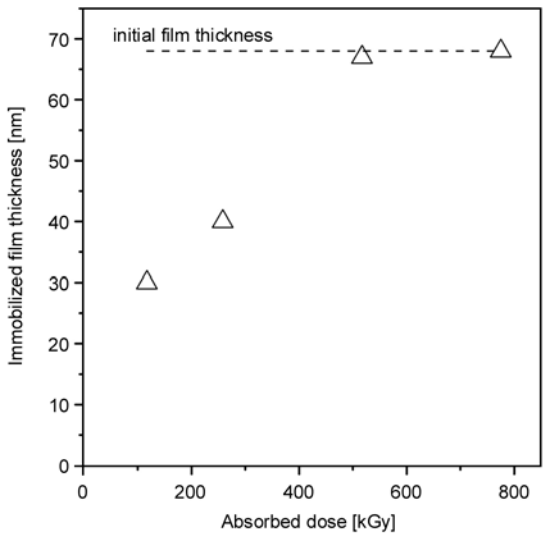

Figure 3. Efficiency of PVME immobilization on polystyrene as a function of absorbed dose

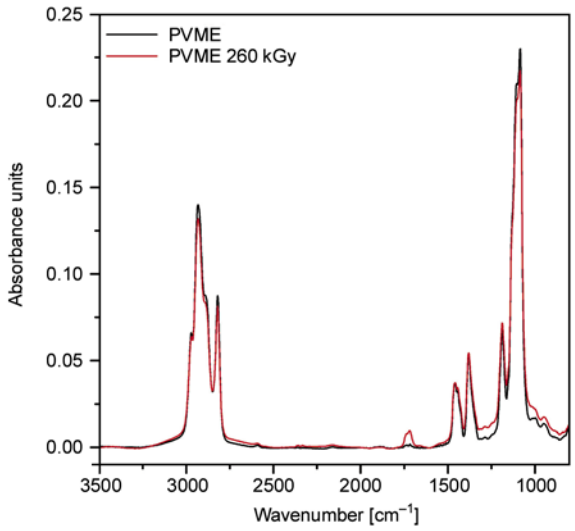

Figure 4. Infrared spectra of non-irradiated and irradiated PVME

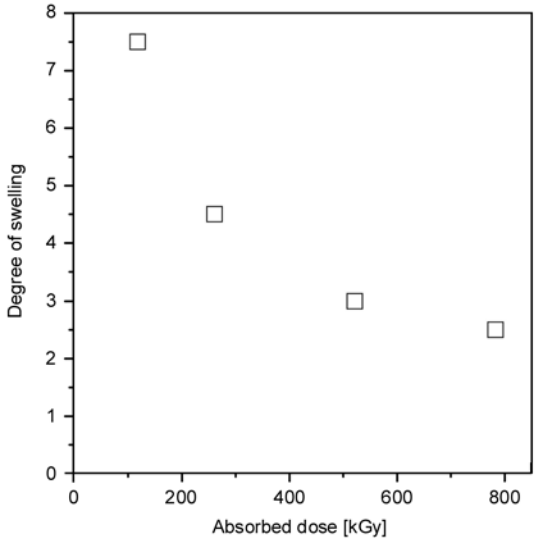

Figure 6. Degree of swelling of immobilized PVME thin films at 15°C depending on the absorbed dose

Figure 3 allows to prepare a coating with a given thickness of the immobilized material.

The structure retention of the PVME upon electron beam immobilization was proven by infrared spectroscopy. Figure 4 compares the spectra of non-irradiated and irradiated PVME. The only significant difference is the appearance of a C=O stretching band at 1720 cm^{-1} which is attributed to oxidative degradation of PVME due to post reaction of persistent radicals formed as a result of the irradiation.

Figure 5 illustrates the temperature dependent swelling behavior of immobilized PVME thin films as determined by spectroscopic ellipsometry. Irrespective of the applied dose, the material shows a thermo-responsive effect with a critical temperature

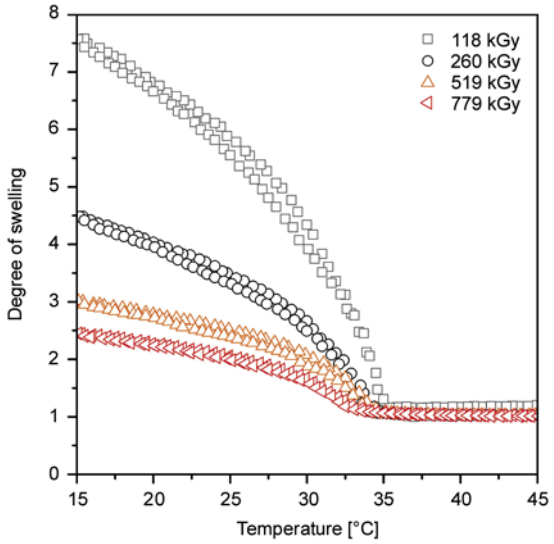

Figure 5. Temperature dependent swelling behavior of immobilized PVME thin fims during heating and cooling

of about 34°C. While all films are fully collapsed above this threshold, a dose dependent degree of swelling is found when cooling down the system. For a lower absorbed dose, i.e. for a lower degree of cross-linking of the hydrogel, the degree of swelling increases (Figure 6). Furthermore, the onset of the swelling gets sharper and more pronounced while the gradient of the swelling curve slightly below the critical temperature increases significantly. The temperature dependent swelling is fully reversible for all cases investigated. The process does not show a pronounced hysteresis, i.e. heating and cooling curves are virtually the same. The water is fully expelled in the collapsed state (degree of swelling = 1). Both facts set apart PVME from PNiPAAm and NiPAAm containing copolymers as investigated in previous studies [4, 21]. The influence of the cell culture medium to the transition behavior is expected to lower the transition temperature by 1–2 K [22]. The shown behavior of PVME thin films on polystyrene substrates corroborate the results of Hegewald *et al*. [23] obtained for thicker layers of PVME directly prepared on silicon oxide surfaces.

To allow for biomolecular functionalization of the thermo-responsive coating described so far, a mixture of PVME and the copolymer of PVME and maleic acid (PVME-MA) was immobilized and characterized in the same way. Figure 7 illustrates, that the thermo-responsive behavior of the system is largely preserved when adding 10% wt/wt of the functional copolymer. The acid groups in the immobilized film can be transformed into anhydride moi-

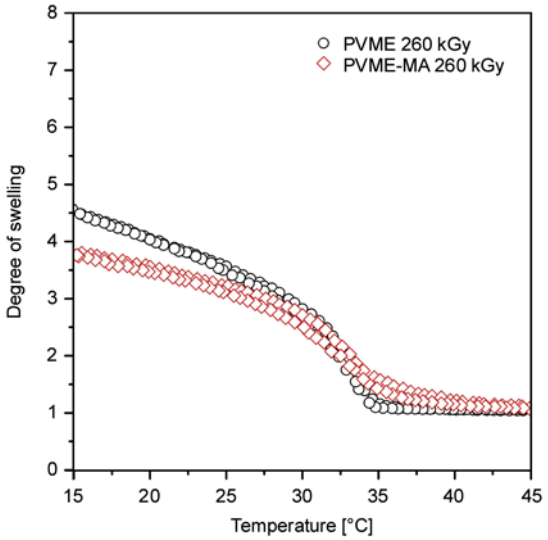

Figure 7. Changes in the temperature dependent swelling behavior of immobilized PVME after adding 10% wt/wt PVME-MA

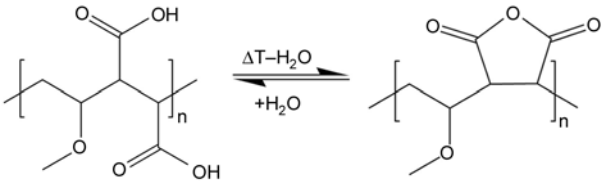

Figure 8. Example of the anhydride formation in the added copolymer

eties when stored at 120°C for 2 h (Figure 8). This was proven by infrared spectroscopy (Figure 9). The band at 1725 cm^{-1} (C=O stretching in COOH) is gradually disappearing and replaced by two bands at 1775 and 1860 cm^{-1} (C=O stretching of cyclic anhydrides) [24].

The restored anhydride moieties are now available for further biomolecular modifications with extracellular matrix proteins, peptides or amino end group functionalized polyethylene glycols. This allows to precisely adjust the physicochemical characteristic

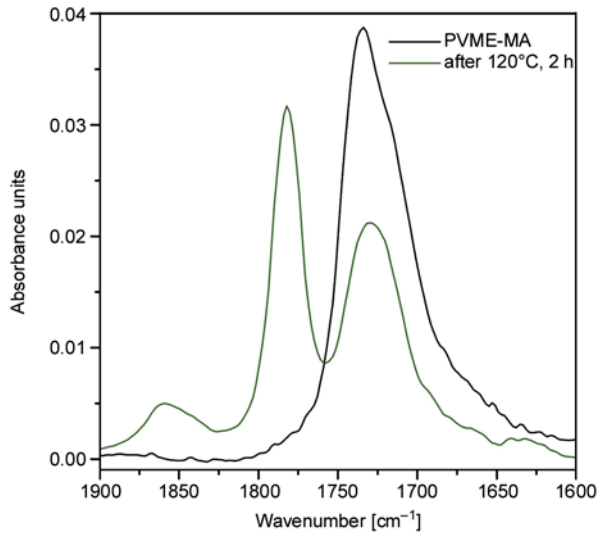

Figure 9. Infrared spectra of immobilized PVME-MA before and after storage at 120°C for 2 h

of the surface for enhanced adhesion and proliferation or accelerated detachment of cultured cells.

The enhanced adhesion after the covalent decoration is demonstrated in Figure 10. It shows the adhesion and growth of HCEC after two days of cultivation on a blend SRP layer of PVME and 10% wt/wt PVME-MA (33 nm dry thickness, 260 kGy absorbed dose) with physisorptive and covalent binding of laminin and chondroitin-6-sulfate.

4. Conclusions

Thin films of the thermo-responsive polymer poly (vinyl methyl ether) were immobilized on polystyrene, the most common material for cell culture carriers. The high affinity to electron beam crosslinking allows to tailor the properties of the PVME films easily. Stable coatings with a dry thickness up to 100 µm can be achieved using an electron energy of 150 keV. The swelling behavior of the immobilized PVME films can be adjusted by variation of

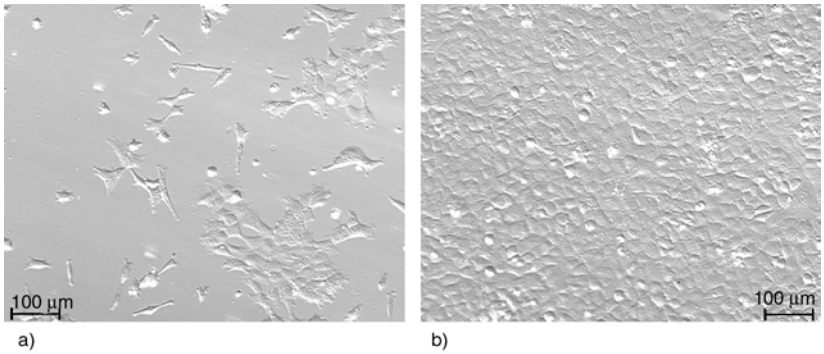

Figure 10. Adhesion and growth of HCEC after two days of cultivation on a blend SRP layer of PVME and 10% wt/wt PVME-MA (33 nm dry thickness, 260 kGy absorbed dose) with physisorptive (a) and covalent binding (b) of laminin and chondroitin-6-sulfate

the absorbed dose. Systems with a critical temperature of 34°C and a different cross-linking corresponding to a degree of swelling between 2.5 and 7.7 were demonstrated. The variability of the mechanical properties of the thermo responsive coating is complemented with a chemical functionalization by introducing a copolymer carrying reactive anhydride sites. This approach combines the concept of thermo responsive cell culture carriers with an anhydride-based platform technology for biomolecular modification.

Acknowledgements

This work was supported by the European Regional Development Fund, project 4212/09 15. The authors thank Roland Schulze (IPF Dresden) for ellipsometry measurements and Michael Spaethe (IPF Dresden) for operating the electron beam irradiation setup.

References

[1] de las Heras Alarcón C., Pennadam S., Alexander C.: Stimuli responsive polymers for biomedical applications. Chemical Society Reviews, **34**, 276–285 (2005). DOI: 10.1039/b406727d

[2] Mendes P. M.: Stimuli-responsive surfaces for bio-applications. Chemical Society Reviews, **37**, 2512–2529 (2008). DOI: 10.1039/b714635n

[3] Yamato M., Akiyama Y., Kobayashi J., Yang J., Kikuchi A., Okano T.: Temperature-responsive cell culture surfaces for regenerative medicine with cell sheet engineering. Progress in Polymer Science, **32**, 1123–1133 (2007). DOI: 10.1016/j.progpolymsci.2007.06.002

[4] Schmaljohann D., Beyerlein D., Nitschke M., Werner C.: Thermo-reversible swelling of thin hydrogel films immobilized by low-pressure plasma. Langmuir, **20**, 10107–10114 (2004). DOI: 10.1021/la034653f

[5] Da Silva R. M. P., Mano J. F., Reis R. L.: Smart thermoresponsive coatings and surfaces for tissue engineering: Switching cell-material boundaries. Trends in Biotechnology, **25**, 577–583 (2007). DOI: 10.1016/j.tibtech.2007.08.014

[6] Rzaev Z. M. O., Dinçer S., Pişkin E.: Functional copolymers of *N*-isopropylacrylamide for bioengineering applications. Progress in Polymer Science, **32**, 534–595 (2007). DOI: 10.1016/j.progpolymsci.2007.01.006

[7] Schild H. G.: Poly(*N*-isopropylacrylamide): Experiment, theory and application. Progress in Polymer Science, **17**, 163–249 (1992). DOI: 10.1016/0079-6700(92)90023-R

[8] Cooperstein M. A., Canavan H. E.: Biological cell detachment from poly(*N*-isopropyl acrylamide) and its applications. Langmuir, **26**, 7695–7707 (2010). DOI: 10.1021/la902587p

[9] Hegewald J., Schmidt T., Gohs U., Günther M., Reichelt R., Stiller B., Arndt K-F.: Electron beam irradiation of poly(vinyl methyl ether) films: 1. Synthesis and film topography. Langmuir, **21**, 6073–6080 (2005). DOI: 10.1021/la0502589

[10] Schäfer-Soenen H., Moerkerke R., Berghmans H., Koningsveld R., Dušek K., Šolc K.: Zero and off-zero critical concentrations in systems containing polydisperse polymers with very high molar masses. 2. The system water-poly(vinyl methyl ether). Macromolecules, **30**, 410–416 (1997). DOI: 10.1021/ma960114o

[11] Karakeçili A. G., Satrianob C., Gümüşderelioğlu M., Marletta G.: Thermoresponsive and bioactive poly (vinyl ether)-based hydrogels synthesized by radiation copolymerization and photochemical immobilization. Radiation Physics and Chemistry, **77**, 154–161 (2008). DOI: 10.1016/j.radphyschem.2007.04.014

[12] Janik I., Kasprzak E., Al-Zier A., Rosiak J. M.: Radiation crosslinking and scission parameters for poly (vinyl methyl ether) in aqueous solution. Nuclear Instruments and Methods in Physics Research Section B: Beam Interactions with Materials and Atoms, **208**, 374–379 (2003). DOI: 10.1016/S0168-583X(03)00897-8

[13] McHerron D. C., Wilkes G. L.: Electron beam irradiation of polystyrene-poly(vinyl methyl ether) blends. Polymer, **34**, 3976–3985 (1993). DOI: 10.1016/0032-3861(93)90657-V

[14] Hatakeyama H., Kikuchi A., Yamato M., Okano T.: Bio-functionalized thermoresponsive interfaces facilitating cell adhesion and proliferation. Biomaterials, **27**, 5069–5078 (2006). DOI: 10.1016/j.biomaterials.2006.05.019

[15] Kwon O. H., Kikuchi A., Yamato M., Okano T.: Accelerated cell sheet recovery by co-grafting of PEG with PIPAAm onto porous cell culture membranes. Biomaterials, **24**, 1223–1232 (2003). DOI: 10.1016/S0142-9612(02)00469-6

[16] Pompe T., Zschoche S., Herold N., Salchert K., Gouzy M-F., Sperling C., Werner C.: Maleic anhydride copolymers – A versatile platform for molecular biosurface engineering. Biomacromolecules, **4**, 1072–1079 (2003). DOI: 10.1021/bm034071c

[17] Bednarz J., Teifel M., Friedl P., Engelmann K.: Immortalization of human corneal endothelial cells using electroporation protocol optimized for human corneal endothelial and human retinal pigment epithelial cells. Acta Ophthalmologica Scandinavica, **78**, 130–136 (2000). DOI: 10.1034/j.1600-0420.2000.078002130.x

[18] Valtink M., Gruschwitz R., Funk R. H. W., Engelmann K.: Two clonal cell lines of immortalized human corneal endothelial cells show either differentiated or precursor cell characteristics. Cells Tissues Organs, **187**, 286–294 (2008).
DOI: 10.1159/000113406

[19] Kloceck P.: Handbook of infrared optical materials. Marcel Dekker, New York (1991).

[20] Harrick N. J.: Internal reflection spectroscopy. Wiley, New York (1975).

[21] Nitschke M., Götze T., Gramm S., Werner C.: Detachment of human endothelial cell sheets from thermo-responsive poly(NiPAAm-co-DEGMA) carriers. Express Polymer Letters, **1**, 660–666 (2007).
DOI: 10.3144/expresspolymlett.2007.90

[22] Schmaljohann D., Oswald J., Jørgensen B., Nitschke M., Beyerlein D., Werner C.: Thermo-responsive PNiPAAm-*g*-PEG films for controlled cell detachment. Biomacromolecules, **4**, 1733–1739 (2003).
DOI: 10.1021/bm034160p

[23] Hegewald J., Schmidt T., Eichhorn K-J., Kretschmer K., Kuckling D., Arndt K-F.: Electron beam irradiation of poly(vinyl methyl ether) films. 2. Temperature-dependent swelling behavior. Langmuir, **22**, 5152–5159 (2006).
DOI: 10.1021/la053461c

[24] Lin-Vien D., Colthub N. B., Fately W. G., Grasseli J. G.: The handbook of infrared and raman characteristic frequencies of organic molecules. Academic Press, London (1991).

eXPRESS Polymer Letters Vol.5, No.11 (2011) 977–995
Available online at www.expresspolymlett.com
DOI: 10.3144/expresspolymlett.2011.96

Preparation and characterization of nanocomposites based on COOH functionalized multi-walled carbon nanotubes and on poly(trimethylene terephthalate)

A. Szymczyk[1], Z. Roslaniec[2], M. Zenker[3], M. C. García-Gutiérrez[4], J. J. Hernández[4], D. R. Rueda[4], A. Nogales[4], T. A. Ezquerra[4]*

[1]Institute of Physics, West Pomeranian University of Technology, Piastów Av. 17,70-310 Szczecin, Poland
[2]Institute of Materials Science and Engineering, West Pomeranian University of Technology, Piastów Av. 17,70-310 Szczecin, Poland
[3]Department of Electrotechnology and Diagnostics, West Pomeranian University of Technology, Piastów Av. 17,70-310 Szczecin, Poland
[4]Instituto de Estructura de la Materia, CSIC, Serrano 119, 28006 Madrid, Spain

Received 11 March 2011; accepted in revised form 30 May 2011

Abstract. Poly(trimethylene terephthalate) nanocomposites containing COOH functionalized multi-walled nanotubes were synthesized with *in situ* polymerization method. The microstructure of the nanocomposites was studied by SEM, in terms of the dispersion state of the nanotubes and the polymer–nanotube interface. The thermal behaviour, mechanical properties and conductivity of these resultant PTT/MWCNTs nanocomposites were studied. The effect of the presence of MWCNTs on cold crystallization of PTT was monitored by dielectric spectroscopy. From thermal analysis study, it is found that the melting temperature and glass transition temperature are not significantly affected by the addition of MWCNTs. The crystallization temperature of PTT matrix is affected by the presence of CNTs. Nanocomposites have slightly higher degree of crystallinity than neat PTT and their thermo-oxidative stability is not significantly affected by the addition of MWCNTs. The study of the isothermal cold crystallization of amorphous PTT and its nanocomposites monitored by dielectric spectroscopy reveals that the presence of MWCNTs have influence on crystallization rate, especially at higher concentration (0.3 wt%). In comparison with neat PTT, the MWCNTs reinforced nanocomposites posses higher tensile strength and Young's modulus at low MWCNTs loading (0.05–0.3 wt%). In addition, all nanocomposites show reduction of brittleness as compared to the neat PTT. The electrical percolation threshold was found between 0.3 and 0.4 wt% loading of MWCNTs.

Keywords: *polymer nanocomposites, poly(trimethylene terephthalate), carbon nanotubes*

1. Introduction

Poly(trimethylene terephthalate) PTT is relatively recently commercialized polyester under trade names Corterra and bio-based Sorrona produced by Shell Chemicals and DuPont respectively [1–3]. PTT is produced by the polycondensation reaction of 1,3-propanediol (PDO) with terephthalic acid or dimethyl terephthalate. The main problem in commercialization of PTT was the high cost of PDO production, which was solved by Shell, which developed the low cost method of producing (petrochemical) PDO from ethylene oxide. At present the 1,3-propanediol used for the polymerization can be prepared either chemically or biologically. DuPont Tate & Lyle recently developed a biological process for the large-scale production of PDO using corn

*Corresponding author, e-mail: aszymczyk@zut.edu.pl

sugar as the raw material in place of petroleum [2–5]. DuPont's PTT Sorrona fibers are made from PDO derived from renewable corn sugar and fossil fuel derived terephthalic acid.

PTT is a semicrystalline polymer which combines the advantageous properties of polyesters and polyamides with main application field in textile industry. Many research groups [3, 6–8] have shown that the structure of PTT is very different from that of commercially well known aromatic linear polyesters poly(ethylene terephthalate) (PET) and poly (butylene terephthalate) (PBT), although their chemical composition is very similar. Owing to unusual properties such as excellent elastic recovery, high thermal and chemical resistance and dyeability, PTT is now a potential competitor of PBT and PET in textile, packing and engineering thermoplastic markets. Review of literature concerning recent advances in the field of PTT based copolymers [9–11], blends [12–14] and composites [15–17] shows a evident trend toward the development of such materials.

PTT is an important candidate for being compounded with various nanoparticles to further broaden its utility. Significant improvements in ultimate properties have been observed after incorporation of various types of nanoparticles into engineering polymers [18, 19]. In particular, carbon nanotubes (CNTs) due to their relatively high surface to volume and aspect ratios, extraordinary mechanical properties, low density and their superior thermal and electrical properties [20–22] are recognized as an ideal nanofiller material in structural and functional polymer composites. Introduction of small quantities of CNTs into a polymer matrix can lead to obtain structural composites with high elastic modulus, high tensile and compressive strength and stiffness. The mechanical properties combined with electrical, thermal, optical and many other properties have been extensively investigated by many research groups for wide range of applications [22–30].

In this work, poly(trimethylene terephthalate)/multi-walled carbon nanotubes nanocomposites were prepared by *in situ* polymerization method. The effect of carboxy-functionalized multi-walled nanotubes (MWCNTs) concentration on thermal, mechanical, and electric properties of the obtained composites was studied. Here we show that at low loading of MWCNTs it is possible to obtain electrical conductive PTT nanocomposites with improved mechanical properties, and the presence of carbon nanotubes have effect on cold crystallization rate of nanocomposites.

2. Experimental

2.1. Materials

Dimethyl terephthalate (DMT, Elana S.A., Torun, Poland), 1,3-propanenediol (PDO, Shell Chemicals Europe B.V., The Netherlands), anhydrous N-methyl-2-pyrrolidone (NMP, Sigma-Aldrich), COOH-functionalized multi-walled carbon nanotubes (MWCNTs, Nanocyl S. A., Belgium) with diameter ≅ 9.5 nm, length < 1.5 μm, and COOH functionalization < 4 wt%, were applied to prepare PTT nanocomposites. Purity of MWCNTs as received was > 97%. PDO was distilled before using. As catalyst the tetrabutyl orthotitanate ($Ti(OBu)_4$, Fluka), and as antioxidant the tetrakis(methylene(3,5-dit-butyl-4-hydroxyphenylhydro-cinnamate))methane (Irganox 1010, Ciba-Geigy, Basel, Switzerland) were used as received.

2.2. Preparation of PTT/MWCNTs nanocomposites

Nanocomposites containing 0.05, 0.1, 0.2, 0.3, 0.4 0.5 wt% of COOH functionalized MWCNTs were prepared by polycondensation in the molten state. The polymerizations were carried out in a 1L high pressure reactor (Autoclave Engineers Pennsylvania, USA) equipped with a vacuum pump, condenser, and cold trap for collecting the by-products. Before introduction to the reaction mixture the MWCNTs were dispersed in 300 ml of N-methyl-2-pyrrolidone (NMP) using ultra-high speed stirrer and then ultrasound (Homogenizator HD 2200, Sonopuls, Bandelin, Berlin, Germany). Completed time of dispersing was 30 min. During the last 10 min of dispersing time the PDO was introduced into MWCNTs dispersion in NMP. Then the dispersion was introduced into reactor containing melted DMT. The first step of polycondensation, the transesterification reaction, was carried out under a constant flow of nitrogen at 165°C in the presence of catalyst (0.15 wt%) for one and half hour. During the reaction, methanol was distilled off. The conversion of the transesterification reaction was calculated by monitoring the amount of effluent methanol. When the reaction was completed, the

thermal stabilizer Irganox 1010 (0.5 wt%) and the second portion of catalyst (0.1 wt%) were introduced to the reactor. Then the reaction temperature was increased slowly to 220°C and the pressure was reduced slowly. When the NMP was distilled off, the reaction temperature was increased to 260°C and pressure reduced below 25 Pa for the 2nd step of the polycondensation reaction. The stirring torque change was monitored in order to estimate the melt viscosity of the product. All syntheses were finished when melt reach the same value of viscosity at 260°C. The molten composite was extruded from reactor into water cooling bath, and then granulated and dried before processing. At the same conditions the neat PTT was synthesized as reference.

2.3. Sample preparation

Dumbbell shape samples of nanocomposites for tensile and DMTA tests were obtained by injection moulding at a pressure of around 50 MPa and at temperature 250°C, into a mould at temperature 40°C. Before tests samples were annealed at 80°C for 8 hours. Amorphous films of about 280 μm thickness for conductivity and dielectric properties studies were prepared by press moulding (Collin P 200E) at 245°C and 15 bar for 2 min and subsequently quenched (250°C/min). Subsequently, circular gold electrodes 2 cm in diameter were deposited onto the surface of the film sample.

2.4. Characterization methods

The limiting viscosity number (intrinsic viscosity) $[\eta]$ of PTT and PTT/MWCNTs nanocomposites was measured 30°C on Ubbelohde viscometer with capillary Ic (K = 0.03294) using a polymer solution of 0.5 g/dl in phenol/trichloroethylene (60/40 by weight). The limiting viscosity number is related to the molecular weight, M_v, through the Mark-Houwink equation (Equation (1)):

$$[\eta] = K \cdot M_v^{\alpha} \tag{1}$$

where K and α are constants specific to the solvent and temperature. The viscosity average molecular weight (M_v) of PTT and its nanocomposites was calculated by using constants: $K = 5.36 \cdot 10^{-4}$ dl/g and $\alpha = 0.69$ available in literature [31]. The measurements of $[\eta]$ were repeated for some samples, which have been earlier purified by means of the following procedure: PTT/MWCNTs (or PTT) was dissolved in phenol/trichloroethylene (60/40 w/w), then filtered to separate the CNTs. The sample was precipitated by adding methanol and recovered by filtration and again dissolved and re-precipitated twice. Finally, the precipitated solid was dried in vacuum at 60°C for 24 hours. The aim of this procedure was to eliminate the influence of MWCNTs presence on measured $[\eta]$ values.

The melt flow rate (MFR) of all the samples was determined using a melt flow tester (CEAST, Italy) according to ISO 1133 specification, under 21.18 N load, orifice diameter 2.095 mm and at temperature 230°C. The samples before measurements were dried in a vacuum dryer at 60°C for 24 hours.

The melt viscosity (η) of the nanocomposites were measured at 240°C on an ARES rheometer (Rheometric Scientific Inc.,USA) at frequency of 1 Hz during 10 min, in a parallel-plate fixture (d = 25 mm) with a gap distance of 2 mm.

The calorimetric measurements were carried out by means of a TA Instruments DSC Q-100 (New Castle, DE, USA). Indium was employed for the temperature and heat flow calibration. The heat capacity at each temperature was evaluated with respect to sapphire standard. Weighed (10±0.2 mg) and encapsulated in aluminum pans samples were heated from 20 to 250°C, and kept at 250°C for five minutes and cooled back down to –25 °C, and then measurements were taken over a temperature range of -25÷250°C at a heating rate of 10°C/min, and under nitrogen flow. The glass transition temperature (T_g) was taken as the midpoint of the change of heat capacity increment ($\Delta C_p/2$) associated with the glass-rubber transition. The specific heat increment ΔC_p associated with T_g of amorphous phase of semicrystalline PTT, was calculated from the vertical distance between two extrapolated baselines at the glass transition temperature according to the literature [32]. The nominal melting temperature (T_m) was defined as the of peak of the melting endotherm during heating from 25 to 250°C, and the nominal crystallization temperature (T_c) was defined as the peak of the crystallization exotherm upon cooling from 250 to –25°C. The heat of fusion (ΔH_m) and the heat of crystallization (ΔH_c) of the crystal phase were calculated from the area of the DSC endo- and exotherm, respectively. The degree of crystallinity, x_c, (i.e. the weight fraction crystallinity) was determined according to Equation (2) as the ratio of the

integrated heat of fusion ΔH_m value of the sample over the heat of fusion of fully crystalline PTT, i.e. $\Delta H_m^0 = 145.6$ J/g [3, 33]:

$$x_c[\,\%\,] = \frac{\Delta H_m}{\Delta H_m^0} \tag{2}$$

The thermogravimetric analysis (TGA) was carried out on a SETARAM TGA 92-16 apparatus. Samples (5±0.1 mg) were placed in alumina crucibles and heated from ambient to 700°C at heating rate of 10°C/min in a 20 ml/min flow of argon or dray air.

Dynamic mechanical thermal properties were measured by DMTA Mk-II apparatus (Polymer Laboratories, Church Stretton UK.) using the bending mode at a frequency of 1 Hz, and at a heating rate of 3°C/min from –100 to 250°C. The glass transition temperature was taken as the temperature at the maximum α-relaxation peak of the loss modulus E'' and tan δ curves [32].

The tensile tests were performed on an Instron 1112 tensile testing machine (Norwood, MA,USA) at room temperature. Tensile examinations were measured on dumbbell samples at a constant crosshead speed of 5 mm/min. Young's modulus, yield strength, stress and elongation at break, were calculated from the stress–strain curves on an average of twelve specimens for each kind of materials according to DIN 53455 standards.

The morphology of the fracture surface of composite samples was examined by a JEOL JSM-610 scanning electron microscope (SEM). Samples were fractured at liquid nitrogen and gold sputtered prior to observation.

Measurements of the complex permittivity $\varepsilon^* = \varepsilon' - i\varepsilon''$, where ε' represents the permittivity and ε'' the dielectric loss, of the nanocomposites were performed in the frequency range of 10^{-1} Hz$<f<10^7$ Hz, using a Novocontrol system (Hundsangen, Germany) integrating an ALPHA dielectric interface. Sputtered gold electrodes, 2 cm diameter, were employed to prepare a sandwich type capacitor. The temperature was controlled by means of a Novocontrol Quatro Cryosystem nitrogen gas jet, leading to isothermal conditions within an error of 0.1°C during every single sweep. The dielectric relaxations were empirical described in terms of the Havriliak-Negami (HN) Equation (3) [34]:

$$\varepsilon^*(\omega) - \varepsilon_\infty = \frac{\varepsilon_0 - \varepsilon_\infty}{[1 + (i\omega\tau_{HN})^b]^c} \tag{3}$$

where $\Delta\varepsilon = \varepsilon_0 - \varepsilon_\infty$ is the dielectric strength; ε_0, ε_∞ are the relaxed and unrelaxed dielectric constant value, respectively; $\omega = 2\pi f$ is the frequency; τ_{HN} is the central relaxation time; b and c are parameters that describe the shape of the relaxation time distribution function (symmetric and asymmetric broadening). Obtained values of $\varepsilon''(\omega)$ $\varepsilon'(\omega)$ were fitted to approximated with Equation (1). HN curve fits were performed using the WinFit v.2.9 software program from Novocontrol.

Alternating current (ac) electrical conductivity measured at room temperature was derived by $\sigma(\omega) = \varepsilon_0 2\pi f\varepsilon''$, where f and ε_0 are frequency and vacuum permittivity respectively.

3. Results and discussion

3.1. Dispersion of PTT/MWCNTs nanocomposites

Nanocomposites were prepared by using *in situ* polycondensation method. The control of the degree of dispersion of the nanotubes in a polymer matrix is difficult because of the strong intramolecular forces that exist between carbon nanotubes which are responsible for the formation of 10–50 nm nanotube bundles. These bundles are difficult to exfoliate since the nanotubes may be hundreds to thousands of nanometers long, disturbing the uniform dispersion of the nanotubes in a polymer matrix [24, 20]. In order to obtain a homogenous distribution of MWCNTs in the whole composite system, the CNTs were mechanically and sonically dispersed in solvent (NMP) and then introduced to the reaction mixture. The presence of dispersing solvent which was distilled off during the synthesis and the presence of COOH functionalized MWCNTs had a slight influence on the syntheses of PTT nanocomposites. In comparison to the net polymer the reaction of polymer chain growth monitored by increase of reactive mixture viscosity proceeded slower and the reaction time lasted about one hour. The highest content of CNTs achieved in the prepared nanocomposites was 0.5 weight%. The introduction of higher content of CNTs was not possible because, the melt does not flow.

In Table 1 the physical properties of obtained nanocomposites are listed. The average molecular weight ($\overline{M}_v$) of neat PTT and PTT in the nanocomposites determined from limiting viscosity number measurements is range from 44 000 to 37 000 g/mol. The

Table 1. Characteristic of PTT and PTT/MWCNTs nanocomposites

Sample	w_{CNT} [wt%]	[η] [dl/g]	$\overline{M}_v \cdot 10^4$ [g/mol]	MFR [g/10 min]	η Pa·s
PTT	0	0.82; 0.83[A]	4.2A	16.8	210
PTT/0.05	0.05	0.84	4.3	15.7	–
PTT/0.1	0.1	0.82; 0.82[A]	4.1[A]	16.1	330
PTT/0.2	0.2	0.78; 0.80[A]	4.0	15.9	372
PTT/0.3	0.3	0.78; 0.76[A]	3.7[A]	15.2	359
PTT/0.4	0.4	0.77	3.8	14.4	343
PTT/0.5	0.5	0.78; 0.76[A]	3.7[A]	13.7	342

w_{CNT} – weight fraction of MWCNTs; [η] – limiting viscosity number; $\overline{M}_v$ – viscosity average molecular weight determined from [η]; MFR – melt flow rate at 230°C; η – melt viscosity of polymer at 240°C and frequency of 1 Hz.

values of the melt flow rate of nanocomposites are lower than for neat PTT suggesting their higher melt viscosity. Measurements of the viscosity (η) of the nanocomposites determined on ARES-rheometer have confirmed that nanocomposites have higher viscosity 240°C than the neat PTT. Moreover, the increase in viscosity does not change appreciably with the CNTs content. Higher melt viscosity of nanocomposites in comparison to the neat PTT suggest the existence of interconnected or network structures formed as a result of CNT-CNT and CNT-polymer interactions. The COOH functional groups at the surface of MWCNTs can interact in the PTT/MWCNTs composite with ester groups of PTT molecules through hydrogen bonding. The presence of hydrogen bond interaction between functional groups of CNT and polyester molecules has been confirmed in PEN/CNTs composites [35].

3.2. Thermal stability

The mass loss (TG) and its derivative (DTG) curves of PTT and PTT/MWCNTs composites with different weight content of CNTs in argon and air atmosphere are shown in Figures 1a–d. The values of the

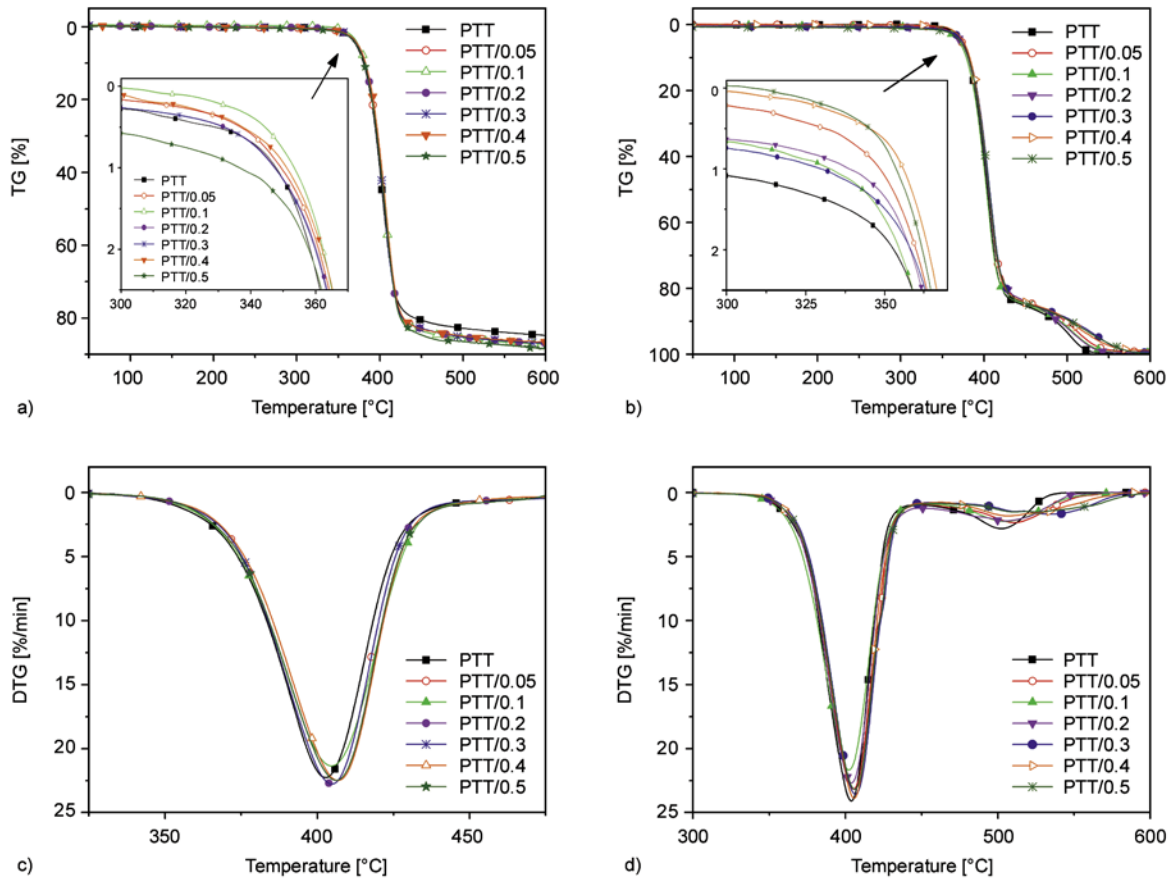

Figure 1. The mass loss (TG) and its derivative (DTG) curves as a function temperature for PTT nanocomposites in argon (a, c) and in air atmosphere (b, d)

Table 2. The characteristic temperatures of the decomposition of the PTT and PTT/MWCNTs nanocomposites in argon and air

	MWCNT content [wt%]						
	0	**0.05**	**0.1**	**0.2**	**0.3**	**0.4**	**0.5**
in argon							
$T_{2\%}$ [°C]	358	360	364	360	361	362	360
$T_{10\%}$ [°C]	383	384	384	384	384	385	384
T_{DTG} [°C]	405	405	405	407	405	407	406
in air							
$T_{2\%}$ [°C]	354	360	358	360	365	365	353
$T_{10\%}$ [°C]	382	382	379	381	383	383	382
T_{DTG1} [°C]	404	405	403	406	406	407	406
T_{DTG2} [°C]	503	511	506	530	538	540	528

$T_{2\%}$, $T_{10\%}$ – temperature of 2 and 10% weight loss respectively; T_{DTG} – temperature at the maximum weight loss rate

characteristic temperatures, including the temperature of 2 and 10% weight loss ($T_{2\%}$, $T_{10\%}$) and the temperature at the maximum weight loss rate (T_{DTG}) of neat PTT and MWCNTs-filled nanocomposites are presented in Table 2. It is evident that neat PTT and its nanocomposites exhibit one decomposition step in argon and two decomposition steps in air. The study of the thermal decomposition kinetics of PTT [36] have shown that the first step of the decomposition of PTT in both argon and air atmospheres is an overlapping of two decomposition processes. The first process is caused by degradation of the polymer chain implying an end group initiation mechanism affected by the molecular weight of PTT. The second degradation process is mainly caused by the thermal degradation of the products formed during the first decomposition process and it is not affected by the molecular weight (end groups) of PTT. Wang *et al*. [37] have shown that the first small weight-loss process (weight loss 2–4%) in argon is highly sensitive to molecular weight and the weight loss during this step decreased steadily with increasing molecular weight. These effect is a result of relatively poor thermal stability of hydroxyl terminal groups in PTT which initiate thermal degradation of PTT (especially ester groups). Additionally, Kelsey *et al*. [38] have shown that the predominant thermal degradation mechanism of PTT and other commercially important aromatic polyesters as PET and PBT is consistent with concerted, electrocyclic oxo retro-ene reaction [39–41], sometimes referred to as the McLafferty (ML) rearrangement. Hence, during thermal degradation of PTT one of the two ester groups between benzene rings forms hexatomic ring, and then after ML rearrangement some chain fragments with end-COO group and end-allyl ester group are formed, which are easy to decarboxylation and latter to de-esterification under high-temperature condition. In these processes products of thermal degradation of PTT, among others, CO_2, CO, acrylaldehyde and some fragments such as phenyl-containing chain were indentified [42].

Studies by Wang *et al*. [36] indicated a three overlapping weight-loss stages for the degradation of PTT in air. During the first process the PTT chains are degraded into smaller fragments by an initial end chain scission. These small fragments during the second processes are oxidized into volatile products. Decomposition of initially stable structures formed in first and second processes forming probably crosslinked residues take place during the third stage of the thermo-oxidative degradation of PTT. According to the Figures 1c–d, neat PTT and all the nanocomposites starts with a first main degradation stage in air at around 335°C independent of the content of MWCNTs. The weak second degradation step in the temperature range 450–600°C (Figure 1d) is due to the decomposition of some thermostable species formed during first degradation step. These may include decomposition of crosslinked carbonaceous structures and also carbon nanotubes. For nanocomposites, the temperature of the maximum weight loss rate (T_{DTG2}) at this post-major/second weight loss step is shifted to higher temperatures. The obtained results show that the thermal and oxidative stability of PTT is independent of the COOH functionalized MWCNT content. These results are in agreement in other researchers [43] observed for PET/CNT nanocomposites which have

confirmed also that functionalization of CNTs and concentration have no influence of thermal stability of polyester nanocomposites.

3.3. Microstructure of the PTT nanocomposites

Morphology of PTT nanocomposites containing short thin COOH functionalized MWCNTs was investigated by using SEM analysis. Figures 2a–d shows SEM micrographs of fracture surfaces of PTT nanocomposites with MWCNTs. As mentioned above, CNTs often tend to bundle together by van der Waals interaction between the individual nanotubes with high aspect ratio and large surface area and lead to some agglomerations, which prevent efficient load transfer to nanotube. Moreover, most of the nanotubes show pulling out and sliding at the surface of nanocomposite, suggesting a limitation of load transfer [44–45]. SEM analysis of the fracture surfaces of PTT/MWCNTs nanocomposites indicate rather homogenous distribution of carbon nanotubes in the PTT matrix. Individual nanotubes, some entanglements or bundles of CNTs, apparently pulled out from the matrix during fracturing are observed on the surface.

3.4. Effect of MWCNTs addition on the thermal transition of PTT

Carbon nanotube functionalization inducing interactions between polymeric matrix and carbon nanotubes can cause changes in the crystallization and melting behavior of the semicrystalline polymer. In many polymer systems after introduction of carbon nanotubes the increase in crystallization temperature, enhancing in nucleation density and in some causes reduction of crystallization time was observed [35, 43, 46–50]. The effect of the presence of COOH functionalized MWCNT in PTT matrix on the melting and crystallization processes was studied by DSC. Table 3 summarizes data obtained from heating and cooling DSC scans for PTT and PTT/MWCNTs nanocomposites which are presented on Figure 3. PTT/MWCNTs nanocomposites exhibit a negligible decrease (1–2°C) in the glass transition compared to pure PTT. Nanocomposites with different amount of MWCNTs have very slightly lower values of ΔC_p at T_g than neat PTT. Introduction of CNTs can separates the long polymer chain into shorter cooperatively rearranging (CRR) segments [51]. The shift of T_g toward lower temperatures can be a result of the higher mobility of these shorter CRR

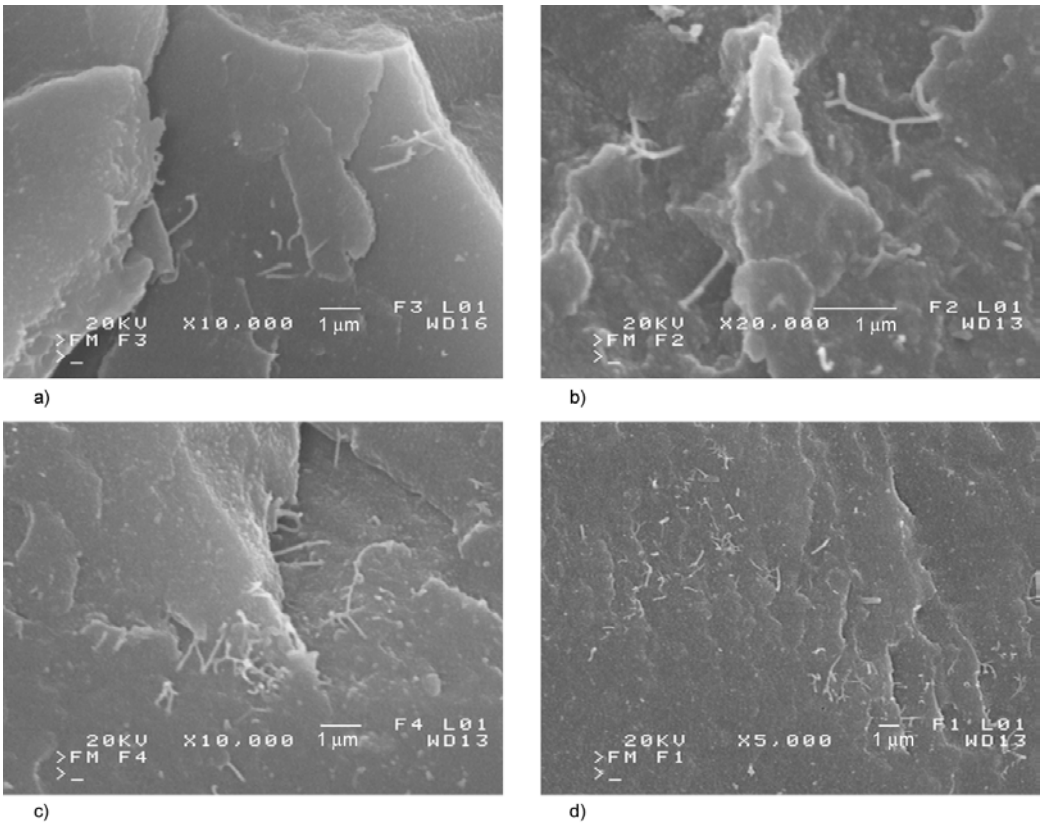

Figure 2. SEM images of cryofractured PTT nanocomposites with 0.3 wt% (a–b) and 0.5 wt% (c–d) of MWCNTs

Table 3. Thermal properties of PTT and PTT/MWCNTs nanocomposites

Sample	T_g [°C]	ΔC_p [J/(g·°C)]	T_m [°C]	ΔH_m [J/g]	$T_{c,on}$ [°C]	T_c [°C]	ΔH_c [J/g]	ΔT [°C]	x_c [%]
PTT	52	0.18	229	50.7	180	170	50.3	59	34.8
PTT/0.05	50	0.15	229	53.7	186	168	53.7	61	36.9
PTT/0.1	51	0.16	229	54.4	186	166	53.5	63	37.4
PTT/0.2	50	0.16	229	54.1	190	166	54.0	63	37.1
PTT/0.3	51	0.16	230	54.3	186	167	54.4	63	37.2
PTT/0.4	51	0.15	230	53.9	187	168	53.5	62	37.0
PTT/0.5	51	0.16	230	54.2	186	168	53.7	62	37.2

T_g – glass transition temperature; T_m, ΔH_m – temperature and enthalpy of melting respectively; ΔC_p – change of heat capacity; $T_{c,on}$ – onset temperature of crystallization; T_c, ΔH_c – temperature and enthalpy of crystallization respectively; x_c – degree of crystallinity of the sample; $\Delta T = T_m - T_c$ – degree of supercooling

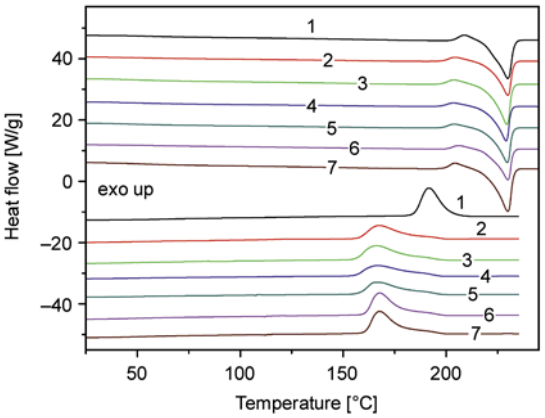

Figure 3. DSC heating and cooling curves for PTT nanocomposites; where:
1 – PTT, 2 – PTT/0.05, 3 – PTT/0.1, 4 – PTT/0.2, 5 – PTT/0.3, 6 – PTT/0.4, 7 – PTT/0.5

segments. Recently, for semicrystalline polymers such PTT, PET, PEEK [51–53], a three phase model consisting of crystalline, mobile amorphous phase (MAP) and rigid amorphous phase (RAP) was used to describe the structural formation of PTT at various conditions. The RAP exists at the interface of crystal and amorphous phase as a result of the immobilization of a polymer chain due to the crystal. In semicrystalline nanocomposites, the RAP fraction sometimes exists at the surface of nanofillers in the polymer nanocomposites material. Ma and Cebe [53] have used these model in to explain lowering the T_g and decreasing degree of crystallinity with the CNTs loading for PTT/MWCNTs (with aspect ratio 36) fibers prepared by electrospinning. They have established that addition of CNTs results in increase in the RAP, which indicates an enhancement in the constrains on the polymer chains in PTT composites nanofibers due to the decrease of chain mobility. Here, the melting temperature and degree of crystallinity of the PTT/MWCNTs nanocomposites (Table 3) are not significantly affected by the presence on the MWCNTs. The degree of crystallinity of nanocomposites increase very slightly around 2–2.6%. Nanocomposites have wider crystallization peak than those of neat PTT, indicating the heterogenous nucleation effect of the CNTs for the PTT matrix. In PTT/MWCNTs nanocomposites, the onset crystallization temperature ($T_{c,on}$) increase by about 6–10°C, whereas the crystallization peak temperature (T_c) decreases by about 2–4°C. Usually the lower degree of supercooling reflects higher nucleation and crystallization rates. The PTT/MWCNTs nanocomposites have a little higher degree of supercooling (ΔT = 61–63°C, Table 3) with the introduction of the MWCNTs in comparison with pure PTT (ΔT = 59°C). Crystallization of polymer occurs from the alignment of mobile polymer chains. The addition of filler in polymer composites changes the thermal properties of the materials due to the formation of interfacial connections between the filler surfaces and polymer. The connections, which may be physical adsorption or chemical bonding, or a combination of both, restrict the mobility of the polymer chains. Here, the introduced short and thin MWCNTs into PTT matrix are not effective nucleating agent caused the increase of the degree of supercooling. These can be a result of their low aspect ratio or their strong interactions with PTT chains. The topological confinement of macromolecular chains at their interfaces and strong interactions between them can increase of supercooling. Recent study on crystallization behaviour of nanocomposites based on high density polyethylene and CNTs performed by Müller and coworkers [54, 55] have shown that in nanocomposites a competition between super-nucleation and confinement occur. At low contents the nucleation effect dominates. The confinement increases as the nano-filler

content increases. In consequence of confinement the reduction of both crystallization and melting temperatures, a strong reduction of the crystallinity degree, an increase in the supercooling needed for isothermal crystallization and a depression of the overall crystallization rate were observed.

The effect of the presence of MWCNT on non-isothermal crystallization behavior of PTT nanocomposites observed here, is in contrast to the results reported in literature for aromatic polyester/CNT nanocomposites. For example, poly(ethylene 2,6-naphthalate) (PEN) nanocomposites [35, 47] have shown the increase in the crystallization temperature of PEN by incorporating pristine MWCNTs and COOH functionalized MWCNTs. Moreover, PEN nanocomposites have a lower degree of supercooling for crystallization with the introduction of the MWCNTs. This behavior has suggested that nanotubes act as effective nucleating agents in the PEN matrix, resulting in the enhancement of the crystallization of the PEN nanocomposites. The increase in the crystallization temperature and degree of crystallinity was observed for poly(butylene terephthalate) nanocomposites containing of 0.2 wt% of pristine MWCNTs and NH_2 functionalized MWCNTs [44] and for poly(ethylene terephthalate) (PET) nanocomposites containing acid treated MWCNTs [43, 48–49]. Correlation of spectroscopic measurements with DSC have shown that acid treated MWCNTs present in PET nanocomposites not only enhanced crystallinity but also lead to a much better polymer crystalline order [49]. The presence of MWCNTs in PET matrix transforms trans conformers of the noncrystalline phase into crystalline domains with the nanotubes acting as moderate nucleation agents. Xu *et al*. [50] have studied the crystallization behaviour of PTT/MWCNTs nanocomposites, which were prepared by solution blending. They report that for such PTT nanocomposites the melting temperature and crystallinity were not affected by the presence on the MWCNTs. However, an increase of crystallization temperature and a decrease of the degree of supercooling was observed with increasing nanotube concentration. Comparison of the results obtained for PTT nanocomposites prepared by solvent blending [50] and those studied here for PTT nanocomposites prepared by *in situ* polymerization seems to indicate that the preparation method in addition to the type of carbon nanotube can affect the crystallization behavior of PTT.

3.5. Effect of MWCNTs on cold crystallization of PTT nanocomposites

In situ real time dielectric isothermal crystallization of amorphous PTT and PTT/MWCNTs nanocomposites at 50°C was monitored by dielectric spectroscopy. Figure 4 shows dielectric loss ε'' and dielectric permittivity ε' at different crystallization times (t_c) of amorphous neat PTT (a–b) and PTT nanocomposites containing 0.05 wt% (c–d) and 0.3 wt% (e–f) of MWCNTs. The obtained spectra recorded in each sweep (4 min) are representative of an isostructure at a given stage of crystallization because the time scale for a sweep is short in comparison with time scale for crystallization. The initial dielectric spectrum for amorphous neat PTT and PTT nanocomposites shows the typical α-relaxation associated with the segmental motions of the amorphous chains above the glass transition. Regarding the analysis of the dynamics of the amorphous phase during isothermal crystallization, the segmental motions of the amorphous polymer chains are confined between the crystalline regions thus modifying the main α-relaxation. It was established for many polymers, that the occurrence of crystallinity in a polymer affects the segmental dynamics, as characterized by DS, in the following way: i) a decrease of the dielectric strength, ii) a shift of the relaxation rate to lower values and iii) a considerable broadening of the relation function [34, 55–58]. The dielectric strength of a relaxation process is, in a first approach, proportional to the total amount of relaxing units participating in the process. The decrease of the dielectric strength (reduction of the relaxing material) is caused by crystal formation due to the progressive transfer of the amorphous material to the growing crystalline phase [34, 56–58]. For neat PTT and PTT/MWCNTs nanocomposites it is observed a decrease in the intensity of the α-relaxation process, characterized by the value of the dielectric loss at the maximum (ε''_{max}) and a positional shift of the maximum of the α-relaxation towards lower frequencies with increasing crystallization time in agreement with previous results [55–58]. Figure 5 represents the variation of ε''_{max} and f_{max} with crystallization time. Analysis of the changes of ε''_{max} and f_{max} indicates that the presence

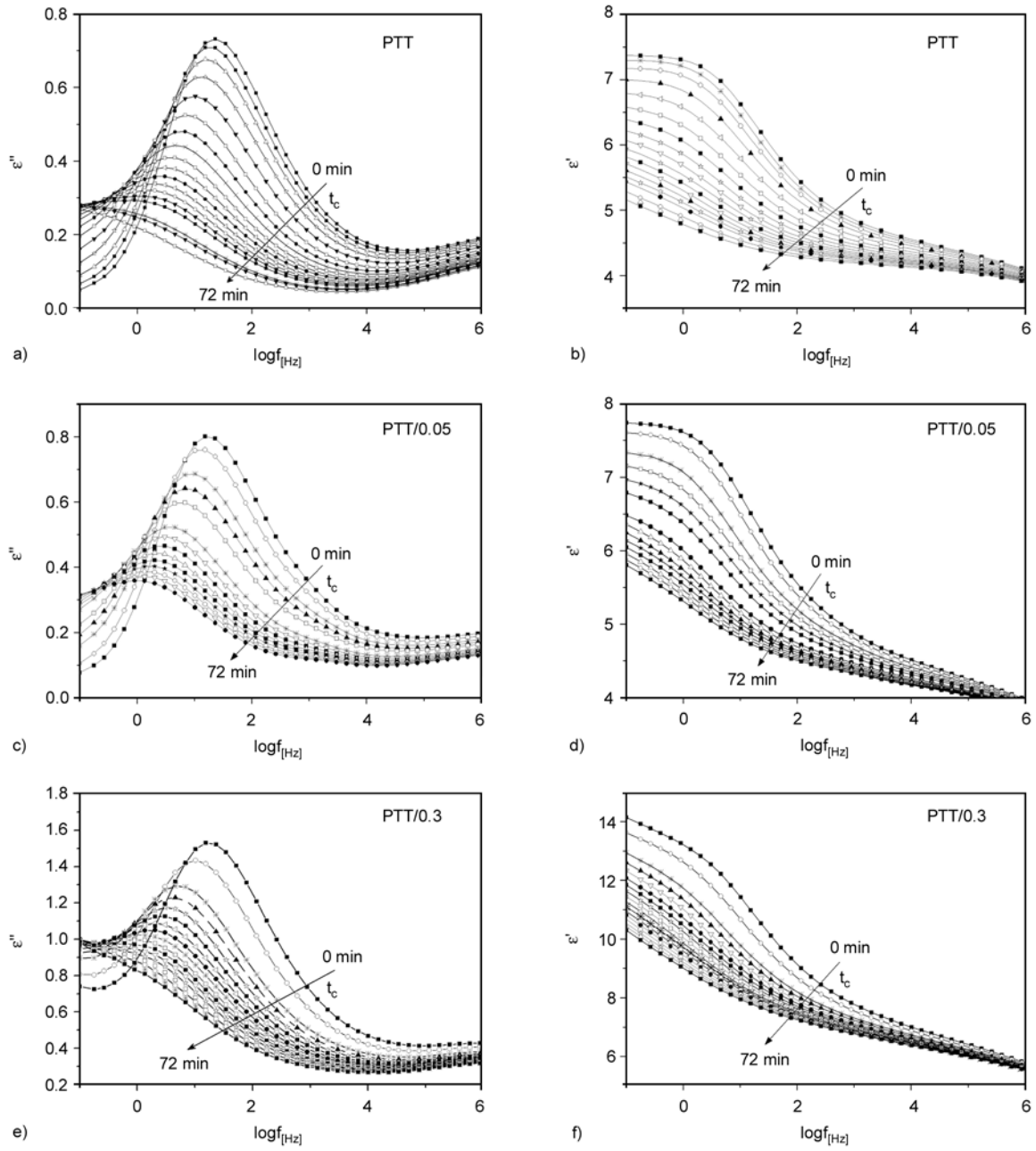

Figure 4. Real time evolution of the dielectric loss (a, c, e) and the dielectric constant (b, d, f) during isothermal crystallization at 50°C as a function of frequency at different crystallization times

of MWCNTs has an effect on cold crystallization of PTT, especially at higher content of MWCNTs (0.3 wt%). As crystallization time increases, for nanocomposite containing 0.3 wt% of MWCNTs the faster shift of fmax in the direction of low frequencies and a higher decrease in the intensity of ε''_{max} than for PTT and PTT with 0.05 wt% of MWCNTs was observed. The changes of the values of the dielectric parameters: $\Delta\varepsilon$, τ_{HN}, b, c obtained after fitting the Equation (1) are presented in Figure 6 as a function of crystallization time. After t_c = 40 min a 92, 74 and 82% reduction of the dielectric strength (Figure 6a) for PTT/0.3 and PTT/0.05 and neat PTT, respectively was observed. These results indicate that PTT/0.3 nanocomposite crystallizes faster than PTT and PTT/0.05 nanocomposite. PTT and its nanocomposites show a slight increase of the relaxation time τ_{HN} values (calculated by Equation (1), Figure 6b). For neat PTT, the relaxation time τ_{HN} of the α process tends to be slower with crystallization time in a linear fashion with time during the whole crystallization period. The same

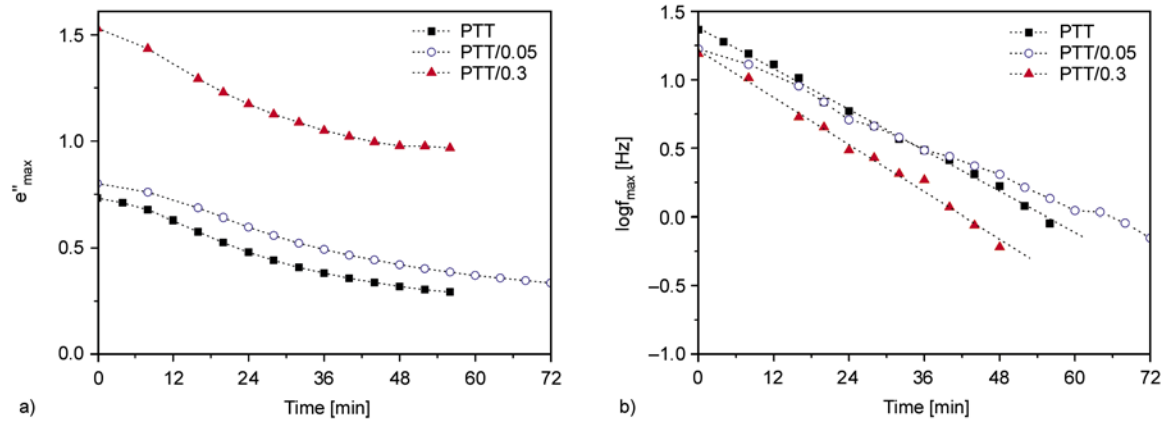

Figure 5. Variation of the maximum dielectric loss values ε''_{max} (a) and frequency of the maximum loss f_{max} (b) as a function of crystallization time at 50°C. (Doted lines are to guide the eyes).

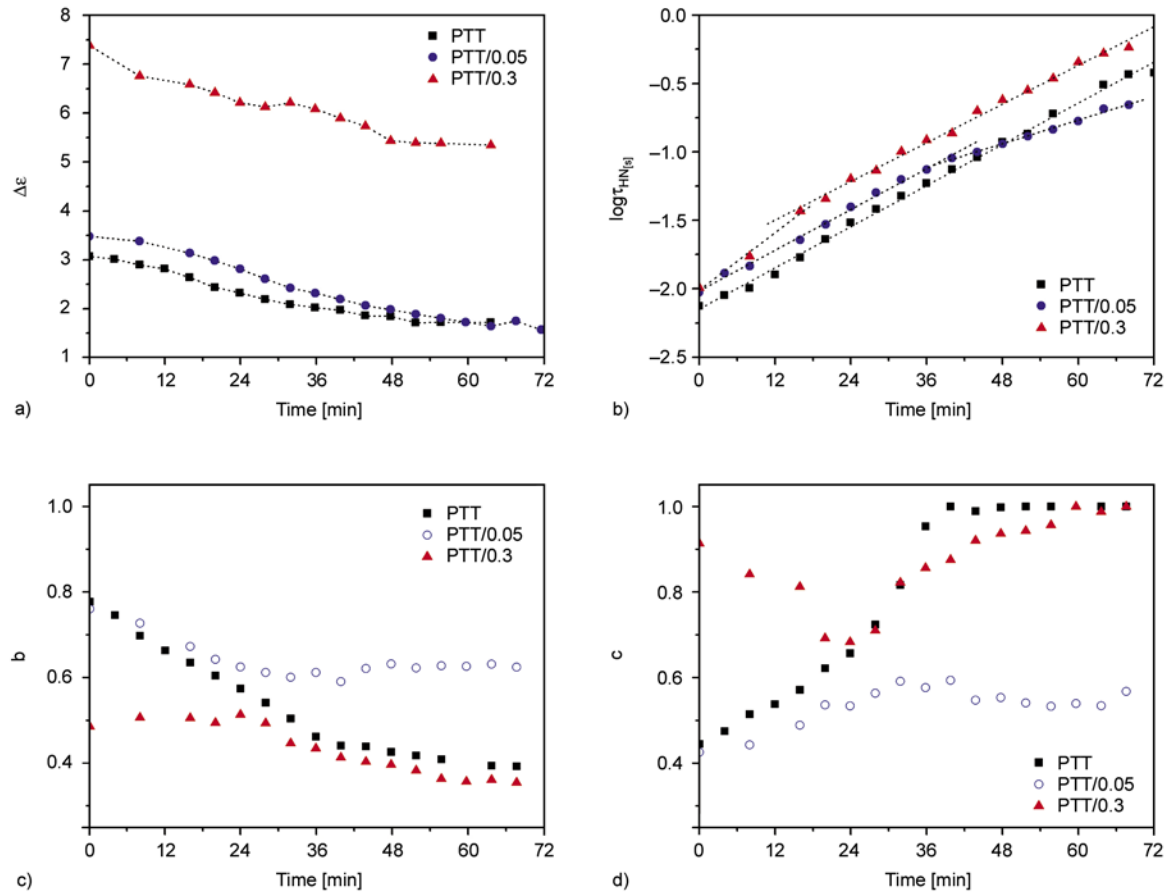

Figure 6. Real time evolution of the HN parameters: $\Delta\varepsilon$ (a), τ_{HN} (b), b (c), c (d) during isothermal crystallization processes of net PTT and PTT/MWCNTs nanocomposites at 50°C. (Doted lines are to guide the eyes).

behaviour of relaxation time was detected for cold crystallization of PTT by A. Sanz *et al*. [58]. This effect is a result of the restricted mobility by crystals. As crystallization time increase, the segmental dynamics in the amorphous phase slows down due to an increase of the crystalline phase. PTT nanocomposites containing: 0.3 and 0.05 wt% of MWCNTs shows higher initial ($t_c = 0$) values of their relaxation times than that of unfilled PTT. This effect could be due to a restricted mobility of the polymer chains at the polymer/nanofiller interface where the interactions between PTT chains and CNTs surface can play role. Obviously, this interaction is not present for unfilled PTT. As shown in Figure 6b–c, a continuous change of *b* and *c* shape parameters with crystallinity is observed. For neat

PTT, the increase of the *c* parameter towards the highest possible value of $c = 1$ after $t_c = 40$ min indicates a decrease of the asymmetry of the relaxation upon crystallization. For PTT nanocomposite with 0.05 wt% at the beginning of crystallization time ($t_c < 32$ min) an increase of the value of c parameter is found. Then, independent on the crystallization time, remains constant ($c \approx 0.5$–0.6). Also a gradual increase with crystallization time of the c parameter is observed for PTT with 0.3 wt% of MWCNTs. During crystallization of neat PTT, a decrease of the *b* parameter (Figure 6b) with crystallization time is found. This indicates that the relaxation curve become broader. Broader curves, higher *b* values, are observed for PTT nanocomposites around 0.5 and 0.8 for PTT/0.05 and PTT/0.05 nanocomposites respectively, and then his decrease with crystallization time is observed. This study of the isothermal cold crystallization of amorphous PTT and its nanocomposites reveals that the presence of MWCNTs have influence on crystallization rate, especially at higher concentration (0.3 wt%) of CNTs.

3.6. Dynamic mechanical thermal analysis

The storage and loss modulus and the loss factor tan δ, determined by DMTA measurements for the pure PTT matrix and nanocomposites filled with MWCNTs, are plotted versus the temperature in Figures 7a, 7b and 7c respectively. It can be seen that magnitudes of the storage modulus and location of the loss peak change significantly for nanocomposites. The addition of MWCNTs to PTT matrix show an influence of the nanotube content on the storage modulus in the glassy region and also in some samples in the rubbery region above the glass transition. For convenience of comparison, data of E' modulus at 25°C are presented in Table 4. All nanocomposites have higher values of E' modulus compared to pure PTT. The highest increase by about of 55% of E' modulus at 25°C was observed for the sample containing 0.3 wt% of MWCNTs. These changes of the E' modulus can be attributed to cohesive interactions between the large surface area of nanotubes and PTT [59]. On loss modulus E'' and tan δ curves (Figure 7b–c), the two relaxation peaks β and α are observed. The β-relaxation peak at about –75°C is attributed to the reorientation of the hydroxyl groups and the local motions of the carboxyl groups in the

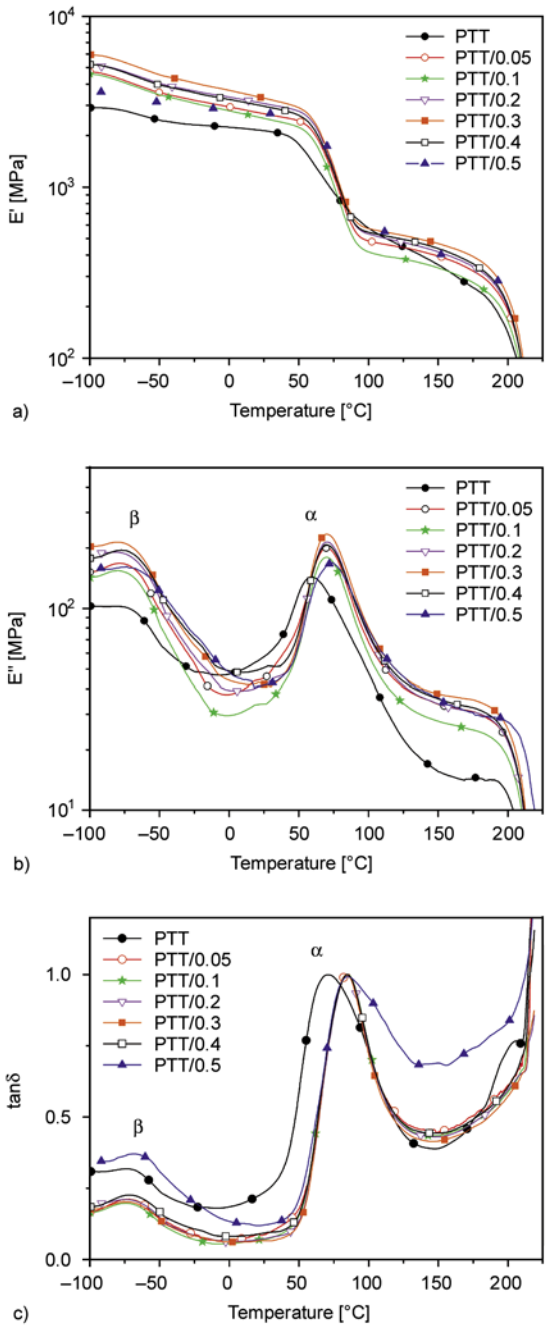

Figure 7. The storage and loss modulus and normalized tan δ as a function of temperature for PTT and PTT/MWCNTs nanocomposites

amorphous phase. The α-relaxation peak corresponds to the glass transition of amorphous PTT. Usually for semicrystalline polymers the increasing of the Tα and decreasing intensity of of α-relaxation peak is observed with the increase of crystallinity. Tan δ is sensitive to all molecular movements occurring in polymer. For nanocomposites, the molecular movement at the interface contribute to the value of the tan δ that enables to estimate the bonding

Table 4. DMTA properties of PTT and PTT/MWCNTs nanocomposites

Sample	E′ at 25°C [MPa]	T_α (E″) [°C]	T_α (tan δ) [°C]
PTT	2136	59	70
PTT/0.05	2683	70	85
PTT/0.1	2524	70	85
PTT/0.2	3081	70	85
PTT/0.3	3316	70	84
PTT/0.4	2971	70	85
PTT/0.5	2716	70	84

E′ – storage modulus at 25°C and 1 Hz; T_α – temperature of α-relaxation corresponding the glass transition determined from maximum of loss modulus (*E″*) and tan *δ*

Table 5. Tensile properties and brittleness of PTT/MWCNTs nanocomposites

Sample	E [GPa]	σ_b [MPa]	ε_b [%]	B [10^{10}·(%·Pa)]
PTT	2.10±0.03	69.1±2.6	4.3±0.3	1.089
PTT/0.05	2.20±0.04	70.5±2.2	4.4±0.5	0.847
PTT/0.1	2.21±0.05	72.4±2.9	4.6±0.6	0.861
PTT/0.2	2.22±0.04	73.4±2.7	4.2±0.5	0.773
PTT/0.3	2.25±0.04	74.5±1.5	4.7±0.4	0.641
PTT/0.4	2.25±0.03	69.2±2.9	4.2±0.5	0.801
PTT/0.5	2.24±0.05	69.7±3.3	4.4±0.4	0.836

E – tensile modulus; σ_b – stress at break; ε_b – elongation at break; *B* (=1/(ε_b·*E′*)) – brittleness [61]

between the interphase of the matrix and the CNTs. The normalized tan *δ* peak of nanocomposites (except 0.5 wt%) was narrower than for neat PTT, which can be indicative of changes in the molecular dynamics for the polymer nanocomposites. Independent on the MWCNTs content, the T_α is shifted on tan *δ* curves from 70°C for the neat PTT to 85°C for PTT/ MWCNTs nanocomposites. This can be due to reduction of the mobility of the PTT chains around the nanotubes by interfacial interactions between CNTs and polymer matrix. The values of T_g determined form the peak maximum of tan *δ* or *E″* curves are found to be higher than from DSC data because of the different frequency of perturbation involved in their measurements and sample preparation. Samples studied by DMTA were prepared by injection molding and then annealed at 80°C. As the MWCNTs content increases, the increase of the intensity of β-relaxation peak is observed for nanocomposites. As mentioned above this peak is associated with the motions of the short chin-segments of PTT and is cooperatively related to the glass transition, the increase of these peak associated with this transition can be regarded as evidence for partial activation of PTT chains by the COOH functionalized MWCNTs.

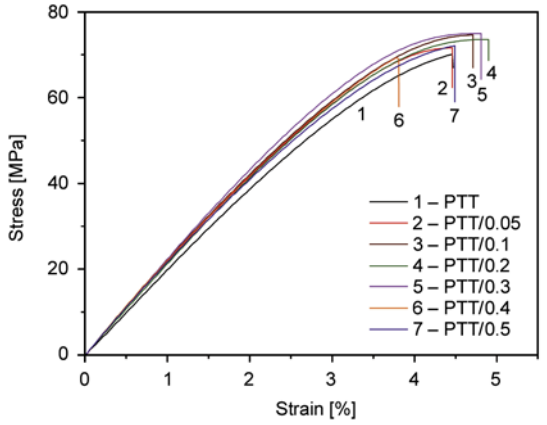

Figure 8. Representative stress strain curves of nanocomposites

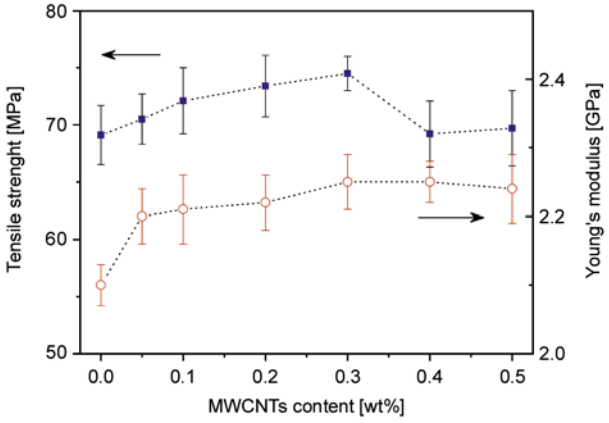

Figure 9. Stress at break and Young's modulus of nanocomposites as a function of MWCNTs weight fraction

3.7. Mechanical properties of nanocomposites

The tensile properties of the synthesized PTT/MWCNTs nanocomposites are listed in Table 5 and representative stress-strain curves are shown in Figure 8. The variation of tensile strength and tensile modulus of the nanocomposites are shown in Figure 9. As the content of the MWCNTs increase to 0.3 wt%, the nanocomposites tensile strength and Young's modulus increases. However, further addition of MWCNTs (0.4–0.5 wt%) lowers tensile strength and Young's modulus, but their values are still comparable or higher (modulus) to neat PTT. The values of elongation at break are higher or comparable to the neat PTT. SEM analysis (Figure 2) have shown that the CNTs are well distributed in the polymer matrix for all concentrations, note that the increase of CNT content does not lead

to formation of visible agglomerates (except small entangled CNTs structures) in the bulk volume of the polymer. When two immiscible phases such PTT and MWCNTs meet, the interaction between them occurs at their interfaces. At the interface, the net internal force of each phase is not zero and will lead to the appearance of a tension called interfacial tension. Interfacial tension is somewhat similar to surface tension in that cohesive forces are also involved [60]. However, the main forces involved in interfacial tension are adhesive forces, i.e., tension between phases. The interphase in PTT nanocomposites is influenced by the Van der Waals forces between MWCNTs and PTT matrix. Additional effect can rise from the interactions of the COOH functional groups at the surface of MWCNTs with ester groups of PTT molecules (hydrogen bonds) and from the interactions between the graphene rings of the MWCNTs and benzene rings of terephthalate moiety. The increase of the tensile strength can be attributed to strong interphase interaction between the matrix and the CNTs. The lower values of tensile strength of nanocomposites compared with neat PTT could be explained by the lower molecular weight (Table 1) of PTT. The molecular weight strongly affects the cohesion of polymer. It was mentioned earlier, that the syntheses of PTT/MWCNTs nanocomposites was carried out to the define viscosity of the reaction mixture at established temperature, which was controlled by the stirrer torque. The presence of CNTs strongly influence on the melt viscosity of polymer and hence the molecular weight of polymer in composites (0.3–0.5 wt%) have lower values of molecular weight compared with neat PTT. Brittleness of the nanocomposites was calculated by Equation (4) [61]:

$$B = \frac{1}{\varepsilon_b \cdot E'} \tag{4}$$

where ε_b is the tensile elongation at break an E' is the storage modulus determined at 1 Hz and 25°C by DMTA. It can be seen (Table 5) that addition of CNTs reduces the brittleness of the nanocomposites. Brittleness of nanocomposites shows opposite tendency to the tensile strength, i.e. brittleness was found to decrease with the CNTs loading until 0.3 wt%, while at CNTs loading above 0.3 wt% increase.

In recent years, many studies with different focuses on mechanical properties of polymer/CNTs composites have been published. Due to the extraordinary mechanical properties, high aspect ratio and low density, the outstanding potential of CNTs as reinforcements in many polymer composites is evident. For example, the mechanical properties improvement was observed for the polyacronitrile/CNTs [62] composite fibers containing single wall carbon nanotubes (SWCNTs), double wall carbon nanotubes (DWNCTs) and multiwall carbon nanotubes (MWCNTs). The low-strain properties (modulus and thermal shrinkage) were most improved by SWNT, while the high-strain properties were most improved by MWCNTs. Gao *et al*. [63] have studied the nylon 6/CNTs composites fibers, which were prepared by *in situ* ring-opening polymerization of caprolactam in the presence of carboxylated SWNTS. These composites containing 1 wt% of SWCNTs show a 153% increase in Young's modulus and 103% increase in tensile strength. Reinforcement effects were also observed by adding of CNTs in polystyrene [64], epoxy resin [65], poly (ethylene oxide) [66]. Nevertheless, for many polymer/CNTs nanocomposites a critical CNTs content in the matrix could be found when the CNT reinforcement effect on randomly oriented polymer/CNTs composites was studied. Below this content, the reinforcement effect for polymer/CNTs composites increases with increasing CNT content. Above this content, the strength of the polymer/CNTs composites decreases, and in some cases, even lower than that of the polymer matrix. For example, the epoxy/CNT [67] and polypropylene/CNT [68] composites shows the critical CNTs content at about 0.5 wt%. At higher CNTs content, the extent of improvement in mechanical properties might be limited by the high viscosity of the composite and by poor load transfer between CNTs and polymer matrix resulted from imperfect dispersion and not completely covered some surface of the CNTs by polymer matrix due to the large specific area of CNTs. As will be noted in many reports, most of randomly oriented polymer/CNTs composites show only a moderate or no strength enhancement, especially for composites containing untreated CNTs, mainly attributed to poor load transfer between polymer matrix and CNTs.

3.8. Electrical properties

When electrically conducting particles such as carbon nanotubes are randomly distributed within an insulating polymer matrix, the sample is non-conducting, before a critical volume fraction of the conducting phase is reached. This critical value is known as the percolation threshold. In addition, close to the percolation threshold, the electrical properties show a nonlinear (critical) behaviour characterized by small variations in the physical parameters, such as temperature, composition or voltage, result in large variations of electrical properties [69].The percolation threshold for the electrical conductivity in polymer/CNTs nanocomposites shows the complex dependence on a variety of factors, including nanotube characteristics (aspect ratio, single- or multi-wall), and fabrication/processing conditions, which affect the filler's distribution and orientation and the filler-matrix interactions [70].

Figures 10 and 11 show the alternating current conductivity, at room temperature, as a function of frequency and the conductivity measured at 0.1 Hz respectively, for PTT nanocomposites with different MWCNTs content. At loadings below 0.26 vol%, the PTT nanocomposites exhibit a strong frequency dependence of the conductivity, which is typical for insulating materials. At loadings in excess of 0.20 vol% (percolation threshold), the composites exhibited a conductive behaviour which is nearly independent of frequency.

The critical concentration of MWCNTs dispersed in PTT matrix can be estimated on the concept of excluded volume for a system of randomly oriented, nanotubes as capped cylinders by using Equation (5) [71]:

$$\varphi_c = 1 - \exp\left[-\frac{V_{ex}\left(\frac{\pi}{4}D^2L + \frac{\pi}{6}D^3\right)}{\frac{4\pi}{3}D^3 + 2\pi D^2L + \frac{\pi}{2}DL^2} \right] \quad (5)$$

where V_{ex} (= 1.4) is total excluded volumes for continuum, randomly infinitely thin rods. The nanotubes were modeled as capped cylinders of radius $r = D/2$ and length L, in the limit of very high aspect ratio ($r/L << 1$) [71]. The critical volume percentage of nanotubes was predicted to be 0.434 vol%, which is about one half higher than of the experimental value (0.262 vol%). This results indicate that conductive pathways due to the content between adjacent nanotube are formed at lower content of nanotubes than was predicted. It can be also a result of well-dispersion of short-thin MWCNTs in PTT matrix, because the presence of aggregates usually increase the conductivity percolation threshold.

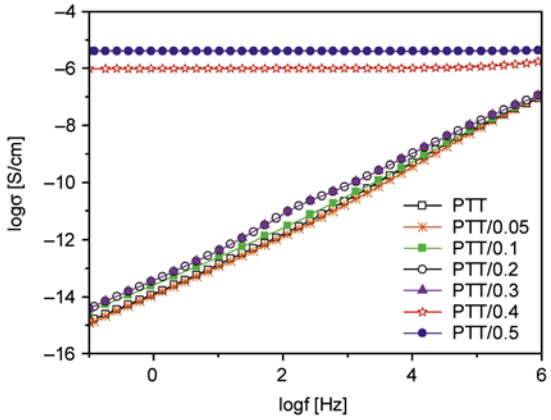

Figure 10. Frequency dependence of ac conductivity at room temperature of PTT/MWCNTs nanocomposites with different MWCNTs content

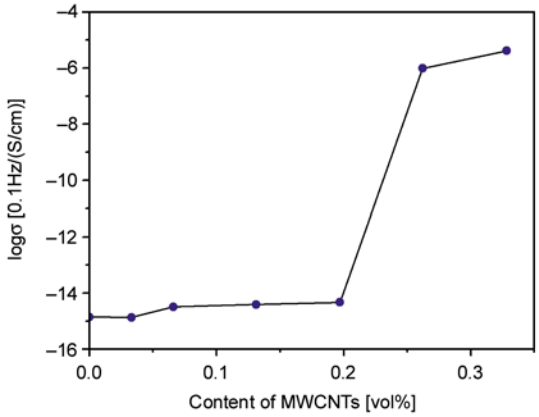

Figure 11. Electrical conductivity of PTT/MWCNTs nanocomposites at frequency of 0.1 Hz and at room temperature as a function of MWCNTs volume fraction

4. Conclusions

In situ polycondensation of PDO and dimethyl terephthalate in the presence of carboxylated MWCNTs (with aspect ratio around 158) was carried to obtain the PTT/MWCNTs nanocomposites. The poly (timetylene terephthalates) (PTT), with average molecular weight in range $4.3–3.7 \cdot 10^4$ g/mol were obtained. The melting and glass transition temperatures of nanocomposites obtained by non-isothermal crystallization (DSC results) were not significantly affected by the presence of CNTs. Nanocomposites have slightly higher degree of crystallinity

than pure PTT. The study of the isothermal cold crystallization of amorphous PTT and its nanocomposites monitored by dielectric spectroscopy reveals that the presence of MWCNTs have influence on crystallization rate, especially at higher concentration (0.3 wt%). Dynamic mechanical analysis studies revealed an enhancement of the storage modulus, in the glassy state, up to 55% at an CNTs loading of 0.3 wt%, and for nanocomposites the increase the glass transition temperature about 10–15°C. With increasing of MWCNTs loading from 0.05 to 0.3 wt%, the increase of tensile strength and Young's modulus of nanocomposites was found. All nanocomposites show reduction of brittleness in comparison to as compared to the neat PTT. The electrical percolation threshold was found at an loading between 0.3 and 0.4 wt% of MWCNTs.

Acknowledgements

The authors thank for the financial support from the Polish Ministry of Science and High Education in the framework of a grant no DFG/83/2006 and from the MCYT (grant MAT2009- 07789), Spain.

References

[1] Liu H., Xu Y., Zheng Z., Liu D.: 1,3-Propanediol and its copolymers: Research, development and industrialization. Biotechnology Journal, **5**, 1137–1148 (2010). DOI: 10.1002/biot.201000140

[2] Kurian J. V.: A new polymer platform for the future – Sorona® from corn derived 1,3-propanediol. Journal of Polymers and the Environment, **13**, 159–167 (2005). DOI: 10.1007/s10924-005-2947-7

[3] Chuah H. H.: Synthesis, properties and applications of poly(trimethylene terephthalate). in 'Modern polyester: Chemistry and technology of polyesters and copolyesters' (eds.: Scheirs J., Long T. E.) Wiley, Chichester, 361–397 (2004). DOI: 10.1002/0470090685.ch11

[4] Patel M. K., Crank M.: Projections for the production of bulk volume bio-based polymers in Europe and environmental implications. Journal of Biobased Materials and Bioenergy, **1**, 437–453 (2007). DOI: 10.1166/jbmb.2007.020

[5] Wolfson W.: Spinning corncobs into socks farming plastics with 'green' chemistry. Chemistry and Biology, **13**, 109–111 (2006).

[6] Frisk S., Ikeda R. M., Chase D. B., Kennedy A., Rabolt J. F.: Structural analysis of poly(trimethylene terephthalate) fibers and films using polarized raman spectroscopy. Macromolecules, **37**, 6027–6036 (2004). DOI: 10.1021/ma049234j

[7] Desborough I. J., Hall I. H., Neisser J. Z.: The structure of poly(trimethylene terephthalate). Polymer, **20**, 545–552 (1979). DOI: 10.1016/0032-3861(79)90163-0

[8] Ho R-M., Ke K-Z., Chen M.: Crystal structure and banded spherulite of poly(trimethylene terephthalate). Macromolecules, **33**, 7529–7537 (2000). DOI: 10.1021/ma000210w

[9] Shyr T-W., Lo C-M., Ye S-R.: Sequence distribution and crystal structure of poly(ethylene/trimethylene terephthalate) copolyesters. Polymer, **46**, 5284–5298 (2005). DOI: 10.1016/j.polymer.2005.04.030

[10] Szymczyk A., Senderek E., Nastalczyk J., Roslaniec Z.: New multiblock poly(ether-ester)s based on poly (trimethylene terephthalate) as rigid segments. European Polymer Journal, **44**, 436–443 (2008). DOI: 10.1016/j.eurpolymj.2007.11.005

[11] Szymczyk A.: Structure and properties of new polyester elastomers composed of poly(trimethylene terephthalate) and poly(ethylene oxide). European Polymer Journal, **45**, 2653–2664 (2009). DOI: 10.1016/j.eurpolymj.2009.05.032

[12] Krutphun P., Supaphol P.: Thermal and crystallization characteristics of poly(trimethylene terephthalate)/poly(ethylene naphthalate) blends. European Polymer Journal, **41**, 1561–1568 (2005). DOI: 10.1016/j.eurpolymj.2005.01.023

[13] Huang J-M.: Polymer blends of poly(trimethylene terephthalate) and polystyrene compatibilized by styrene-glycidyl methacrylate copolymers. Journal of Applied Polymer Science, **88**, 2247–2252 (2003). DOI: 10.1002/app.11945

[14] Lee L-T., Woo E-M.: Miscible blends of poly(4-vinyl phenol)/poly (trimethylene terephthalate). Polymer International, **53**, 1813–1820 (2004). DOI: 10.1002/pi.1588

[15] Liu Z., Chen K., Yan D.: Crystallization, morphology, and dynamic mechanical properties of poly(trimethylene terephthalate)/clay nanocomposites. European Polymer Journal, **39**, 2359–2366 (2003). DOI: 10.1016/S0014-3057(03)00166-6

[16] Mishra J. K., Chang Y-W., Choi N. S.: Preparation and characterization of rubber-toughened poly(trimethylene terephthalate)/organoclay nanocomposite. Polymer Engineering and Science, **47**, 863–870 (2007). DOI: 10.1002/pen.20770

[17] Xu Y., Jia H-B., Piao J-N., Ye S-R., Huang J.: Crystallization behavior of poly(trimethylene terephthalate)/multi-walled carbon nanotube composites. Journal of Materials Science, **43**, 417–421 (2008). DOI: 10.1007/s10853-007-2161-1

[18] Paul D. R., Robeson L. M.: Polymer nanotechnology: Nanocomposites. Polymer, **49**, 3187–3204 (2008). DOI: 10.1016/j.polymer.2008.04.017

[19] Coleman J. N., Khan U., Gun'ko Y. K.: Mechanical reinforcement of polymers using carbon nanotubes. Advanced Materials, **18**, 689–706 (2006). DOI: 10.1002/adma.200501851

[20] Jorio A., Dresselhaus G., Dresselhaus M. S.: Carbon nanotubes: Advanced topics in the synthesis, structure, properties and applications. Springer, Berlin (2008).

[21] Yu M-F., Lourie O., Dyer M. J., Moloni K., Kelly T. F., Ruoff R. S.: Strength and breaking mechanism of multiwalled carbon nanotubes under tensile load. Science, **287**, 637–640 (2000). DOI: 10.1126/science.287.5453.637

[22] Szleifer I., Yerushalmi-Rozen R.: Polymers and carbon nanotubes – Dimensionality, interactions and nanotechnology. Polymer, **46**, 7803–7818 (2005). DOI: 10.1016/j.polymer.2005.05.104

[23] Lau A. K-T., Hui D.: The revolutionary creation of new advanced materials – Carbon nanotube composites. Composites Part B: Engineering, **33**, 263–277 (2002). DOI: 10.1016/S1359-8368(02)00012-4

[24] Moniruzzaman M., Winey K. I.: Polymer nanocomposites containing carbon nanotubes. Macromolecules, **39**, 5194–5205 (2006). DOI: 10.1021/ma060733p

[25] Eitan A., Fisher F. T., Andrews R., Brinson L. C., Schadler L. S.: Reinforcement mechanisms in MWCNT-filled polycarbonate. Composites Science and Technology, **66**, 1162–1173 (2006). DOI: 10.1016/j.compscitech.2005.10.004

[26] García-Gutiérez M. C., Hernández J. J., Nogales A., Panine P., Rueda D. R., Ezquerra T. A.: Influence of shear on the templated crystallization of poly(butylene terephthalate)/single wall carbon nanotube nanocomposites. Macromolecules, **41**, 844–851 (2008). DOI: 10.1021/ma0713512

[27] Nogales A., Broza G., Roslaniec Z., Schulte K., Šics I., Hsiao B. S., Sanz A., García-Gutiérez M. C., Rueda D. R., Domingo C., Ezquerra T. A.: Low percolation threshold in nanocomposites based on oxidized single wall carbon nanotubes and poly(butylene terephthalate). Macromolecules, **37**, 7669–7672 (2004). DOI: 10.1021/ma049440r

[28] Giraldo L. F., Brostow W., Devaux E., López B. L., Pérez L. D.: Scratch and wear resistance of polyamide 6 reinforced with multiwall carbon nanotubes. Journal of Nanoscience and Nanotechnology, **8**, 3176–3183 (2008). DOI: 10.1166/jnn.2008.092

[29] Giraldo L. F., López B. L., Brostow W.: Effect of the type of carbon nanotubes on tribological properties of polyamide 6. Polymer Engineering Science, **49**, 896–902 (2009). DOI: 10.1002/pen.21386

[30] Glenis S., Likodimos V., Guskos N., Yarmis D., Zolnierkiewicz G., Szymczyk A., Lin C. L.: Magnetic properties of carbon nanotube poly(ether-ester) nanocomposites. Journal of Applied Physics, **108**, 054314/1–054314/4 (2010). DOI: 10.1063/1.3481688

[31] Chuah H. H., Lin-Vien D., Soni U.: Poly(trimethylene terephthalate) molecular weight and Mark–Houwink equation. Polymer, **42**, 7137–7139 (2001). DOI: 10.1016/S0032-3861(01)00043-X

[32] Brostow W.: Performance of plastics. Hanser, Munich (2001).

[33] Pyda M., Boller A., Grebowicz J., Chuah H., Lebedev B. V., Wunderlich B.: Heat capacity of poly(trimethylene terephthalate). Journal of Polymer Science Part B: Polymer Physics, **36**, 2499–2511 (1998). DOI: 10.1002/(SICI)1099-0488(199810)36:14<2499::AID-POLB4>3.0.CO;2-O

[34] Kremer F., Schönhals A.: Broadband dielectric spectroscopy. Springer, Berlin (2000).

[35] Kim J. Y., Han S. I., Hong S.: Effect of modified carbon nanotube on the properties of aromatic polyester nanocomposites. Polymer, **49**, 3335–3345 (2008). DOI: 10.1016/j.polymer.2008.05.024

[36] Wang X-S., Li X-G., Yan D.: Thermal decomposition kinetics of poly(trimethylene terephthalate). Polymer Degradation and Stability, **69**, 361–372 (2000). DOI: 10.1016/S0141-3910(00)00083-5

[37] Wang X-S., Li X-G., Yan D.: High-resolution thermogravimetric analysis of poly(trimethylene terephthalate) with different molecular weights. Polymer Testing, **20**, 491–502 (2001). DOI: 10.1016/S0142-9418(00)00064-7

[38] Kelsey D. R., Kiibler K. S., Tutunjian P. N.: Thermal stability of poly(trimethylene terephthalate). Polymer, **46**, 8937–8946 (2005). DOI: 10.1016/j.polymer.2005.07.015

[39] McNeill I. C., Bounekhel M.: Thermal degradation studies of terephthalate polyesters: 1. Poly(alkylene terephthalates). Polymer Degradation and Stability, **34**, 187–204 (1991). DOI: 10.1016/0141-3910(91)90119-C

[40] McLafferty F. W.: Mass spectrometric analysis. Molecular rearrangements. Analytical Chemisry, **31**, 82–87 (1959). DOI: 10.1021/ac60145a015

[41] Botelho G., Queirós A., Liberal S., Gijsman P.: Studies on thermal and thermo-oxidative degradation of poly (ethylene terephthalate) and poly(butylene terephthalate). Polymer Degradation and Stability, **74**, 39–48 (2001). DOI: 10.1016/S0141-3910(01)00088-X

[42] Liu J., Bian S. G., Xiao M., Wang S. J., Meng Y. Z.: Thermal degradation and isothermal crystalline behavior of poly(trimethylene terephthalate). Chinese Chemical Letters, **20**, 487–491 (2009).
DOI: 10.1016/j.cclet.2008.11.035

[43] Yoo H. J., Jung Y. C., Cho J. W.: Effect of interaction between poly(ethylene terephthalate) and carbon nanotubes on the morphology and properties of their nanocomposites. Journal of Polymer Science Part B: Polymer Physics, **46**, 900–910 (2008).
DOI: 10.1002/polb.21424

[44] Kwiatkowska M., Broza G., Schulte K., Roslaniec Z.: The in-situ synthesis of poly(butylene terephthalate)/carbon nanotubes composites. Reviews on Advanced Materials Science, **12**, 154–159 (2006).

[45] Broza G.: Thermoplastic elastomers with multi-walled carbon nanotubes: Influence of dispersion methods on morphology. Composites Science and Technology, **70**, 1006–1010 (2010).
DOI: 10.1016/j.compscitech.2010.02.021

[46] Lu K., Grossiord N., Koning C. E., Miltner H. E., Van Mele B., Loos J.: Carbon nanotube/isotactic polypropylene composites prepared by latex technology: Morphology analysis of CNT-induced nucleation. Macromolecules, **41**, 8081–8085 (2008).
DOI: 10.1021/ma8008299

[47] Kim J. Y., Han S. I., Kim D. K., Kim S. H.: Mechanical reinforcement and crystallization behavior of poly (ethylene 2,6-naphthalate) nanocomposites induced by modified carbon nanotube. Composites Part A: Applied Science and Manufacturing, **40**, 45–53 (2009).
DOI: 10.1016/j.compositesa.2008.10.002

[48] Wang Y., Deng J., Wang K., Zhang Q., Fu Q.: Morphology, crystallization, and mechanical properties of poly(ethylene terephthalate)/multiwall carbon nanotube nanocomposites via *in situ* polymerization with very low content of multiwall carbon nanotubes. Journal of Applied Polymer Science, **104**, 3695–3701 (2007).
DOI: 10.1002/app.25677

[49] Tzavalas S., Drakonakis V., Mouzakis D. E., Fischer D., Gregoriou V. G.: Effect of carboxy-functionalized multiwall nanotubes (MWNT−COOH) on the crystallization and chain conformations of poly(ethylene terephthalate) PET in PET−MWNT nanocomposites. Macromolecules, **39**, 9150–9156 (2006).
DOI: 10.1021/ma0613584

[50] Xu Y., Jia H-B., Piao J-N., Ye S-R., Huang J.: Crystallization behavior of poly(trimethylene terephthalate)/multi-walled carbon nanotube composites. Journal of Materials Science, **43**, 417–421 (2008).
DOI: 10.1007/s10853-007-2161-1

[51] Hong P-D., Chuang W-T., Yeh W-J., Lin T-L.: Effect of rigid amorphous phase on glass transition behavior of poly(trimethylene terephthalate). Polymer, **43**, 6879–6886 (2002).
DOI: 10.1016/S0032-3861(02)00617-1

[52] Wundrelich B.: Reversible crystallization and the rigid–amorphous phase in semicrystalline macromolecules. Progress in Polymer Science, **28**, 383–450 (2003).
DOI: 10.1016/S0079-6700(02)00085-0

[53] Ma Q., Cebe P.: Phase structure of electrospun poly (trimethylene terephthalate) composite nanofibers containing carbon nanotubes. Journal of Thermal Analysis and Calorimetry, **102**, 425–434 (2010).
DOI: 10.1007/s10973-010-0977-4

[54] Müller A. J., Arnal M. L., Trujillo M., Lorenzo A. T.: Super-nucleation in nanocomposites and confinement effects on the crystallizable components within block copolymers, miktoarm star copolymers and nanocomposites. European Polymer Journal, **47**, 614–629 (2011).
DOI: 10.1016/j.eurpolymj.2010.09.027

[55] Trujillo M., Arnal M. L., Müller A. J., Bredeau S., Bonduel D., Dubois P., Hamley I. W., Castelletto V.: Thermal fractionation and isothermal crystallization of polyethylene nanocomposites prepared by in situ polymerization. Macromolecules, **41**, 2087–2095 (2008).
DOI: 10.1021/ma702272e

[56] Napolitano S., Wübbenhorst M.: Deviation from bulk behaviour in the cold crystallization kinetics of ultra-thin films of poly(3-hydroxybutyrate). Journal of Physics: Condensed Matter, **19**, 205121/1–205121/9 (2007).
DOI: 10.1088/0953-8984/19/20/205121

[57] Šics I., Ezquerra T. A., Nogales A., Denchev Z., Alvarez C., Funari S. S.: Cold crystallization of poly (ethylene naphthalene-2,6-dicarboxylate) by simultaneous measurements of X-ray scattering and dielectric spectroscopy. Polymer, **44**, 1045–1049 (2003).
DOI: 10.1016/S0032-3861(02)00742-5

[58] Nogales A., Ezquerra T. A., Denchev Z., Šics I., Baltá-Calleja F. J., Hsiao B. S.: Molecular dynamics and microstructure development during cold crystallization in poly(ether-ether-ketone) as revealed by real time dielectric and X-ray methods. Journal of Chemical Physics, **115**, 3804–3813 (2001).
DOI: 10.1063/1.1388627

[59] Sanz A., Nogales A., Ezquerra A. T., Soccio M., Munari A., Lotti N.: Cold crystallization of poly (trimethylene terephthalate) as revealed by simultaneous WAXS, SAXS, and dielectric spectroscopy. Macromolecules, **43**, 617–679 (2010).
DOI: 10.1021/ma902188c

[60] Kopczynska A., Ehrenstein G. W.: Polymeric surfaces and their true surface tension in solids and melts. Journal of Materials Education, **29**, 325–340 (2007).

[61] Brostow W., Hagg Lobland H. E., Narkis M.: Sliding wear, viscoelasticity, and brittleness of polymers. Journal of Materials Research, **21**, 2422–2428 (2006).
DOI: 10.1557/jmr.2006.0300

[62] Chae H. G., Liu J., Kumar S.: Carbon nanotubes-enabled materials. in 'Carbon nanotubes properties and applications' (ed.: O'Connell M. J.) CRC Press Taylor and Francis Group, Boca Raton, 213–253 (2006).

[63] Gao J., Zhao B., Itkis M. E., Bekyarova E., Hu H., Kranak V., Yu A., Haddon R. C.: Chemical engineering of the single-walled carbon nanotube−nylon 6 interface. Journal of the American Chemical Society, **128**, 7492–7496 (2006).
DOI: 10.1021/ja057484p

[64] Qian D., Dickey E. C., Andrews R., Rantell T.: Load transfer and deformation mechanisms in carbon nanotube-polystyrene composites. Applied Physics Letters, **76**, 2868–2870 (2000).
DOI: 10.1063/1.126500

[65] Allaoui A., Bai S., Cheng H. M., Bai J. B.: Mechanical and electrical properties of a MWNT/epoxy composite. Composites Science and Technology, **62**, 1993–1998 (2002).
DOI: 10.1016/S0266-3538(02)00129-X

[66] Geng H. Z., Rosen R., Zheng B., Shimoda H., Fleming L., Liu J., Zhou O.: Fabrication and properties of composites of poly(ethylene oxide) and functionalized carbon nanotubes. Advanced Materials, **14**, 1387–1390 (2002).
DOI: 10.1002/1521-4095(20021002)14:19<1387::AID-ADMA1387>3.0.CO;2-Q

[67] Bai J. B., Allaoui A.: Effect of the length and the aggregate size of MWNTs on the improvement efficiency of the mechanical and electrical properties of nanocomposites – Experimental investigation. Composites Part A: Applied Science and Manufacturing, **34**, 689–694 (2003).
DOI: 10.1016/S1359-835X(03)00140-4

[68] Koval'chuk A. A., Shchegolikhin A. N., Shevchenko V. G., Nedorezova P. M., Klyamkina A. N., Alsdyshev A. M.. Synthesis and properties of polypropylene/multiwall carbon nanotube composites. Macromolecules, **41**, 3149–3156 (2008).
DOI: 10.1021/ma800297e

[69] Foulger S. H.: Electrical properties of composites in the vicinity of the percolation threshold. Journal of Applied Polymer Science, **72**, 1573–1582 (1999).
DOI: 10.1002/(SICI)1097-4628(19990620)72:12<1573::AID-APP10>3.0.CO;2-6

[70] Kalaitzidou K., Fukushima H., Drzal L. T.: A route for polymer nanocomposites with engineered electrical conductivity and percolation threshold. Materials, **3**, 1089–1103 (2010).
DOI: 10.3390/ma3021089

[71] Celzard A., McRae E., Deleuze C., Dufort M., Furdin G., Marêché J. F.: Critical concentration in percolating systems containing a high-aspect-ratio filler. Physical Review, **53**, 6209–6214 (1996).
DOI: 10.1103/PhysRevB.53.6209

eXPRESS Polymer Letters Vol.5, No.11 (2011) 996–1008
Available online at www.expresspolymlett.com
DOI: 10.3144/expresspolymlett.2011.97

ROS-inducing potential, influence of different porogens and *in vitro* degradation of poly (D,L-lactide-co-glycolide)-based material

M. Stevanović[1*], *V. Pavlović*[2], *J. Petković*[3], *M. Filipič*[3], *D. Uskoković*[1]

[1]Institute of Technical Sciences of the Serbian Academy of Sciences and Arts, Knez Mihailova 35/IV, Belgrade 11000, Serbia
[2]Faculty of Agriculture, University of Belgrade, Nemanjina 6, Belgrade 11080, Serbia
[3]Department of Genetic Toxicology and Cancer Biology, National Institute of Biology, Vecna pot 111, Ljubljana 1000, Slovenia

Received 18 March 2011; accepted in revised form 2 June 2011

Abstract. Porous, poly(D,L-lactide-co-glycolide) (PLGA) materials were prepared by physicochemical solvent/non-solvent method with polyvinyl pyrrolidone (PVP) as a stabilizer and with silicone oil, paraffin, hydrogen peroxide or sodium chloride as a porogen. The obtained PLGA particles without porogens are non-agglomerated, uniform and with particle size on the submicron scale. The formation of intracellular reactive oxygen species (ROS) was measured spectrophotometrically using a fluorescent probe, 2,7-dichlorofluorescein diacetate (DCFH-DA) and it is shown that PLGA nanospheres are not inducers of intracellular formation. Porous PLGA scaffolds obtained in the experiment with sodium chloride as porogen and water as solvent of the porogen had apparently uniform pore morphology with spheroidal pore in shape and well controlled three-dimensional interconnected network. PLGA scaffolds are highly porous with similar porosity values. The degradation of PLGA nanoparticles and PLGA porous materials were studied in phosphate buffered saline as a degradation medium. The samples were characterized by Infrared Spectroscopy (IR), X-ray difractometry, Zeta potential measurements, Scanning Electron Microscopy (SEM) and Ultraviolet Spectroscopy (UV).

Keywords: *biodegradable polymers, ROS formation, porogens, zeta potential, in vitro degradation*

1. Introduction

A variety of materials have been used for replacement and repair of damaged or traumatized tissues [1–8].These materials include metals, ceramics, polymers (natural and synthetic) and their combinations. Polymers have great design flexibility because their composition and structure can be tailored to the specific needs [9, 10]. They are therefore attractive candidates for various clinical applications. Synthetic biodegradable polymers, poly (esters) based on polylactide (PLA), polyglycolide (PGA), polycaprolactone (PCL) and their copolymers are approved by the World Health Organization (WHO) and Food and Drug Administration (FDA) as materials that can be used in medicine and pharmacy [11–14]. Poly (DL-lactide-co-glycolide) (PLGA), a biocompatible and biodegradable copolymer of PLA and PGA, is widely used in various medical applications; controlled release of delivering drugs, scaffolds in the tissue engineering, fixation of bone fractures, chirurgical strings, etc. [15–17]. PLGA particles are used for the controlled delivery of several types of medicaments, including anticancer agents, antihypertensive agents, immunomodulatory drugs, hormones, vitamins, etc. [18–20].

*Corresponding author, e-mail: magdalena.stevanovic@itn.sanu.ac.rs

Scaffold provides temporary support for cell proliferation and differentiated function, allowing neotissue formation and initial remodeling [19]. The choice of the best scaffold for a particular tissue engineering application and how to change an existing scaffold to improve its performance are important components of any tissue engineering research project [19]. Numerous techniques have been used for scaffold design, such as solvent casting/particulate leaching, phase separation, microsphere sintering, electrospining, emulsion freeze drying, fiber extrusion, gas foaming and 3-D printing [19–21].

Many factors are important when designing materials for use in biomedicine. The main advantage of nano and microspheres used in tissue engineering, compared to the more traditional macroporous block scaffolds, is that nano and microspheres possess not only better drug-delivery properties, but also the ability to fill the bone defects with irregular and complex shapes and sizes [22]. The interstitial space between the particles of the microspheres is crucial for effective and functional bone regeneration [22–24] as they allow for both bone and vascular ingrowths. Appropriate porosity is a crucial biomaterial design criterion for materials used in tissue engineering applications as it can allow increased cell adhesion, migration, proliferation and extracellular matrix production within the scaffold at a tissue defect site [25].

In controlled drug delivery porosity is also a very important factor influencing the degradation process of poly(DL-lactide-co-glycolide). The presence of pores does not only increase the mobility of the involved species (drug molecules, acids and bases), but fundamentally alters the underlying drug release mechanisms. Generally, the release of medicament during the degradation process will be faster in case of porous particles. A factor related to the sphere porosity is, also, the initial burst effect, which corresponds to the rapid initial release of drug and is normally followed by the relatively controlled linear release [26].

The goal of the study reported here was to investigate the influence of different porogens on the morphological characteristics and formation of pores in PLGA based materials, nano and microspheres obtained by physicochemical solvent/non-solvent method, and also very important to eliminate the release-delayed phenomenon of macromolecular drug delivery system at the early stage of the degradation. Porous, PLGA materials were prepared with polyvinyl pyrrolidone (PVP) as a stabilizer and with silicone oil, paraffin, hydrogen peroxide or sodium chloride as a porogen. PVP acting as stabilizer and dispersant i.e. has role to prevent coalescence or aggregation of the particles. In the process of the preparation of the porous PLGA, we have obtained non-particulate templates in the forms of porous films and scaffolds. Using the synthesis protocol nanoparticulate PLGA materials were obtained only in the absence of porogens [27]. Since the recent studies have pointed out that the higher toxic potential of nanomaterials in comparison to their larger counterparts is most probably due to oxidative stress as a consequence of increased production of reactive oxygen species (ROS) [28, 29], it is very important to establish ROS-inducing potential of our model nanomaterial, PLGA nanospheres, which is determined in this paper.

2. Experimental

2.1. Materials

Poly(DL-lactide-co-glycolide) (PLGA) was purchased from Durect, Lactel (Birmingham, Alabama, USA) and had a lactide-to-glycolide ratio of 50:50. Molecular weight of the polymer is 40 000–50 000 g/mol. The time for its complete resorption in the body is 4 to 8 weeks. Polyvinyl pyrrolidone (povidone, PVP) was obtained from Merck Chemicals Ltd (k-25, Merck, Germany). Silicon oil, sodium chloride, hydrogen peroxide (all from Centrohem, Serbia) and paraffin (melting point 53–57ºC, Merck, Germany) were used as porogens. Cyclohexane (boiling point 81°C, Merck, Germany), n-heptane (Centrohem, Serbia) and distilled water were used as solvents of a porogens.

The degradation medium used was phosphate buffered saline (PBS, one tablet dissolved in 200 ml of deionized water yields 0.137 mol/l sodium chloride, 0.01 mol/l phosphate buffer and 0.0027 mol/l potassium chloride, pH is 7.4 at 25°C, Sigma-Aldrich, St. Louis, USA) with sodium azide (Sigma-Aldrich Chemie GmbH Germany), 0.1 mol/l solution NaN_3).

Chemicals for determining intracellular reactive oxygen species formation (DCFH-DA assay) [30], Minimal Essential Medium Eagle, penicillin/streptomycin, L-glutamine, phosphate buffered saline,

trypsin, foetal bovine serum, non-essential amino acid solution (100×), and 2,7-dichlorofluorescein diacetate (DCFH-DA) were obtained from Sigma Aldrich (St. Louis, USA).

2.2. Preparation of PLGA nanospheres and preparation of porous PLGA samples by different porogens and different solvents of the porogens

PLGA nano and microparticles were synthesized following method previously described in our work [31] i.e. by using physicochemical method with solvent/nonsolvent systems where obtained solutions were centrifuged. Polyvinyl pyrrolidone was used as a stabilizer of the particles.

Briefly, commercial granules poly(D,L-lactide-co-glycolide) (250 mg) have been dissolved in the acetone (20 ml) and, after approximately two hours, ethanol (25 ml) has been added into the solvent mixture. PLGA was precipitated by the addition of ethanol and the solution became whitish. The polymeric solution thus obtained has been very slowly poured into aqueous PVP solution (0.05% w/w) while continuously stirring at 1200 rpm by a stirrer. After that porogen (silicon oil, paraffin, hydrogen peroxide or sodium chloride) has been added into the mixture and then the solution has been centrifuged at 6000 rpm and at 5ºC for 120 min (Universal 320R, Hettich, Germany) and decanted. In all experiments PLGA:porogen ratio was 1:10. This ratio was used because; in case porogen content is sufficiently high, the resulting pores must be with some interconnectivity simply due to geometrical packing. The sediment was placed into the Petri dish and allowed to dry overnight at room temperature. The dried polymer films were removed from the Petri dish and soaked in appropriate solvent for 72 h to remove the porogen. The solvent was changed, approximately, every 12 h to allow the porogen to leach out. Paraffin as porogen has been removed from polymeric film with cyclohexane, silicone oil with n-heptan and sodium chloride with distilled water. This was repeated several times to remove the porogen in its entirety. PLGA films were vacuum dried (Vaciotem P-Selecta) for 48 h to allow the solvent to evaporate.

2.3. The structural analysis of the samples

In order to investigate the characteristics of the PLGA particles and PLGA porous materials obtained with different porogens i.e. to confirm the quality composition of the samples, X-ray diffraction (XRD) has been used. Phase analyses were performed by XRD, using a Philips PW 1050 diffractometer with Cu-$K_{\alpha 1,2}$ radiation (Ni filter). Measurements were done in 2θ range of 10–70° with scanning step width of 0.05° and 2 s of time per step.

The quality analysis of the samples was, also, performed using IR spectroscopy. IR spectra were recorded in the range of 400–4000 cm^{-1} at a MIDAC M 2000 Series Research Laboratory FTIR Spectrometer, at 4 cm^{-1} resolution.

2.4. Zeta potential measurements

Zeta potential was measured by Zetasizer (Nano ZS, Model ZEN3600, particles size range for zeta potential determination (5 nm–10 μm), Malvern Instruments, Malvern, UK) using the principle of electrophoretic mobility under an electric field. Zeta potential is the function of dispersion/suspension pH which determines particle stability in dispersion.

2.5. Determining intracellular reactive oxygen species formation – DCFH-DA assay

The formation of intracellular reactive oxygen species (ROS) was measured spectrophotometrically using a fluorescent probe, DCFH-DA as described by Osseni *et al*. [30], with minor modifications [32]. DCFH-DA readily diffuses through the cell membrane and is hydrolyzed by intracellular esterases to non-fluorescent 2′,7′-dichlorofluorescin. It is then rapidly oxidized to highly fluorescent 2′,7′-dichlorofluorescein in the presence of ROS. The DCF fluorescence intensity is proportional to the amount of reactive oxygen species formed intracellularly. H_2O_2 is the principle ROS responsible for the oxidation of DCFH-DA to DCF [33].

In this assay we used cells HepG2, which were grown in Minimal Essential Medium Eagle medium containing 10% foetal bovine serum, 1% non-essen-

tial amino acid solution, 2 mM L-glutamine and 100 U/ml penicillin plus 100 μg/ml streptomycin at 37°C in humidified atmosphere and 5% CO_2.

HepG2 cells were seeded at a density of 75 000 cells/ml into 96-well, black, tissue culture treated microtiter plates (Nunc, Naperville IL, USA) in five replicates. After 20 h of incubation at 37°C in 5% CO_2, cells were incubated with 20 μM DCFH-DA. After 30 min, DCFH-DA was removed and cells were treated with 0, 1, 10, 25, 50 and 66,5 μg/ml of PLGA nanoparticles without porogens in PBS. In each experiment were included negative control (non-treated cells), positive control (0,5 mM t-BOOH) and a vehicle control (5% emulsion; emulsion consists of acetone, ethanol and PVP, in the same ratio as used in the experiment, without PLGA) in order to exclude possible effects of the solvent (emulsion). For kinetic analyses the dishes were maintained at 37°C and the fluorescence intensity was determined every 30 min during the 5 h incubation using a microplate reading spectrofluorimeter (Tecan, Genios) at the excitation wavelength of 485 nm and the emission wavelength of 530 nm.

Statistical significance between treated groups and controls was determined by two tailed Student's t-test and $P<0.05$ was considered as statistically significant. Two independent experiments with five replicates were performed.

In our study we tested ROS-inducing potential of PLGA nanoparticles without porogens only and we did not test ROS-inducing potential of porous PLGA material, since it is much more difficult to perform testing of material in form of the scaffold than of particles that can be dispersed. Testing of materials in the form of scaffold requires seeding of cells onto material surface instead of seeding onto plastic surfaces, which is regularly used for *in vitro* toxicology tests. For the analysis of ROS-inducing potential of such material it is necessary to detach the cells from the material (with trypsinization or cell scraping), process that itself generates cellular oxidative stress and result in artificial changes in fluorescence, due to which we can observe false positive results. Because of this we tested only ROS-inducing potential of PLGA nanoparticles without porogens.

2.6. Morphology studies

The morphology of obtained nano and microparticles and porous samples was evaluated by scanning electron microscope (SEM) (JEOL JSM-639OLV) and SUPRA 35 VP Carl Zeiss field emission scanning electron microscope (FESEM). The powder samples for SEM analysis were coated with gold using the physical vapour deposition (PVD) process. Samples were covered with gold (Baltec SCD 005 sputter coater), using 30 mA current from the distance of 50 mm during 180 s. SEM recordings were, also, used to obtain information about profiles and sizes of the particles and pores.

2.7. Water absorption

Water absorption of the polymeric films or scaffolds was measured in the manner described in detail elsewhere [34–38]. Water absorption was measured by immersing the samples in distilled water for a predetermined time span (55 hours), then the samples were taken out and dried by removing the free water on the surface with filter paper and weighed (W1). Then the samples were thoroughly vacuum-dried and weighed again (W2). The water absorption could be calculated as shown in Equation (1) and five specimens were averaged.

$$\text{Water absorption}\,[\,\%\,] = \frac{W1 - W2}{W2} \cdot 100 \quad (1)$$

2.8. *In vitro* degradation studies

The degradation of PLGA nanoparticles and PLGA porous materials obtained with sodium chloride as porogen were studied during the 39 days in phosphate buffered saline as a degradation medium.

Taking into account that the degradation products of PLGA, among others, are lactic and glycolic acid [31], a calibration curve for lactic acid was made. By tracking the increase of the concentration of lactic acid in the solution, the degradation of the samples was monitored.

The concentration of lactic acid in the phosphate buffered saline as a release medium was determined by UV spectroscopy. Based on measuring absorbance of the solution with a known concentration of lactic acid at 220 nm, a calibration curve was prepared. The linear relationship between light absorbance at

220 nm and lactic acid concentration is shown according to the Beer-Lambert Law (Equation (2)):

$$A = \varepsilon cl \quad (2)$$

where A is absorbance at sample concentration c (in this case concentration of the lactic acid [mg/ml]), l is path length of quartz cell and ε is the absorptivity. By applying this standardized relationship, PBS solution, in which the samples were suspended, was analyzed to determine the concentration and amount of lactic acid as product of the degradation of PLGA samples whether it is porous or whether it is not porous. The *in vitro* degradation of PLGA nanoparticles and PLGA porous materials obtained with sodium chloride as porogen was studied by suspending samples in PBS in the absence of light at 37±1ºC (VIMS elektrik, SCG). Measurements of the degradation of both samples were undertaken by exposing 2 mg of the sample to 2 ml of PBS. The UV measurements were performed on GBC, Cintra 101 UV-VIS Spectrophotometer in the frequency interval of 200–400 nm.

2.9. pH measurements

The pH of the physiological solution has been measured using pH indicator strips obtained from Merck (KGaA, Germany) at various time periods (during the 39 days) to follow the acidity of the degrading medium with time.

3. Results and discussion

3.1. The structural analysis of the samples

The IR spectra illustrate all characteristic groups for copolymer poly(DL-lactide-coglycolide). The IR spectra of PLGA show peaks at 2995, 2948 , 2841 cm^{-1} (C–H bend of the $–CH_2$ and $–CH_3$ group), 1769 cm^{-1} (C=O ester), 1461, 1425, 1370 cm^{-1} (C–H bend of the CH_3 group), 1150, 1069, 987 cm^{-1} (C–O stretch), 735, 510 cm^{-1} (C–H bend). The IR spectra, also, shows a broad band in the range 3100–3600 cm^{-1} which belongs to the OH− group of the water molecule [39, 40].

The X-ray diffractograms of PLGA nanoparticles and PLGA porous materials are presented in Figure 1. PLGA did not exhibit any crystalline peak under the present experimental conditions because PLGA is amorphous. Also, X-ray patterns show that there is no presence of residual porogens in the samples (Figure 1b–d). On the Figure 1e strong background and the up-shift of the broad structure can be observed. We may assume this is probably related to residual sodium chloride. However, as known from the literature [41], sodium chloride is crystalline and has strong peaks at 2θ = 31.8, 45.6 and 66.2º assigned to (200), (400) and (220) planes respectively, which are not present. Thus we conclude the amount of the residual sodium chloride is negligible.

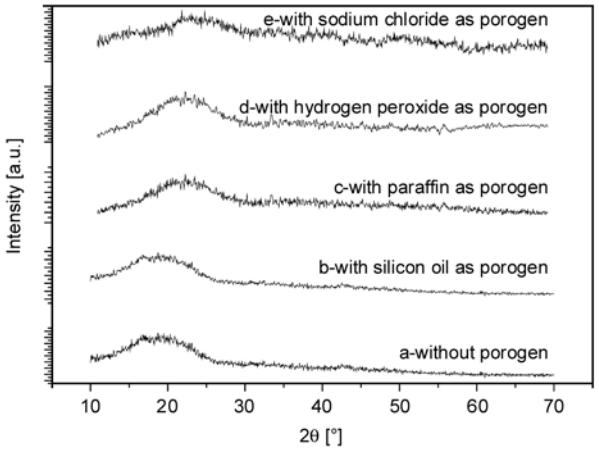

Figure 1. XRD patterns of a) PLGA particles prepared without porogen, b) PLGA obtained with silicone oil as porogen and n-heptan as solvent of the porogen; c) PLGA obtained with paraffin as porogen and cyclohexane as solvent of the porogen; d) PLGA obtained with hydrogen peroxide and e) PLGA obtained with sodium chloride as porogen and water as solvent of the porogen

3.2. Zeta potential measurements

PVP was used as a stabilizer which creates negatively charged PLGA particles, that is, induces a specific zeta potential. PVP reduces the agglomeration because the particles of the same charge are not attracted to each other. A refractive index (RI) value of 1.4 was used in determination of the size of nanoparticles. The RI value is estimated from product literature values for the RI of polylactic acid (1.35–1.45, Natureworks LLC) and for the monomers (lactic acid = 1.42, glycolic acid = 1.41, Sigma-

Table 1. Zeta potential of PLGA dispersion and size of PLGA particles in dispersion

	Particle size [nm]	pH	Polydispersity index	Zeta potential [mV]
PLGA2	275±5	4.30–4.37	0.053	–9.5±0.3

Values given are mean ± standard deviation (n = 5).

Aldrich Corp.) [42]. The polydispersity index (PDI) which is a dimensionless number indicating the width of the size distribution, having a value between 0 and 1 (0 being for monodispersed particles) was also obtained (Table 1).

Values for the size of particles from the dispersion of the same sample determined by Malvern particle analyzer were bigger from the values obtained by SEM for particles of the powder of the same sample. The reason is, as we reported earlier [43], that time and velocity of centrifugal processing influences the morphology (size and shape) and uniformity of PLGA polymer powder. An influence of the centrifugation process on the particle sizes is supported by the fact that coefficient of friction for smaller and more compact spherical particles is less than those with irregular shapes and same mass, which makes spherical particles sediment faster [43]. Also, values for sizes of the particles in the dispersion can be bigger because of the hydrodynamic effect, layer of ions around the particles, aggregates of the particles, etc [44].

3.3. Induction of intracellular ROS formation

HepG2 cells are of human origin and retain many of the specialized liver functions and drug metabolizing enzyme activities present in human hepatocytes. They are considered to better reflect the processes in normal human liver than other *in vitro* toxicity test systems. In our previous study we have shown that exposure of HepG2 cells to 0, 1, 10, 25, 50 and 66,5 μg/ml of PLGA nanoparticles for 24 h did not affect the viability of the cells [18]. Therefore, these concentrations were used in further experiments.

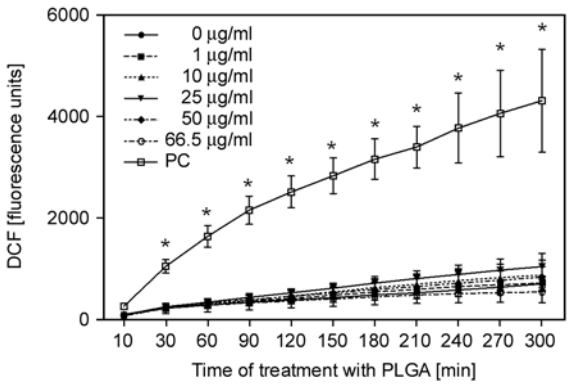

Figure 2. PLGA-induced intracellular ROS formation in HepG2 cells. The HepG2 cells were pretreated with DCFH-DA (20 μM) for 30 min, washed and then exposed to different concentrations of PLGA (0, 1, 10, 25, 50 and 66,5 μg/ml) or 0,5 mM t-BOOH as the positive control (PC). DCF fluorescence intensity was measured at 30 min intervals during the 5 h incubation. Each point represents the mean of five replicates (±SD) of two independent experiments. (*) denotes a significant difference ($p < 0,05$).

Exposure of HepG2 cells to PLGA nanoparticles did not induce significant increase of DCF fluorescence intensity, while exposure to *t*-BOOH, the positive control, induced significant, up to six fold increase in DCF fluorescence intensity over the control, non-treated cells (Figure 2). Based on these results we conclude that PLGA nanoparticles are not inducers of intracellular ROS formation.

3.4. Morphology studies

The morphological characteristics of the particles are extremely important for the controlled drug delivery and tissue engineering and particularly influence the adhesion and interaction with cells (intracellular uptake). Dynamics of the release (rate and concentration) depends on the morphology, i.e. structure of the copolymer.

The morphological characteristics of PLGA particles and PLGA porous materials obtained with different porogens, were observed by a scanning electron microscope. Different morphologies of PLGA were prepared using no porogen, and silicon oil, paraffin, hydrogen peroxide or sodium chloride as porogens. By using different porogens the samples with diferent morphological characteristics, at macroscopic and as well on microscopic level, were obtained.

From the micrograph of non-porous PLGA particles it is visible the particles have spherical shape, smooth surface, low level of agglomeration and high level of uniformity (Figure 3). The size distribution of all nanoparticles was unimodal with sizes of about 100–200 nm. The particles are without cracks and pores.

From SEM images of PLGA material obtained in the experiment with silicone oil as porogen and n-heptan as solvent of the porogen it is visible that use of silicon oil as porogen has no major impact on the formation of pores in the sample (Figure 4). The particles are much agglomerated and they create the film. On the film cracks and roughness can be seen. In the sample spherical particles of smaller and larger sizes that are distributed sporadically are still present.

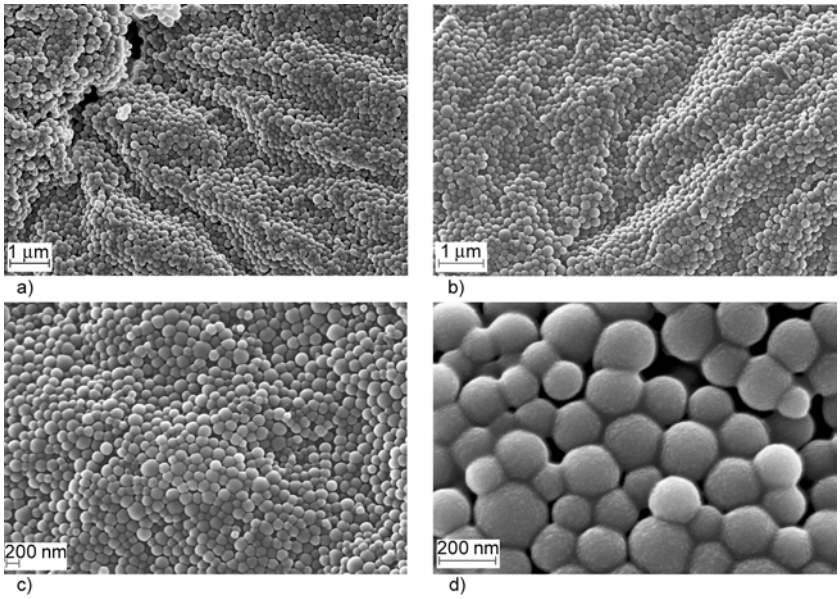

Figure 3. FESEM images of PLGA particles obtained in the experiment without porogen (a–d)

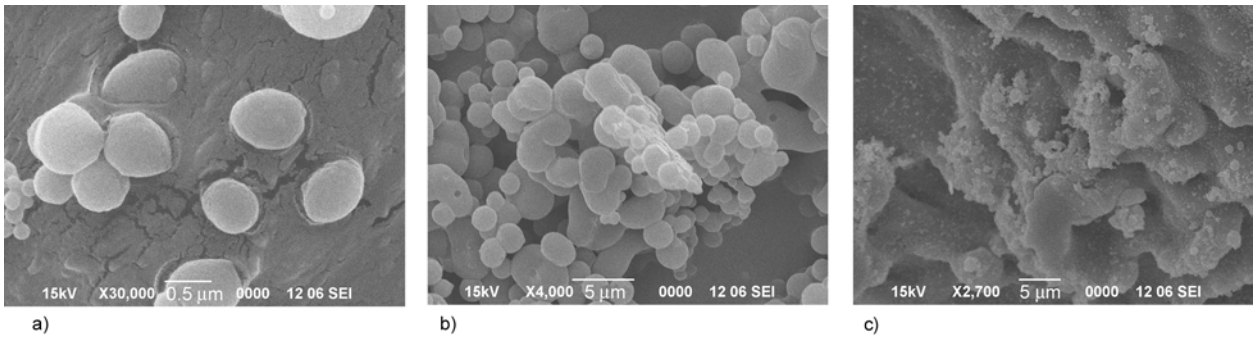

Figure 4. SEM images of PLGA material obtained in the experiment with silicone oil as porogen and n-heptan as solvent of the porogen (a–c)

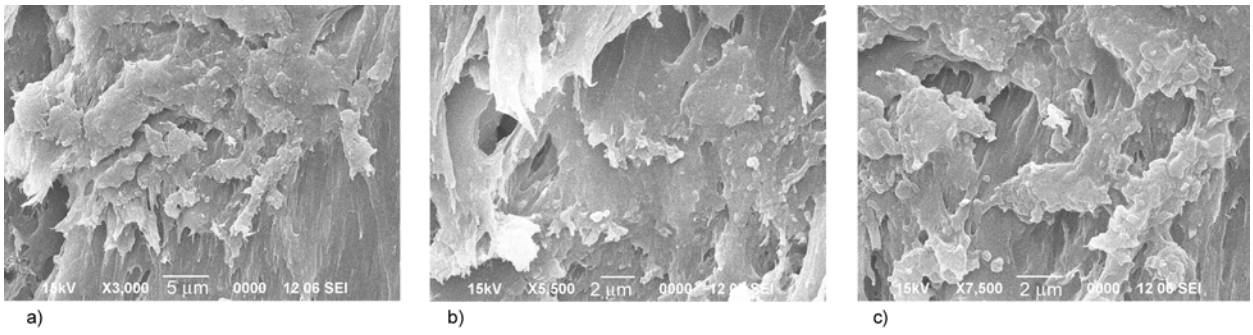

Figure 5. SEM images of PLGA material obtained in the experiment with paraffin as porogen and cyclohexane as solvent of the porogen (a–c)

SEM images revealed porous morphologies of the samples when paraffin was used in the experiment as porogen and cyclohexane as solvent of the porogen (Figure 5). We can see from SEM micrographs that the resulting pores are with irregular shapes and without a good interconnectivity.

Figure 6 shows SEM observation of the interior pore structure of PLGA material obtained in the experiment when hydrogen peroxide was used as porogen. In this case the sample with high porosity and with good interconnectivity was obtained. The pores are with spherical but also irregular shapes. The pore size has mean value of about 10 µm.

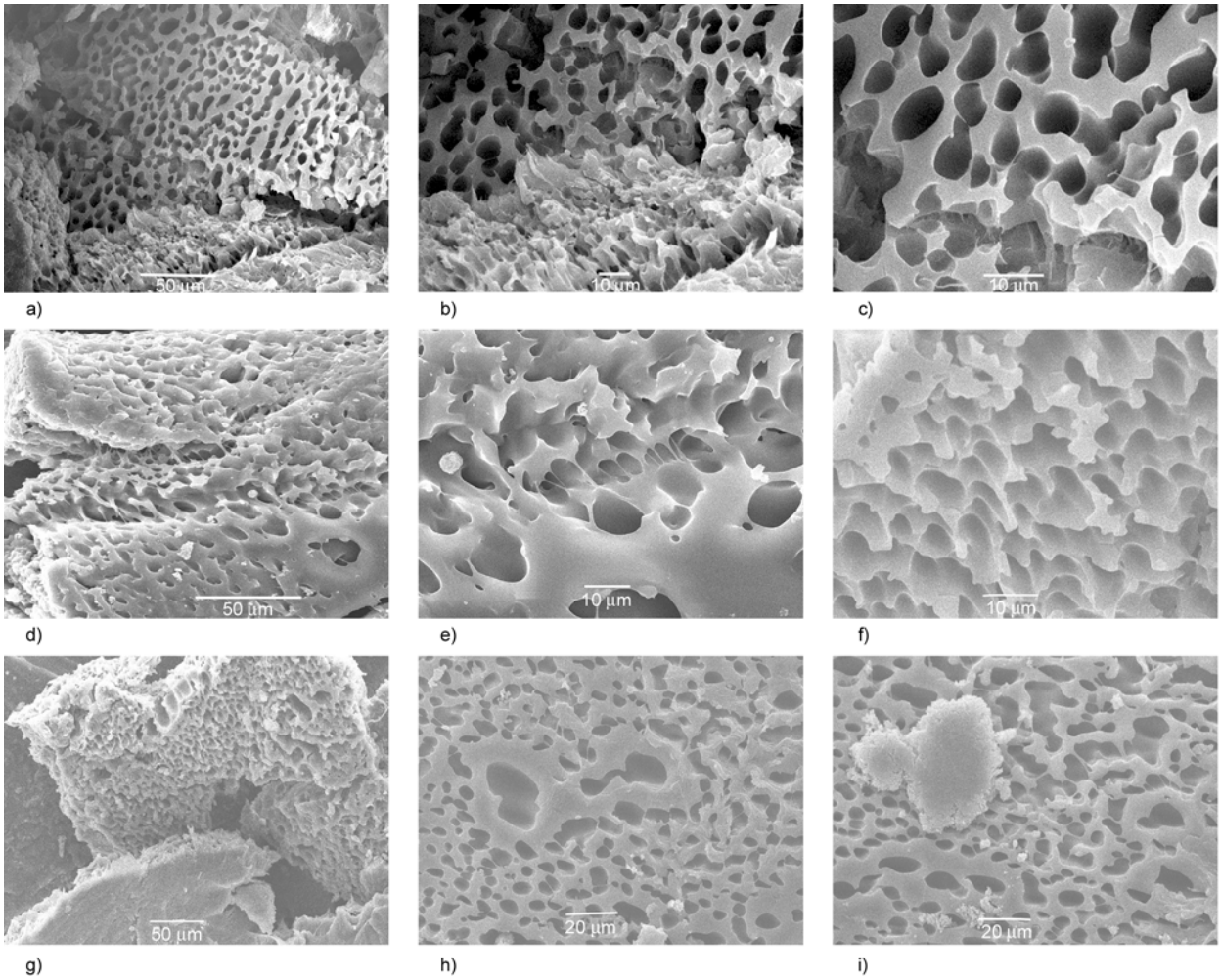

Figure 6. SEM images of PLGA material obtained in the experiment with hydrogen peroxide as porogen (a–i)

Figure 7a–b shows digital photographs of PLGA material obtained with sodium chloride as porogen. PLGA porous material appeared well formed and a highly porous sponge-like where the pores are similar in the size and shape.

The optimum morphological characteristics were obtained when sodium chloride was used as pore former. SEM micrographs showed that porous PLGA scaffolds obtained in the experiment with sodium chloride as porogen and water as solvent of the porogen had apparently uniform pore morphology with spheroidal pore in shape and well controlled three-dimensional interconnected network (Figure 7c–f). This PLGA samples are highly porous with similar porosity values. The pore size varies from 50 to 150 µm based on SEM images. The unified and well organized porous structure can be seen. It is evident that pores have more precise contours.

3.5. Water absorption

In the literature, it has been reported that wetting of a polymer scaffold is very important for homogeneous and sufficient cell seeding throughout the porous scaffold [38]. To evaluate hydrophilicity of PLGA porous samples water absorption was measured. The water absorption of the samples changed with their porosity (Figure 8). PLGA porous scaffolds obtained with sodium chloride as porogen exhibited higher water absorption than other samples. It could be seen that the water absorption increased with the degree of porosity increasing and all the samples had higher water absorption than non-porous PLGA.

3.6. Degradation studies

The degradation of PLGA particles and PLGA porous materials obtained with sodium chloride as porogen was measured in PBS as a degradation

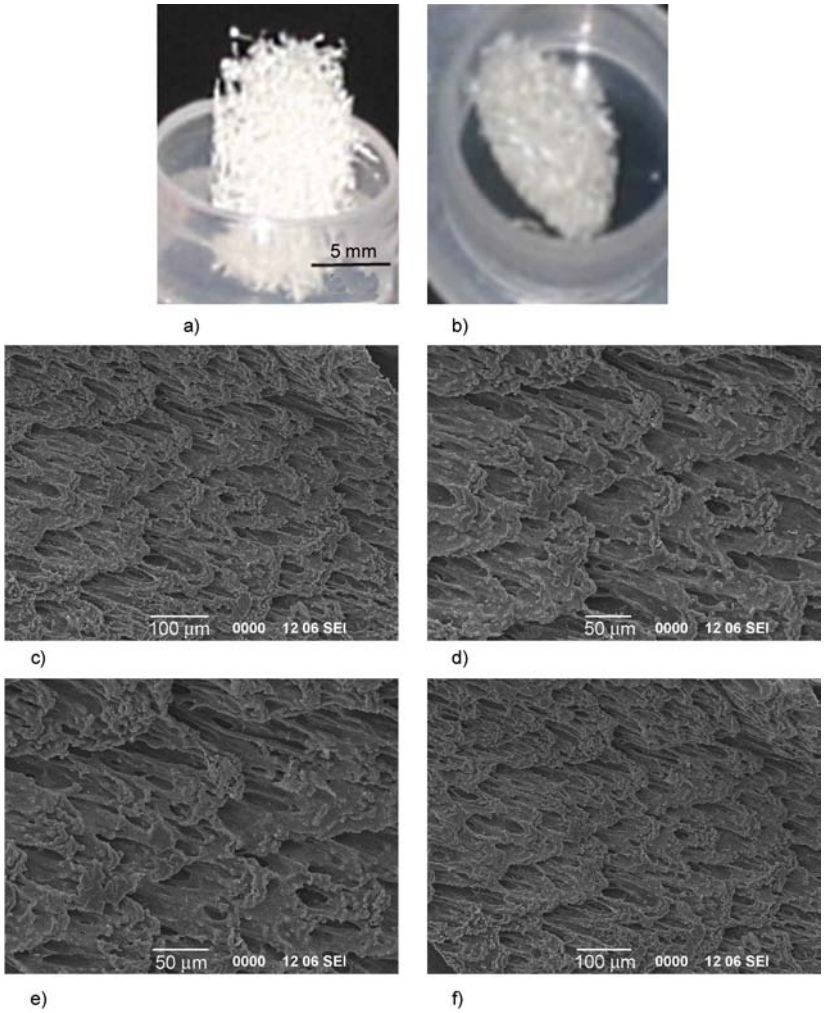

Figure 7. a–b) Macroscopic observation of PLGA scaffold obtained with NaCl as pore former and c–f) SEM images of PLGA material obtained in the experiment with sodium chloride as porogen and water as solvent of the porogen

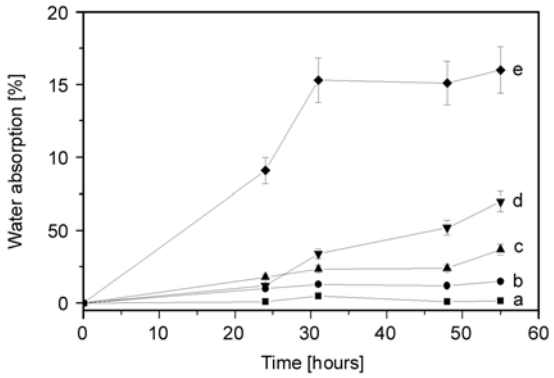

Figure 8. Change of water absorption of various PLGA porous samples in comparison with non-porous PLGA as function of time: a) non-porous PLGA particles; b) porus PLGA material obtained with silicone oil as porogen and n-heptan as solvent of the porogen; c) with paraffin as porogen and cyclohexane as solvent of the porogen; d) with hydrogen peroxide as porogen and e) with sodium chloride as porogen and water as solvent of the porogen

medium during the 39 days (Table 2). By the end of 39 days, the samples have fully degraded and there were no more traces of them in the solution. Literature describes two approaches for the study of polymeric degradation and they vary according to whether examination is under dynamic or static conditions [45]. In our case degradation of non-porous and porous PLGA was measured under static conditions. It was observed, the degradation medium, in which porous PLGA was suspended, at the beginning of the process of the degradation (measured in the second day), contains much more lactic acid than degradation medium in which PLGA nanoparticles were suspended, which means porous PLGA degrades faster (Table 2 gives cumulative concentrations of the released lactic acid). The release-delayed phenomenon of macromolecular drug delivery system at the early stage of the degradation was eliminated in the case of porous PLGA

Table 2. The concentration of lactic acid calculated on the basis of absorbance at the wavelength of absorption maximum at 220 nm from spectra recorded after 39 days of the degradation and calibration curve for lactic acid

	Absorbance at 220 nm		Concentration [mg/ml]	
	After two days	After 39 days	After two days	After 39 days
PLGA	0.068	0.507	0.07	1.00
Porous PLGA (NaCl as pore former)	0.242	0.561	0.42	1.12

The data are presented as mean values of three independent

obtained with sodium chloride as porogen and water as solvent of the porogen. The explanation for this phenomenon is very simple. During the degradation process the non-porous PLGA particles are in a very close contact which brings to higher agglomeration of the particles and creation of the porous film [18]. The degradation of the PLGA becomes faster when the degradation medium passes through the polymeric membrane, i.e. the degradation is more rapid when polymeric film becomes sufficiently porous. We have already elaborated this process elsewhere [18]. The sample obtained in the experiment with sodium chloride as porogen and water as solvent of the porogen has already porous structure so degradation becomes more rapid without delay, i.e. immediately and so the release of, potentially encapsulated, drug will be starting, also, without delay.

3.7. pH measurements

The pH of PBS solution has begun to decrease, approximately, after 48hrs of storage, in the case of porous PLGA when sodium chloride was used as pore former as well as in the case of non-porous PLGA (Figure 9). This is presumably due to an accumulation of lactic and glycolic acid. PLGA degrades via backbone hydrolysis (bulk erosion) and the degradation products are the monomers, lactic acid and glycolic acid. It could be expected that the faster degradation of the lower molar mass fraction, present in copolymer, increases the local acidity, thereby, accelerating the hydrolysis of higher molar mass species. In another words, when acid accumulation creates a local pH drop, catalytic degradation of the polymer itself occurs [24]. The pH of PBS medium in which porous PLGA scaffold was stored decreases faster at the beginning of the degradation and the reason for these phenomena is that the degradation medium diffuse through the sample i.e. medium passes into pores of the sample. Also, as already noted, PLGA porous scaffolds obtained with sodium chloride as porogen exhibited

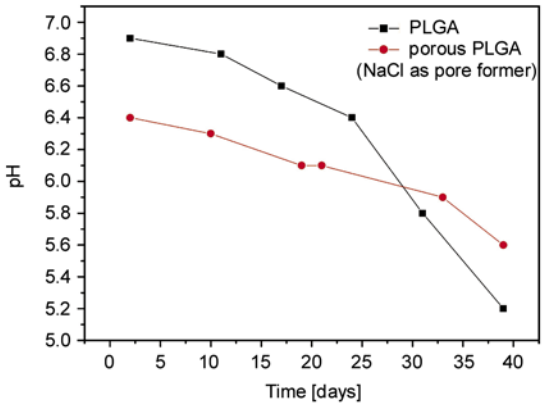

Figure 9. Changes in the pH of the degradation medium with time for the PLGA in the case of a) non porous PLGA nanoparticles and b) porous PLGA obtained when sodium chloride was used as pore forme

higher water absorption than other samples and degradation medium in which PLGA porous scaffolds were suspended contains more lactic acid after two days of the degradation. In the case of non-porous PLGA, during the degradation process the particles are in a very close contact which leads to higher agglomeration of the particles and formation of the porous film [18]. The degradation becomes more rapid when polymeric film becomes sufficiently porous. Because of that, after approximately 20 days, degradation of newly generated porous film (initially non-porous PLGA particles) becomes faster and thus it comes to a faster decrease of pH than in the case of pH of the porous PLGA scaffold. Thin PLGA films degraded faster than thick scaffold because thin films had a greater surface area to volume ratio and thus a greater extent of degradation medium uptake.

4. Conclusions

The physicochemical method has produced non-agglomerated PLGA nanospheres with spherical and uniform shapes. We have shown that PLGA nanospheres are not cytotoxic and they do not induce increased production of ROS for HepG2 cells *in*

vitro, which is an optimistic result for usage of PLGA nanospheres for *in vivo* applications. Porous poly (DL-lactid-co-glycolid) materials were fabricated using different porogens, silicon oil, paraffin, hydrogen peroxide or sodium chloride. It was found that silicon oil as porogen has no major impact on the formation of pores in the sample. Paraffin leads to the formation of pores with irregular shapes and without a good interconnectivity. When hydrogen peroxide was used as porogen, sample with high porosity and with good interconnectivity was obtained but pore size has mean value only of about 10 μm. SEM micrographs showed that porous PLGA scaffolds obtained in the experiment with sodium chloride as porogen and water as solvent of the porogen had apparently uniform pore morphology with spherical pore in shape and well controlled three-dimensional interconnected network. These PLGA samples are highly porous with similar porosity values and exhibit higher water absorption than porous samples obtained with another porogens. To eliminate the release-delayed phenomenon of PLGA macromolecular drug delivery system at the early stage, biodegradable implantable drug delivery system with porous structure was designed when sodium chloride was used as pore former and by physicochemical solvent/non-solvent method. An important clinical application of this porous PLGA material is reflected in the case of many chronic diseases where long term therapy is needed, but one has to start treatment immediately. Besides for the controlled delivery of drugs, this porous material is also very suitable in many other biomedical applications, for example in tissue engineering because it provides the required properties needed for the survival of cells (cell adhesion, proliferation, migration, and/or differentiation) and formation of tissue.

Acknowledgements

This study was supported by the Ministry of Science and Technological Development of the Republic of Serbia, under Grant No. III45004: Molecular designing of nanoparticles with controlled morphological and physicochemical characteristics and functional materials based on them. The authors would like to thank to Ljiljana Kandić for X ray measurements, Srečo Škapin for FESEM analysis and Slobodan Milonjić for zeta potential measurements.

References

[1] Lim H. J., Ghim H. D., Choi J. H., Chung H. Y., Lim J. O.: Controlled release of BMP-2 from alginate nanohydrogels enhanced osteogenic differentiation of human bone marrow stromal cells. Macromolecular Research, **18**, 787–792 (2010).
DOI: 10.1007/s13233-010-0804-6

[2] Wang Z. H., Wang Z. Y., Sun C. S., Wang C. Y., Jiang T. Y., Wang S. L.: Trimethylated chitosan-conjugated PLGA nanoparticles for the delivery of drugs to the brain. Biomaterials, **31**, 908–915 (2010).
DOI: 10.1016/j.biomaterials.2009.09.104

[3] Gupta A., Vara D. S., Punshon G., Sales K. M., Winslet M. C., Seifalian A. M.: *In vitro* small intestinal epithelial cell growth on a nanocomposite polycaprolactone scaffold. Biotechnology and Applied Biochemistry, **54**, 221–229 (2009).
DOI: 10.1042/BA20090214

[4] Pattison M. A., Wurster S., Webster T. J., Haberstroh K. M.: Three-dimensional, nano-structured PLGA scaffolds for bladder tissue replacement applications. Biomaterials, **26**, 2491–2500 (2005).
DOI: 10.1016/j.biomaterials.2004.07.011

[5] Thapa A., Miller D. C., Webster T. J., Haberstroh K. M.: Nano-structured polymers enhance bladder smooth muscle cell function. Biomaterials, **24**, 2915–2926 (2003).
DOI: 10.1016/S0142-9612(03)00123-6

[6] Melchels F. P. W., Feijen J., Grijpma D. W.: A poly (D,L-lactide) resin for the preparation of tissue engineering scaffolds by stereolithography. Biomaterials, **30**, 3801–3809 (2009).
DOI: 10.1016/j.biomaterials.2009.03.055

[7] Blanco T. M., Mantalaris A., Bismarck A., Panoskaltsis N.: The development of a three-dimensional scaffold for *ex vivo* biomimicry of human acute myeloid leukaemia. Biomaterials, **31**, 2243–2251 (2010).
DOI: 10.1016/j.biomaterials.2009.11.094

[8] Bonartsev A. P., Livshits V. A., Makhina T. A., Myshkina V. L., Bonartseva G. A., Iordanskii A. L.: Controlled release profiles of dipyridamole from biodegradable microspheres on the base of poly(3-hydroxybutyrate). Express Polymer Letters, **1**, 797–803 (2007).
DOI: 10.3144/expresspolymlett.2007.110

[9] Sun K., Li Z. H.: Preparations, properties and applications of chitosan based nanofibers fabricated by electrospinning. Express Polymer Letters, **5**, 342–361 (2011).
DOI: 10.3144/expresspolymlett.2011.34

[10] Fuchs S., Jiang X., Gotman I., Makarov C., Schmidt H., Gutmanas E. Y., Kirkpatrick C. J.: Influence of polymer content in Ca-deficient hydroxyapatite–polycaprolactone nanocomposites on the formation of microvessel-like structures. Acta Biomaterialia, **6**, 3169–3177 (2010).
DOI: 10.1016/j.actbio.2010.02.001

[11] Park C. H., Hong Y. J., Park K., Han D. K.: Peptide-grafted lactide-based poly(ethylene glycol) porous scaffolds for specific cell adhesion. Macromolecular Research, **18**, 526–532 (2010).
DOI: 10.1007/s13233-010-0517-9

[12] Wang Y., Shi X., Ren L., Wang C., Wang D-A.: Porous poly (lactic-co-glycolide) microsphere sintered scaffolds for tissue repair applications. Materials Science and Engineering C, **29**, 2502–2507 (2009).
DOI: 10.1016/j.msec.2009.07.018

[13] Liu S-J., Hsueh C-L., Ueng S. W-N., Lin S-S., Chen J-K.: Manufacture of solvent-free polylactic-glycolic acid (PLGA) scaffolds for tissue engineering. Asia-Pacific Journal of Chemical Engineering, **4**, 154–160 (2009).
DOI: 10.1002/apj.187

[14] Stevanović M., Radulović A., Jordović B., Uskoković D.: Poly(DL-lactide-*co*-glycolide) nanospheres for the sustained release of folic acid. Journal of Biomedical Nanotechnology, **4**, 349–358 (2008).
DOI: 10.1166/jbn.2008.321

[15] Zhang J., Rana S., Srivastava R. S., Misra R. D. K.: On the chemical synthesis and drug delivery response of folate receptor-activated, polyethylene glycol-functionalized magnetite nanoparticles. Acta Biomaterialia, **4**, 40–48 (2008).
DOI: 10.1016/j.actbio.2007.06.006

[16] Abdelwahed W., Degobert G., Stainmesse S., Fessi H.: Freeze-drying of nanoparticles: Formulation, process and storage considerations. Advanced Drug Delivery Reviews, **58**, 1688–1713 (2006).
DOI: 10.1016/j.addr.2006.09.017

[17] Zhang H., Chen Z.: Fabrication and characterization of electrospun PLGA/MWNTs/hydroxyapatite biocomposite scaffolds for bone tissue engineering. Journal of Bioactive and Compatible Polymers, **25**, 241–258 (2010).
DOI: 10.1177/0883911509359486

[18] Stevanović M., Maksin T., Petković J., Filipič M., Uskoković D.: An innovative, quick and convenient labeling method for the investigation of pharmacological behavior and the metabolism of poly(DL-lactide-co-glycolide) nanospheres. Nanotechnology, **20**, 335102/1–335102/12 (2009).
DOI: 10.1088/0957-4484/20/33/335102

[19] Wei G., Ma P. X.: Polymer/ceramic composite scaffolds for bone tissue engineering. in 'Scaffolding in tissue engineering' (eds.: Ma P. X., Elisseeff J.) CRC Press, Boca Raton, 241–251 (2006).

[20] Sha'ban M., Kim S. H., Idrus R. B. H., Khang G.: Fibrin and poly(lactic-co-glycolic acid) hybrid scaffold promotes early chondrogenesis of articular chondrocytes: An *in vitro* study. Journal of Orthopaedic Surgery and Research, **3**, 17/1–17/10 (2008).
DOI: 10.1186/1749-799X-3-17

[21] Lee J. J., Lee S-G., Park J. C., Yang Y. I., Kim J. K.: Investigation on biodegradable PLGA scaffold with various pore size structure for skin tissue engineering. Current Applied Physics, **7**, 37–40 (2007).
DOI: 10.1016/j.cap.2006.11.011

[22] Dawes G. J. S., Fratila-Apachitei L. E., Mulia K., Apachitei I., Witkamp G-J., Duszczyk J.: Size effect of PLGA spheres on drug loading efficiency and release profiles. Journal of Materials Science: Materials in Medicine, **20**, 1089–1094 (2009).
DOI: 10.1007/s10856-008-3666-0

[23] Blanco M. D., Sastre R. L., Teijón C., Olmo R., Teijón J. M.: Degradation behaviour of microspheres prepared by spray-drying poly(D,L-lactide) and poly(D,L-lactide-*co*-glycolide) polymers. International Journal of Pharmaceutics, **326**, 139–147 (2006).
DOI: 10.1016/j.ijpharm.2006.07.030

[24] Ito F., Fujimori H., Makino K.: Factors affecting the loading efficiency of water-soluble drugs in PLGA microspheres. Colloids and Surfaces B: Biointerfaces, **61**, 25–29 (2008).
DOI: 10.1016/j.colsurfb.2007.06.029

[25] Krebs M. D., Sutter K. A., Lin A. S. P., Guldberg R. E., Alsberg E.: Injectable poly(lactic-co-glycolic) acid scaffolds with *in situ* pore formation for tissue engineering. Acta Biomaterialia, **5**, 2847–2859 (2009).
DOI: 10.1016/j.actbio.2009.04.035

[26] Stevanović M., Uskoković D.: Poly(lactide-co-glycolide)-based micro and nanoparticles for the controlled drug delivery of vitamins, review article. Current Nanoscience, **5**, 1–14 (2009).

[27] Rabelo D., Lima E. C. D., Reis A. C., Nunes W. C., Novak M. A., Garg V. K., Oliveira A. C., Morais P. C.: Preparation of magnetite nanoparticles in mesoporous copolymer template. Nano Letters, **1**, 105–108 (2001).
DOI: 10.1021/nl005533k

[28] Kim S., Choi J. E., Choi J., Chung K-H., Park K., Yi J., Ryu D-Y.: Oxidative stress-dependent toxicity of silver nanoparticles in human hepatoma cells. Toxicology in Vitro, **23**, 1076–1084 (2009).
DOI: 10.1016/j.tiv.2009.06.001

[29] Schins R. P. F., Knaapen A. M.: Genotoxicity of poorly soluble particles. Inhalation Toxicology, **19**, 189–198 (2007).
DOI: 10.1080/08958370701496202

[30] Osseni R. A., Debbasch C., Christen M-O., Rat P., Warnet J-M.: Tacrine-induced reactive oxygen species in a human liver cell line: The role of anethole dithiolethione as a scavenger. Toxicology in Vitro, **13**, 683–688 (1999).
DOI: 10.1016/S0887-2333(99)00050-8

[31] Stevanović M., Savić J., Jordović B., Uskoković D.: Fabrication, in vitro degradation and the release behaviours of poly(DL-lactide-co-glycolide) nanospheres containing ascorbic acid. Colloids and Surfaces B: Biointerfaces, **59**, 215–223 (2007).
DOI: 10.1016/j.colsurfb.2007.05.011

[32] Petković J., Žegura B., Stevanović M., Drnovšek N., Uskoković D., Novak S., Filipič M.: DNA damage and alterations in expression of DNA damage responsive genes induced by TiO_2 nanoparticles in human hepatoma HepG2 cells. Nanotoxicology, in press (2011). DOI: 10.3109/17435390.2010.507316

[33] LeBel C. P., Ischiropoulos H., Bondy S. C.: Evaluation of the probe 2′,7′-dichlorofluorescin as an indicator of reactive oxygen species formation and oxidative stress. Chemical Research in Toxicology, **5**, 227–231 (1992). DOI: 10.1021/tx00026a012

[34] Zhang J., Wu L., Jing D., Ding J.: A comparative study of porous scaffolds with cubic and spherical macropores. Polymer, **46**, 4979–4985 (2005). DOI: 10.1016/j.polymer.2005.02.120

[35] Cai Q., Yang J., Bei J., Wang S.: A novel porous cells scaffold made of polylactide–dextran blend by combining phase-separation and particle-leaching techniques. Biomaterials, **23**, 4483–4492 (2002). DOI: 10.1016/S0142-9612(02)00168-0

[36] Perugini P., Genta I., Conti B., Modena T., Pavanetto F.: Periodontal delivery of ipriflavone: New chitosan/PLGA film delivery system for a lipophilic drug. International Journal of Pharmaceutics, **252**, 1–9 (2003). DOI: 10.1016/S0378-5173(02)00602-6

[37] Boccaccini A. R., Blaker J. J., Maquet V., Chung W., Jérôme R., Nazhat S. N.: Poly(D,L-lactide) (PDLLA) foams with TiO_2 nanoparticles and PDLLA/TiO_2-Bioglass® foam composites for tissue engineering scaffolds. Journal of Materials Science, **41**, 3999–4008 (2006). DOI: 10.1007/s10853-006-7575-7

[38] Woo Y. I., Lee M. H., Kim H-L., Park J-C., Han D-W., Kim J. K., Tsubaki K., Chung K-H., Hyun S. O., Yang Y-I.: Cellular responses and behaviors of adipose-derived stem cells onto β-glucan and PLGA composites surface-modified by microwave-induced argon plasma. Macromolecular Research, **18**, 90–93 (2010). DOI: 10.1007/s13233-009-0125-9

[39] Kiremitçi-Gümüşderelioğlu M., Deniz G.: Synthesis, characterization and in vitro degradation of poly(DL-lactide)/poly(DL-lactide-co-glycolide) films. Turkish Journal of Chemistry, **23**, 153–162 (1999).

[40] Yang T-H., Dong A., Meyer J., Johnson O., Cleland J., Carpenter J.: Use of infrared spectroscopy to assess secondary structure of human growth hormone within biodegradable microspheres. Journal of Pharmaceutical Sciences, **88**, 161–165 (2000). DOI: 10.1021/js980423n

[41] Arrieta A., Mera S., Diamant R., Fernández-Guasti M., Sosa R., Escobar-Alarcón L., Muñoz A. F., Haro-Poniatowski E.: Synthesis and characterization of sodium chloride thin films obtained by pulsed laser deposition. Applied Physics A: Materials Science and Processing, **69**, S491–S493 (1999). DOI: 10.1007/s003399900321

[42] Belu A., Mahoney C., Wormuth K.: Chemical imaging of drug eluting coatings: Combining surface analysis and confocal Raman microscopy. Journal of Controlled Release, **126**, 111–121 (2008). DOI: 10.1016/j.jconrel.2007.11.015

[43] Stevanović M., Ignjatović N., Jordović B., Uskoković D.: Stereological analysis of the poly-(DL-lactide-co-glycolide) submicron sphere prepared by solvent/non-solvent chemical methods and centrifugal processing. Journal of Materials Science: Materials in Medicine, **18**, 1339–1344 (2007). DOI: 10.1007/s10856-007-0156-8

[44] Chen H., Ding Y., Tan C.: Rheological behaviour of nanofluids. New Journal of Physics, **9**, 367/1–367/23 (2007). DOI: 10.1088/1367-2630/9/10/367

[45] Pukánszky B., Nagy T. T., Kelen T., Tüdős F.: Comparison of dynamic and static degradation of poly(vinyl chloride). Journal of Applied Polymer Science, **27**, 2615–2623 (1982). DOI: 10.1002/app.1982.070270730

eXPRESS Polymer Letters Vol.5, No.11 (2011) 1009–1016
Available online at www.expresspolymlett.com
DOI: 10.3144/expresspolymlett.2011.98

A novel test method for quantifying surface tack of polypropylene compound surfaces

U. D. Çakmak[1], *G. Grestenberger*[2*], *Z. Major*[1]

[1]Johannes Kepler University Linz, Institute of Polymer Product Engineering, Altenbergerstr. 69, 4040 Linz, Austria
[2]Borealis Polyolefine GmbH, Innovation Headquarters, St-Peterstraße 25, 4021 Linz, Austria

Received 1 April 2011; accepted in revised form 2 June 2011

Abstract. While adhesiveness is required for polymer surfaces in special applications, tacky surfaces are generally undesirable in many applications like automotive interior parts. The tackiness of polymer surface results from a combination of composition and additivation, and it can change significantly in natural or accelerated ageing. Since there is no established, uniform method to characterize surface tack, the major focus of the present work was on the development of an objective quantification method. A setup having a soft die tip attached to a standard tensile tester was developed aiming for correlation to the human sense of touch. Three different model thermoplastic polyolefin (TPO) compound formulations based on a high-impact isotactic polypropylene (iPP) composition with varying amounts and types of anti-scratch additives were used for these investigations. As the surface tack phenomenon is related to ageing and weathering, the material's examination was also performed after various intervals of weathering. The developed method allows a fast assessment of the effect of polymer composition variations and different additive formulations on surface tack and gives identical rankings as the standardized haptic panel.

Keywords: *material testing, industrial applications, surface tack, polypropylene, haptic properties*

1. Introduction

Due to their versatility and easy shaping properties, polymers have successively replaced classic materials such as wood and leather for automobile interiors since the middle of the last century. Especially thermoplastic polyolefin (TPO) compounds based on isotactic polypropylene (iPP) as matrix polymer are widely used as interior parts (e.g. instrument panels, pillar trims, door claddings) in the automotive industry. The property spectrum of this polymer class is very broad and can be tailored by varying the type and content of elastomers and fillers as well as the use of special additives [1–8]. The material can be adjusted to achieve desired properties with regard to the original part manufacturer (OEM) specifications, with the key material properties considered for interior applications illustrated in Figure 1.

The OEM specifications require a balanced mechanical performance in combination with a material

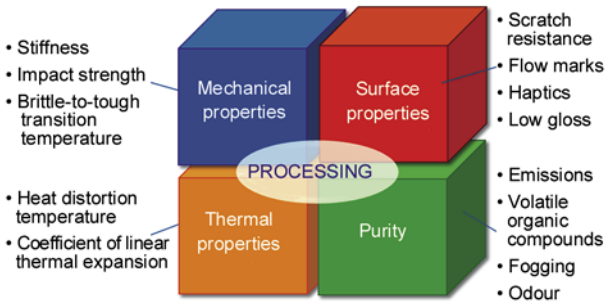

Figure 1. Illustration of the considered material specifications for plastics for automotive interior applications

*Corresponding author, e-mail: georg.grestenberger@borealisgroup.com

surface offering high scratch resistance, low gloss, and good 'surface feel' or haptics [9]. Haptic properties refer to the subjective surface impression during touching and qualitatively rank between completely non-tacky surfaces and tacky surfaces generally characterized by a high level of adhesiveness [10]. Although adhesiveness might be required in many applications, like adhesive tapes or notes, it is highly undesirable for automotive interior parts. In some cases, OEMs observed tackiness on part surfaces after weathering (elevated temperature and UV-irradiation, among other parameters) and assumed that the migration of incorporated additives is a main driver for this phenomenon. The migratory additives in TPO-compounds include antioxidants, UV-stabilizers, anti-scratch additives and mould release agents. Other possible sources of surface adhesion are amorphous low molecular weight fractions of the polymer composition itself [11].

A major concern around the surface tack phenomenon is the lack of an appropriate test method and standardized test equipment or methodology to characterize this important phenomenon. It can hardly be compared to tack measurements for adhesives [12, 13] because the respective tack forces are orders of magnitude lower than for e.g. for pressure-sensitive adhesives while the complex detachment phenomena like cavitation [14] will not play a role. For pure elastomers (like natural rubber) surface tack measurement is an established method and mostly related to the quantification of adhesive forces [10, 15] with short contact time measurements playing an important role [16, 17]. For polymers, such measurements have been developed for the film area [18] but rather with a focus on self-adhesion as desired for cling films. Rigid surfaces not subjected to a coating or painting process have mostly been neglected in this respect so far.

In the automotive area, OEMs and material suppliers have previously designed their own methods to assess tackiness. Most of these techniques make use of haptic reference scales or describe the corresponding sensory perception [9, 12, 19]. One example is the 'Sensotact tactile reference frame' (manufacturer: Cemas, Besançon, France). This reference scale consists of a set of ten descriptors, each made up of five reference parts in ascending order of sense of touch intensity. Each descriptor represents a different haptic sense. In this way, Sensotact distinguishes ten surface characteristics, which are determined according to specific finger movements – orthogonal or tangential – across the surface. To determine the tackiness of a surface, the index, middle, and ring fingers are lightly pressed onto the surface at an angle of about 15°. The resistance felt during the subsequent lifting of the fingers is regarded as a measure for tack [20]. Unfortunately, these methods generally lack reproducibility as they are based on testers' impressions of surface tack which are quite subjective, time-consuming and difficult to compare between laboratories.

An attempt to really quantify the tackiness of plastic surfaces was made by Huber and Solera [21] in adapting a film block tester normally used to determine the block strength or lubricity of plastic films. In order to assess the tackiness of artificially aged plates, low density polyethylene (LDPE) films were pressed onto the still-warm plates (30 min with a load of 5 kg). After a defined conditioning period, the films were peeled off with the block tester, and the adhesive force recorded. With this setup it could be shown that under corresponding UV radiation of the components, the decomposition products of erucamide resulted in higher film adhesion. No attempt was made to relate the measured forces to human perception, and the film block tester only permitted a differentiation of adhesive forces up to 21 N. All samples with higher values were classified as 'bad'. The target of the present study was therefore to develop a test setup and surface tack method suitable for the characterization of rigid surfaces typical for automotive interiors, the results of which should be related to those of a haptic panel, i.e. human perception. An important factor in designing the experiment should be a realistic contact time, avoiding both the very short contact typical for elastomer testing (0.1 s, see [17]) and the very long times for film block testing (30 min, see [21]).

2. Experimental work

2.1. Materials and specimen preparation

Three different model TPO-compound formulations based on a high-impact ethylene-propylene copolymer from sequential copolymerization in a reactor cascade [22] were used for these investigations. The compounds were formulated with varying amounts and types of slip agents to reduce

scratch sensitivity, while the other constituents (base resin, talc, antioxidants and UV-stabilizer) were kept constant. The base polymer was a commercial grade having a melt flow rate (melt flow rate (MFR) 230°C/2.16 kg, ISO 1133) of 18 g/10 min and a total ethylene content of 20 wt%, to which 11 wt% high density polyethylene (HDPE) (density 964 kg/m^3) and 17 wt% talc (Steamic T1CA, Luzenac, France) as well as a stabilization package and carbon black were added. One migratory additive, oleamide (Crodamide OR, Croda, Italy) at 0.15 wt% was compared to the neat material and a silicone (Tegomer Antiscratch 100, Evonik, Germany) as non-migratory additive at 2.0 wt%.

The stickiness test was performed on injection moulded 'VW' multigrain plaques (see Figure 2) with a film gate using the grain K29 to characterize the tackiness. The K29 surface is defined as a grain with a grain depth of 0.01 mm, and a minimum draft angle of 1° for ejection from the injection moulding tool [23]. The section with this grain was cut out from the plaque with a bench shear.

As the surface tack phenomenon is often considered as a consequence of weathering conditions, the material examination was performed after various intervals of weathering. The specimens were faced around a light source in an environmental chamber (WeatherOmeter Ci4000, Atlas Material Testing Technology GmbH; Linsengericht, Germany) and artificially weathered. The Kalahari weathering condition in dry and hot climate was performed, which is a well-known test in the automotive industry [24]. The weathering conditions of the chamber were:

– light source: Xenon arc light
– filter: Pyrex S
– black standard temperature: 90°C
– chamber temperature in the dry phase: 50°C
– relative humidity: 20%
– intensity of irradiation (300–400 nm): 75 W/m^2.

In the current investigation the specimens were irradiated for 24, 48, 96, 192, and 384 h. After the UV-exposure, the specimens were conditioned for approximately 1 h at 23°C and 50% relative humidity before testing surface tack.

2.2. Test setup and surface tack investigation

The requirements for an ideal surface tack measurement were summarized as follows:

– objective measured values instead of human impression
– reproducible and reliable results
– good correlation of test results to human impression of stickiness
– easy to implement on existing equipment
– short measurement times
– flexible in terms of pre-treatment.

After evaluation of different concepts a promising route was identified. The basic idea was to perform a compression-tensile test combination, where a die is first pressed vertically onto the specimen surface with a constant controlled force. After a holding time, the die is detracted at constant pull-off speed, recording the maximum force necessary to remove the die vertically as the surface tack force. This particular procedure of verifying stickiness is similar to the manual assessment according to the Sensotact haptic frame [20].

First of all, the material of the die tip had to be chosen for the further verification of the parameter influences. Since this material is in direct contact with the specimen surface, it should not contain any migrating constituents and have elasticity and softness comparable to a human finger. This should allow the material to adapt completely to a profiled

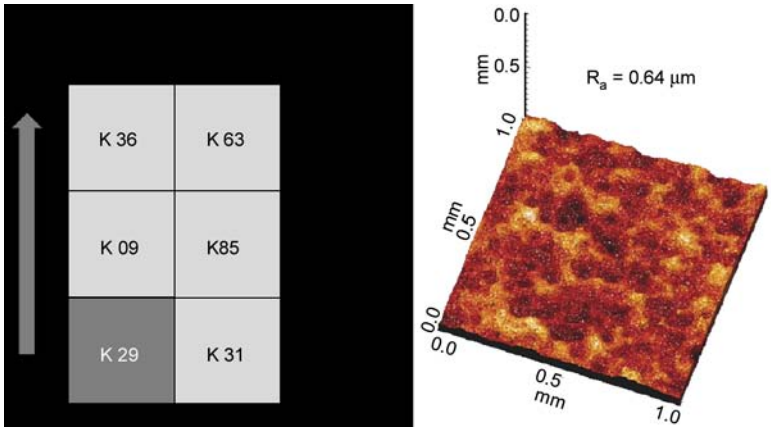

Figure 2. Schematic demonstration of the VW multigrain plaque and topography of the cut-out specimen K29

surface as typical for automotive interior components while not deforming plastically in the process. Furthermore, it should be easy to process and have good long-term availability. Several materials in a Shore A hardness range from 40 to 70 were screened and a natural rubber/styrene butadiene rubber (NR/SBR) blend (Semperflex A 560, Semperit Technische Produkte GmbH, Wimpassing, Austria; see [25]) was found to give the best balance between hardness (surface adaptation and 'finger-like' behaviour) and surface tack (no plastic deformation and enhanced adhesion).

An aluminium sheet was chosen as reference surface to be measured prior to each test. The influence of inherent engineering fluctuations of the die tip elastomer on the test result was minimized, and the reproducibility was increased by this procedure. Moreover, to reduce the possibility of transferring surface components from one specimen to another a new die was used for each specimen characterization.

For handling reasons, the elastomer was supplied with a separating agent on its surface which caused large fluctuations in the surface tack test results. In order to minimize the fluctuations, different cleaning conditions using either acetone or water were tested and the standard deviation was monitored. Each cleaning method had several test runs which were compared to a reference non-cleaned elastomer. The acetone cleaned die tips were tested both immediately after cleaning and after 24 h to verify if there was a change of the elastomer surface (swelling, acetone residuals etc.).

The mechanical properties of the die tip elastomer also change over its lifetime, and the die tip will not show the same behaviour after long time and/or high temperature in surface tack testing. This influence factor was eliminated by using a new elastomer die tip for each measurement, assuming the properties to remain constant for the short testing time window.

In principle, the test setup developed in the present study can be adapted to any tensile testing machine capable of handling the defined test parameters. Figure 3 shows a schematic picture of the setup and a photograph of the installation on the tensile tester. For the current investigations an Instron tensile testing machine (ElectroPuls E3000, Instron Deutschland GmbH; Darmstadt, DEU) was used to perform the experiments.

Each single surface tack measurement was performed with this setup in the following way: After the elastomer (NR/SBR) tip had been cleaned and attached to the die by means of a double-side adhesive tape, the tackiness force F_T of both the aluminium reference and the specimen (sample) were measured. Figure 4 shows an example of the force/displacement curve from a reference measurement on the aluminium plaque. The tack quotient Q_T was calculated by Equation (1):

$$Q_T = \frac{F_{T,\,sample}}{F_{T,\,reference}} \tag{1}$$

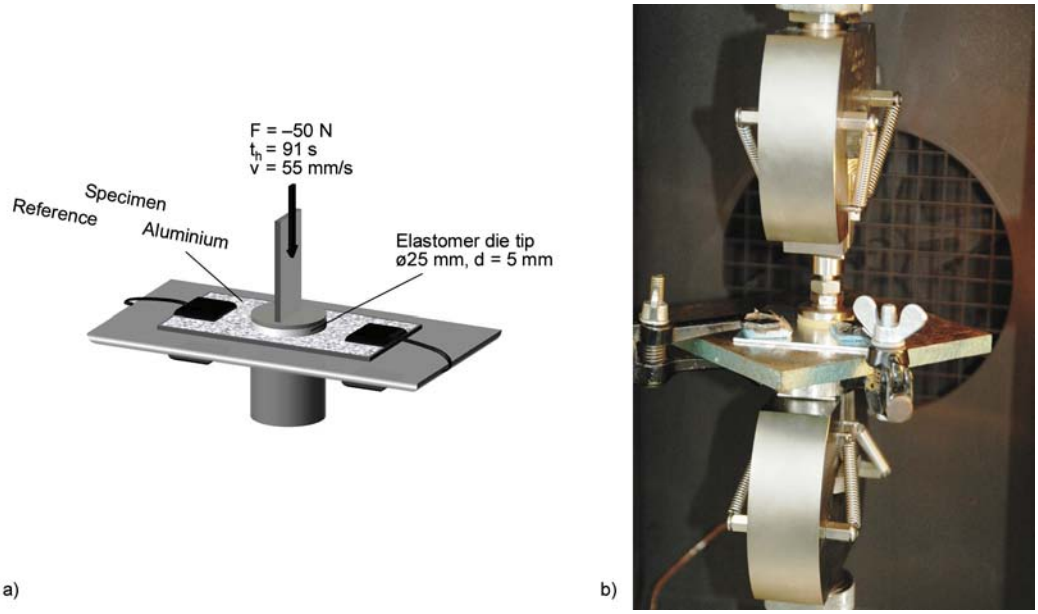

Figure 3. Schematic test setup (a) and photograph of real equipment (b) for surface tack measurements

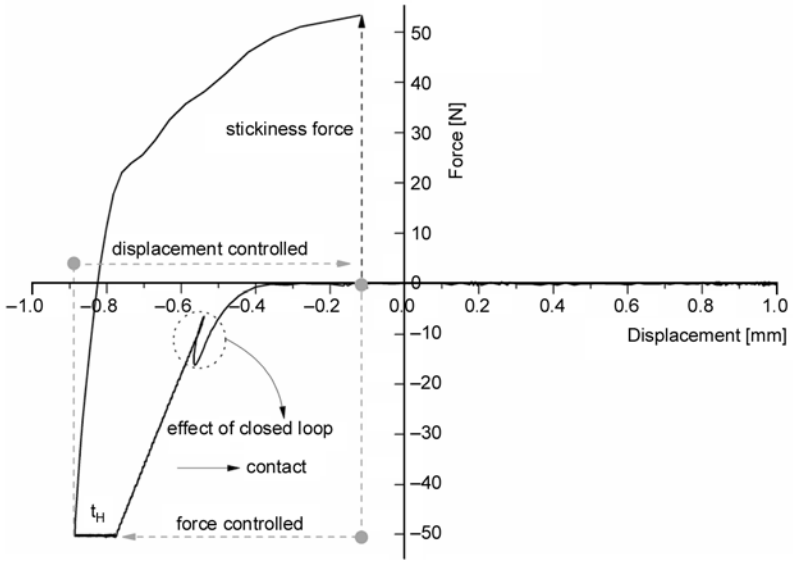

Figure 4. Force / displacement curve from the tack measurement process; the negative displacement shows the compression of the die tip elastomer (tested material: aluminum reference)

and averaged over a minimum of three successive measurements.

2.3. Test parameter selection and reference

The main parameters of the stickiness test are the compressive force (F), holding time (t_H) and haul-off speed (v). A number of other parameters such as environment and specimen clamping were not considered or kept constant during the test. The tests were performed at standard laboratory climate conditions (+23°C and 50% relative humidity). A design of experiments (DoE) was used to determine the effect of the main factors on the measurement, where for each factor two levels were selected.

A DoE with three factors and two levels (2^3) required eight experiments to analyze the significance and effect of each factor (see Table 1). The design of experiments was applied according to Montgomery [26]. The statistical analyses of variances (ANOVA) of the experimental results were examined and the significances of the factors were verified with the aid of the F-test (hypotheses test). The effect of a factor or an interaction (i.e. the combined impact of factors) is the difference in averages between the four treatment combinations at high level minus the average of the four runs where the factor or interaction is at the low level.

A haptic panel according to DIN 10963, which is equivalent to ISO 8587 (2007) [27], was organized as reference to verify if the human sense of touch is correlating to the results of the surface tack test. Consisting of about 30 persons of different ages and genders, the testers were trained using a Sensotact tactile frame [20] to assess and rank sticky surfaces and operated at identical environmental conditions as the mechanical test. The fact that the pH-value and the moisture of the testers' fingers also influence their sense of touch was not considered in the haptic panel, and the testers were only instructed to wash their hands. A separate specimen was prepared from each material for each test person. The results of the Friedman-Test show if the same specimens are ranked significantly different by the testers (general difference) and if pairs of specimens are significantly different.

Table 1. Tabulation of performed tests with different levels of the factors according to a 23 design of experiments; F – compressive force, t_H – holding time, v – haul-off speed

Number of tests	F [N]	t_H [s]	v [mm/s]
1	–5	1	10
10	–5	1	100
5	–5	180	10
7	–5	180	100
8	–50	1	10
6	–50	1	100
4	–50	180	10
2	–50	180	100

Table 2. Tack force quotient results from checking the influence of different cleaning conditions of the elastomer die tips

	Uncleaned	Water	Acetone	Acetone/24 h
Measurement 1	0.68	0.53	0.38	0.39
Measurement 2	0.47	0.37	0.41	0.36
Measurement 3	0.30	0.44	0.35	0.36
Q_T average	0.68	0.53	0.38	0.39
S.dev. Q_T	0.19	0.08	0.03	0.01

3. Results and discussion

3.1. Cleaning conditions and reproducibility

The tests performed to select the most appropriate die-tip cleaning conditions were also used to check the reproducibility of the surface tack test. Table 2 summarizes the results of the four series performed with different cleaning conditions, measuring the non-equipped TPO-compound. It shows the clear advantage of acetone as cleaning agent over water, and the rather negligible effect of a waiting period of 24 hours after cleaning, excluding the possible problem of swelling or interaction between acetone and the SBR material.

3.2. Parameter selection by DoE

After performing the test series indicated in Table 1 in randomized fashion and identifying both effect level and interaction of the three investigated parameters, it can be deduced that all main and interaction effects are significant for the response value (Q_T) and thus for the tackiness test. However, the factor F (compressive force) is clearly the most significant factor for the tackiness value. Since the significance of the factors t_H (holding time) and v (haul-off speed) is much lower, the standardized test parameters for the further investigations were defined as factor F at high level, t_H and v at the center level:

– compressive force, F = –50 N
– holding time, t_H = 91 s
– haul-off speed, v = 55 mm/s

The test is also illustrated in the force/displacement graph (see Figure 4), where the two phases of the tackiness test and the tackiness force evaluation are shown. The first phase is force controlled at –50 N until the holding time (91 s) runs off. During this phase, the die tip elastomer is creeping at constant force. In the second phase, which is displacement controlled (55 mm/s) the peak value in the force-displacement curve was reported as tackiness force, i.e. force needed to remove the die tip from the specimen's surface.

3.3. Composition effects and relation to haptic panel results

Figure 5 summarizes and compares the results from the mechanical tack quotient measurements and the haptic panel ranking for the three investigated compositions. While the correlation appears to be only a qualitative one, the relative ranking of surface tack between the newly developed test method and the established method based on individual human perception is clearly identical. It can therefore be assumed that relative changes in surface tack resulting from variations of polymer composition can be quantified or at least ranked reliably with the new method.

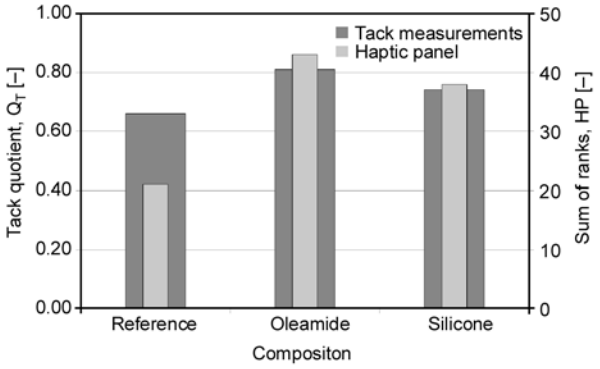

Figure 5. Comparison of results from tack force measurement and haptic panel for the three investigated TPO-compounds with different additivation

3.4. Weathering effects and time dependence

The fact that surface tack of polymer components change over times due to migration and ageing effects has been mentioned before. To compare the relative effects for the three investigated compositions, artificial ageing according to the Kalahari weathering conditions in dry and hot climate as defined above were performed. As Figure 6 shows, not only the absolute level of the individual compositions' surface tack, but even the relative ranking changed over time, pointing out the high importance of well defined sample preparation and pretreatment for achieving relevant results. The strong variations at short time for both the reference composition and the one containing the migratory additive (oleamide) probably result from a combination

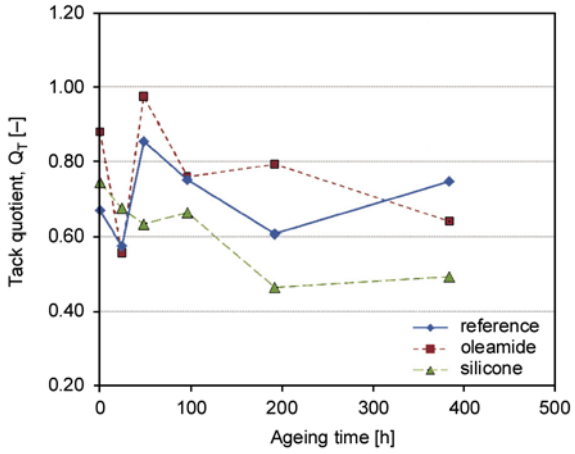

Figure 6. Effect of artificial weathering on the tackiness for the three investigated TPO-compounds with different additivation

of migration and subsequent decomposition of additives. This is in line with experience from haptic panel tests combined with ageing tests before.

4. Conclusions

In the present study it could be demonstrated that by means of corresponding development work in the area of measurement methods, it is possible to make very subjective sensory perceptions such as the haptic properties of a surface quantifiable. The key to success lies in breaking down complex sensory perceptions to the most important influencing factors. If this simplification is successful, it is possible to make deductions about the complex human sense of touch also if a very simple test setup is used.

The present results show the possibilities of the developed method, both in respect to comparing different material compositions qualitatively and even (semi-)quantitatively and in assessing the effect of artificial weathering on surface tack. In standard material development this provides a fast method for both assessing the effect of polymer composition variations and different additive formulations. For more complex variations (like massive changes of material mechanics) it will probably still be necessary to reference such results to human perception by involving haptic panel testing.

References

[1] Karger-Kocsis J., Csikai I.: Skin-core morphology and failure of injection-molded specimens of impact-modified polypropylene blends. Polymer Engineering and Science, **27**, 241–250 (1987). DOI: 10.1002/pen.760270403

[2] Alonso M., Gonzalez A., Requejo A., Arribas M., de Saja J. A.: Air-borne sound absorption and sound speed in talc-filled polypropylene. Polymer Testing, **11**, 71–78 (1992). DOI: 10.1016/0142-9418(92)90035-A

[3] Karger-Kocsis J.: Polypropylene: Structure, blends and composites. Vol. 2 – Copolymers and blends. Chapman and Hall, London (1995).

[4] Chu J., Xiang C., Sue H-J., Hollis R. D.: Scratch resistance of mineral-filled polypropylene materials. Polymer Engineering and Science, **40**, 944–955 (2000). DOI: 10.1002/pen.11222

[5] Xiang C., Sue H-J., Chu J., Coleman B.: Scratch behavior and material property relationship in polymers. Journal of Polymer Science Part B: Polymer Physics, **39**, 47–59 (2001). DOI: 10.1002/1099-0488(20010101)39:1<47::AID-POLB50>3.0.CO;2-2

[6] Pasquini N.: Polypropylene handbook. Hanser, Munich (2005).

[7] Koch T., Machl D.: Evaluation of scratch resistance in multiphase PP blends. Polymer Testing, **26**, 927–936 (2007). DOI: 10.1016/j.polymertesting.2007.06.006

[8] Markarian J.: Thermoplastic elastomer compounds continue upward trend. Plastics, Additives and Compounding, **10**, 38–43 (2008). DOI: 10.1016/S1464-391X(08)70186-7

[9] Dagman J., Karlsson M. A., Wikström L.: Investigating the haptic aspects of verbalised product experiences. International Journal of Design, **4**, 15–27 (2010).

[10] Hamed G. R., Shieh C-H.: Relationship between the cohesive strength and the tack of elastomers. Journal of Polymer Science: Polymer Physics Edition, **21**, 1415–1425 (1983). DOI: 10.1002/pol.1983.180210812

[11] Voyutskii S. S., Vakula V. L.: The role of diffusion phenomena in polymer-to-polymer adhesion. Journal of Applied Polymer Science, **7**, 475–491 (1963). DOI: 10.1002/app.1963.070070207

[12] Toyama M., Ito T., Moriguchi H.: Studies on tack of pressure–sensitive adhesive tapes. Journal of Applied Polymer Science, **14**, 2039–2048 (1970). DOI: 10.1002/app.1970.070140812

[13] Bates R.: Studies in the nature of adhesive tack. Journal of Applied Polymer Science, **20**, 2941–2954 (1976). DOI: 10.1002/app.1976.070201102

[14] Tirumkudulu M., Russel W. B., Huang T. J.: On the measurement of 'tack' for adhesives. Physics of Fluids, **15**, 1588–1605 (2003).
DOI: 10.1063/1.1571058

[15] Mith S., Carpentier L., Monteil G.: Correlation between the sensorial perception and the descriptive instrumental analysis of the tackiness of silicone elastomers. Surface and Interface Analysis, **40**, 142–145 (2008).
DOI: 10.1002/sia.2795

[16] David M. O., Nipithakul T., Nardin M., Schultz J., Suchiva K.: Influence of nonrubber constituents on tack of natural rubber. I. At very short times of contact (pendulum test). Journal of Applied Polymer Science, **78**, 1486–1494 (2000).
DOI: 10.1002/1097-4628(20001121)78:8<1486::AID-APP40>3.0.CO;2-I

[17] Smitthipong W., Nardin M., Schultz J., Niphithakul T., Suchiva K.: Study of tack properties of uncrosslinked natural rubber. Journal of Adhesion Science and Technology, **18**, 1449–1463 (2004).
DOI: 10.1163/1568561042323248

[18] McNally G. M., Small C. M., Murphy W. R., Garrett G.: The effect of polymer properties on the mechanical behavior and morphological characteristics of cast polyethylene film for stretch and cling film applications. Journal of Plastic Film and Sheeting, **21**, 39–54 (2005).
DOI: 10.1177/8756087905052804

[19] Chen X., Shao F., Barnes C., Childs T., Henson B.: Exploring relationships between touch perception and surface physical properties. International Journal of Design, **3**, 67–77 (2009).

[20] Legay F.: The first tactile reference frame. Company magazine of CEMAS (Centre of Microtechniques Evaluation dedicated to Sensory Analysis), Besançon (2010).
http://www.sensotact.com

[21] Huber G., Solera P.: New additive to improve scratch resistance and reduce surface tack for automotive applications. in 'Proceedings of the 1st World Automotive Congress-Plastics in Motion, Lisbon, Portugal' p.15 (2006).

[22] Schwager H.: PP reactor blends. in 'Polypropylene '92 World Congress, Zürich, Switzerland' pp. II-4.1–II-4.18 (1992).

[23] Eschmann Textures International GmbH: Texture guide- Get in touch. P.19 (2010).
http://www.eschmanntextures.de/fileadmin/user_upload/downloads/guide/Textures_Guide_en.pdf

[24] Riedl A.: Überblick über die Methoden der Bewitterungs- und Lichtechtheitsprüfung in der Automobilindustrie (in German). Galvanotechnik, **97**, 420–427 (2006).

[25] Semperit Technische Produkte GmbH: Semperflex A560, Data sheet (2010).
http://www.semperflex.com/uploads/tx_AScatalog/files/A560_e.pdf

[26] Montgomery D. C.: Design and analysis of experiments. Wiley, New York (1991).

[27] ISO 8587: Sensory analysis – Methodology – Ranking (2007).

eXPRESS Polymer Letters Vol.5, No.11 (2011) 1017–1026
Available online at www.expresspolymlett.com
DOI: 10.3144/expresspolymlett.2011.99

Facile preparation of rich β-transcrystallinity in PET fiber/iPP composites

X. Q. Hao[1], *G. Q. Zheng*[1,2*], *K. Dai*[1], *Z. H. Jia*[1], *Q. Jia*[1], *J. B. Chen*[1], *C. T. Liu*[1], *C. Y. Shen*[1]

[1]College of Materials Science and Engineering, The Key Laboratory of Material Processing and Mold of Ministry of Education, Zhengzhou University, Zhengzhou, 450002, P.R. China
[2]The Key Laboratory of Polymer Processing Engineering, Ministry of Education, Guangzhou, 510641, P.R. China

Received 16 February 2011; accepted in revised form 7 June 2011

Abstract. Polyethylene terephthalate (PET) fibers containing different contents of β-nucleating agent (β-NA) were melt-spun from a reconstructive melt flow index rheometer at 270°C, and then blended with polypropylene (iPP). The supermolecular and phase structure of the composite were investigated by polarized optical microscopy (POM), differential scanning calorimetry (DSC), and wide-angle X-ray diffraction (WAXD). For the pure PET fiber reinforced iPP, the interfacial region was mainly composed of α-modification, though it has been demonstrated that PET fiber shows weak nucleating ability towards iPP matrix. More interestingly, when the amount of β-NA introduced into the PET fiber exceeds a critical value, the transcrystalline layer will be notably dominated by β-modification. This method to prepare β-transcrystallinity is remarkably different from those through stress or temperature control. The present results provide a facile and promising technique to prepare rich β-transcrystallinity under stress-free conditions.

Keywords: *polymer composites, PET fiber, β-transcrystallinity, dendritic structure, self-organization*

1. Introduction

It is well known that when fibers are introduced into a semi-crystalline polymer matrix, the matrix may be nucleated and fascinating crystalline morphology with various features will be developed at the interface. Such distinct morphology is defined as transcrystalline layer or transcrystallinity. This structure is always considered as an effective and economical method to improve interfacial adhesion [1–5].

Owing to the outstanding properties of β-iPP (e.g. better impact resistance and toughness) [6–11], β-crystallinty has attracted much attention in the past decades. Among them, β-transcrystallinity of iPP reinforced by fibers is particularly interesting. However, as for fiber/iPP composites, a number of studies have demonstrated that their interfacial morphology is mainly composed of α-transcrystallinity. Up to now, a few special approaches such as pulling fiber in iPP melt [12–14] and controlling the fiber's introduction temperature [15–17], have been proposed to prepare β-transcrystallinity. Recently, β-NA was even chemically supported onto the surface of multi-wall carbon nanotubes by Wang *et al*. [18]. The results indicate that the multi-wall carbon nanotubes after being supported with β-NA show enhanced β-nucleating ability towards iPP matrix. Except for the methods mentioned above, few approaches have been reported by which the β-transcrystallinity in fiber/iPP composites can be directly formed under static conditions.

Rare earth β-NA (WBG- II) exhibits considerable β-selectivity and nucleating efficiency to induce β-iPP [19, 20]. There exist two crucial problems about the addition of β-NA: first, for directly mixed β-NA/iPP system, comparatively large amount of β-

*Corresponding author, e-mail: gqzheng@zzu.edu.cn

NA is needed; the second is that, owing to the addition of mass β-NA, the polymer composite's processability would be weakened. In view of these, a problem naturally arises: how to develop abundant β-modification on the premise that the extremely small content of β-NA is added. However, to the best of our knowledge, there are scarcely studies concerning: (1) rich β-transcrystallinity developed directly in PET fiber/iPP system under static condition and (2) the effect of the fraction of additive introduced into PET fibers on the crystalline modifications at the interface.

Owing to its scientific interest and industrial significance [21], in this study, we will focus on a facile method by which rich β-transcrystallinity can be created under quiescent condition. Inspired by work of Dai *et al*. [22], β-NA with different contents was first melt mixed with PET pellets, and then PET fiber containing β-NA was prepared via melt spinning. The spun PET fibers were introduced into iPP melt to get PET fiber/iPP composites. The crystalline morphology at the polymer composites' interface was investigated in detail by POM, DSC as well as WAXD. This study could provide an effective way to fabricate rich β-transcrystallinity in PET/iPP composites in the absence of stress and temperature control.

2. Experimental

2.1. Materials

The iPP (T30S) used in this work is a commercial product from Lanzhou Petroleum Chemical Co., China. Its melt flow rate (MFR) is 2.6 g/10 min (230˚C, 2.16 kg), and is ca. $11.0 \cdot 10^4$ g/mol. The PET pellet, which is blow molding grade with an intrinsic viscosity of 0.65 dl/g, was purchased from Liaoyang Petroleum Chemical Co., China.

The β-NA (WGB-II), a heteronuclear bimetal complex of lanthanum and calcium with some specific ligands, was kindly provided by Winner Functional Materials Co. Ltd., China. It is an organic complex synthesized by rare earth elements and organic compounds (other information about this β-NA is available in the Supplement Material) [23]. Note that this kind of β-NA exhibits considerably β-selectivity and efficiency.

2.2. Sample preparation

To achieve a good dispersion of β-NA, WGB-II with different content (0.5, 1, 1.5, 2 wt%) was mixed with PET pellets in a Haake internal mixer (Haake Polylab System-Rheomex 252p series, RC9000, Haake company, Germany) at 270°C, for 5 min. Pure PET pellets were also treated under the same conditions. After crushing and drying, the fibers containing β-NA (fibers' diameter is about 40 μm) were melt-spun by a reconstructive melt flow index rheometer (RL-5, Shanghai S.R.D. Scientific Instrument Company, Shanghai, China) at 270°C with a take-up speed of 3 m/min. In a convenient manner, the as-spun PET fiber is labeled as x-PET, where x represents the mass percentage of β-NA. Hereafter, its corresponding composite is labeled as x-PET/iPP. The schematic illustration of PET fiber preparation is shown in Figure 1.

PET fiber/iPP composites were prepared as follows: for the POM experiment, a given amount of iPP was put on a coverslip of a Linkam TMS 600 hot stage with a preset temperature of 200°C, and then a single PET fibe was introduced into the iPP melt (Figure 1). Subsequently, another coverslip was put on and a film with a thickness of about 20 μm was formed under the press of tweezers; For DSC and WAXD experiments, 5 wt% PET fibers and 95 wt% iPP were mixed in a Haake internal mixer (Haake Polylab System-Rheomex 252p series, RC9000, Haake company, Germany) at 200°C, for 5 min. The sample preparing procedure is shown in Figure 1. It is noteworthy that, before iPP was melt blended with PET fibers, PET fibers had been cut into short fibers with a length of ca. 5 mm. In addition, the selection of 5 wt.% PET fibers in the composites has an important purpose: because of a smaller amount of β-transcrystallinity existing in single fiber reinforced composites, β-transcrystallinity might not be detected by WAXD and DSC. Therefore, 5 wt% PET fibers were introduced into iPP matrix to fabricate abundant β-transcrystallinity which can be detected easily by DSC and WAXD.

2.3. Characterization

2.3.1. POM

The polymer composites were held at 200°C for 5 min on a Linkam hot stage (TMS600) to remove

the stress involved during sample preparation, and then cooled to room temperature at a cooling rate of 10°C/min. The morphological observation during cooling was carried out with a POM (Olympus BX61, Olympus Corporation, Japan). The fabrication procedure of the sample is illustrated in Figure 1(a composites).

2.3.2. DSC

Thermal analysis was performed on a DSC (TA DSC-2920, TA Instruments, USA). About 5~10 mg composite was sealed into an aluminum pan, heated from room temperature to 200°C at a heating rate of 10°C /min and held for 5 min in order to erase the effect of thermal and mechanical history. Since β-iPP samples cooled down below $T(\alpha\beta)$ = 100°C can recrystallize into the α-modification during the partial melting of the α-phase, the end temperature of cooling (T_R) was set at 100°C. This limited recooling technique prevents βα-recrystallisation [11, 24, 25]. Then the samples were cooled to 100°C at a rate of 10°C/min. After that, they were heated to 200°C at a heating rate of 10°C/min. The DSC experiment has the same thermal process as POM.

2.3.3. WAXD

WAXD measurements were carried out on a Philips X'Pert Graphics and Indentify instrument (X'Pert PRO, PANalytical B.V., Netherlands) operating at 50 kV and 30 mA with Ni-filtered Cu K_α radiation source. The composite film for WAXD test composed 5 wt% PET fibers and 95 wt% iPP and its preparing procedure is also displayed in Figure 1(b composites). Note that it was thermally treated under the same conditions as those for POM and DSC measurements. Clearly, although the proportion of β-NA in PET fibers is between 0–2 wt%, but the proportion of PET fibers in the composite is just 5 wt%, so the proportion of β-NA in the composite is just 0–0.1 wt%, which is a much smaller than that of iPP.

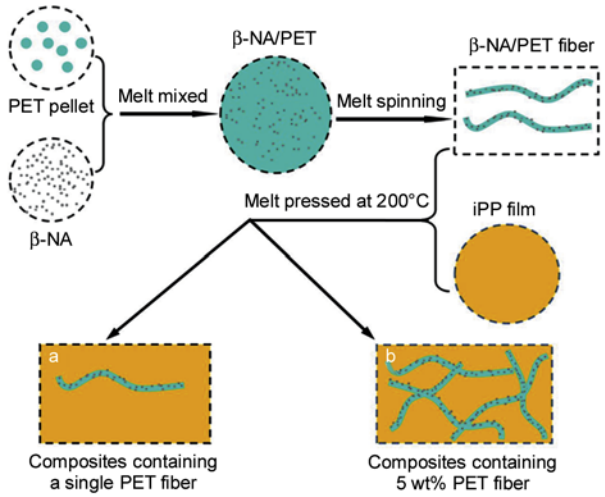

Figure 1. Schematic illustration of the preparation of PET fiber/iPP composites for characterization

2.2.4. Scanning electron microscope (SEM)

The surface morphology of PET fiber was observed by a scanning electron microscopy (SEM, Quonxe-2000, Phillips, FEI company, Netherlands) operating with an acceleration voltage of 20 kV. All the samples were sputtered with gold before taking images.

3. Results and discussion

3.1. The effect of β-NA loaded in PET fiber on the interfacial morphology

The formation of the transcrystalline layer, originated by fiber surface, is generally studied by single fiber model composites. In this study, the samples were crystallized under non-isothermal conditions after the erasure of thermal and mechanical history. Figure 2a shows a series of optical micrographs for 0-PET/iPP taken at three representative crystallization stages (i.e., the beginning, medium, and the end) during the cooling process. It can be clearly seen that once the temperature decreases to ca. 128°C, dense transcrystallinity immediately appears on PET fibers' surface. Simultaneously, dot-like nuclei are developed in the iPP matrix. With further decreasing temperature, the crystallites grow from these nuclei until they impinge on each other and a well developed transcrystalline layer can be obtained along the PET fibers. According to the birefringence of the crystals, it suggested that the crystallites in the matrix and those on the surface of PET fiber are of the same crystalline form. For the sample in which smaller amount of β-NA was added (0.5-PET/iPP), its matrix and interfacial feature is strongly analogous to that of 0-PET/iPP (see Figure 2b), indicating that low content of β-NA loaded in PET fiber is not enough to change the interfacial morphology. Furthermore, this also confirmed that the PET fiber used in this study shows obvious heterogeneous nucleating ability toward iPP.

Figure 2c–e shows the series of optical micrographs of 1-PET/iPP, 1.5-PET/iPP and 2-PET/iPP, respectively. It is very interesting that when the samples were cooled down to ca. 135°C, many characteristic dendritic structures first appeared randomly on the lateral surface of PET fibers (see Figure 2c–e), and

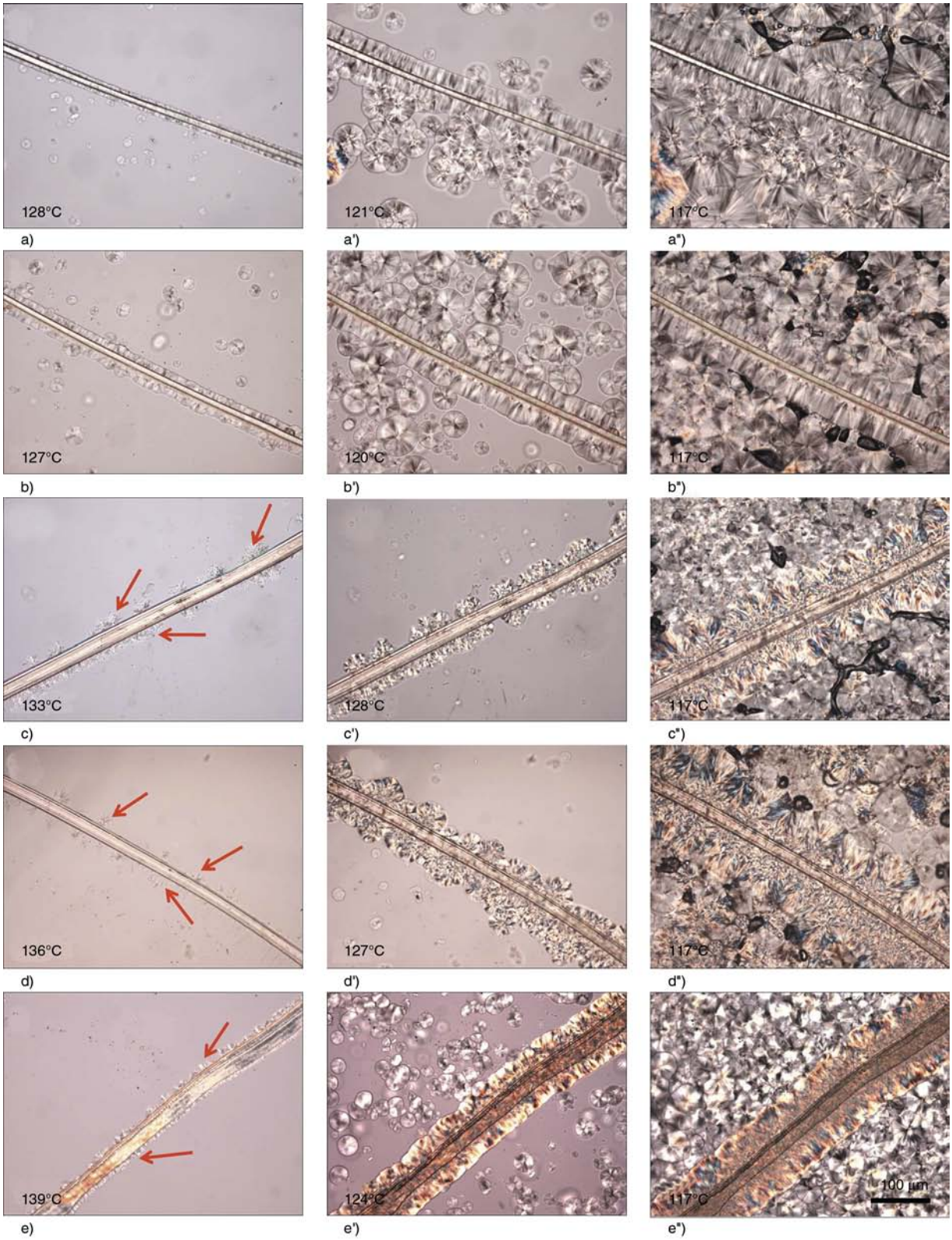

Figure 2. A series of optical micrographs of the PET fiber/iPP composites taken at different temperatures during the cooling process: (a) 0-PET/iPP; (b) 0.5-PET/iPP; (c) 1-PET/iPP; (d) 1.5-PET/iPP; (e) 2-PET/iPP. Temperature decreases from the left image to the right one.

the dendritic structures grew quickly with decreasing temperature. Compared with the crystals that emerged surrounding the PET fiber in 0-PET/iPP and 0.5-PET/iPP, the temperature at which the dendritic structures appeared is higher than that for 0-PET/iPP and 0.5-PET/iPP systems. Varga and Menyhárd [9] has also found the similar structure when they study the solubility and nucleating duality of N, N′-Dicyclohexyl-2, 6-naphthalenedicarboxamide (NJS) in iPP matrix. The formation of dendritic structures can be explained as follows: the β-NA can be partially molten at higher temperature, and then dendritic structures (i.e. nuclei) can be developed through high level of self-organization during cooling process.

Furthermore, as the temperature further decreases to 128°C, nuclei in bulk begin to appear sporadically. Thus taking into account above results, the β-NA filled PET fiber shows strong heterogeneous nucleating ability toward iPP at the interface of the composite. Moreover, when the samples' temperature further decreased to 123°C, the closely packed dendritic structures around the PET fiber caused the formation of transcrystallinity due to the limitation from the neighboring crystallites. Simultaneously, the bulk is still not fully occupied by the growing spherulites in matrix. This crystallization process is not completed until the sample is cooled to 116°C. It is worth noting that the spherulites in the bulk and the transcrystallinity are not of the same birefringence, suggesting that they are of different crystalline modifications.

To clarify what kind of crystalline forms are present in both the bulk and transtrystalline layers, these completely crystallized samples were heated to 158°C (this temperature is above the melting point of β-iPP but below that of α-iPP) at a rate of 10 °C/min. Figure 3 shows the optical micrographs of the composites after selective melting at 158°C.

In Figure 3a and b, it is evident that neither the spherulites nor the transcrystalline layer in 0-PET/iPP and 0.5-PET/iPP exhibit any change. More interestingly, as shown in Figure 3c–e, transcrystallinity in 1-PET/iPP, 1.5-PET/iPP and 2-PET/iPP significantly disappeared, resulting in the occurrence of sporadic fragmentary nuclei in the area near the surface of the PET fiber (shown by the arrows). Additionally, the spherulites in the matrix and the dendrites on the fibers' surface still exist. The selective melting test preliminarily confirms that the crystalline column surrounding the PET fiber in 0-PET/iPP and 0.5-PET/iPP is α-transcrystallinity, while that for 1-PET/iPP, 1.5-PET/iPP and 2-PET/iPP is β-transcrystallinity. During the crystallization process, the β-iPP grew faster and thus hindered the expansion of α front in the later stage of the crystallization. As a consequence,the transcrystallization formed in 1-PET/iPP, 1.5-PET/iPP and 2-PET/iPP were all β-modification. Dendrites have mixed polymorphic composite can be proved by presence of α-

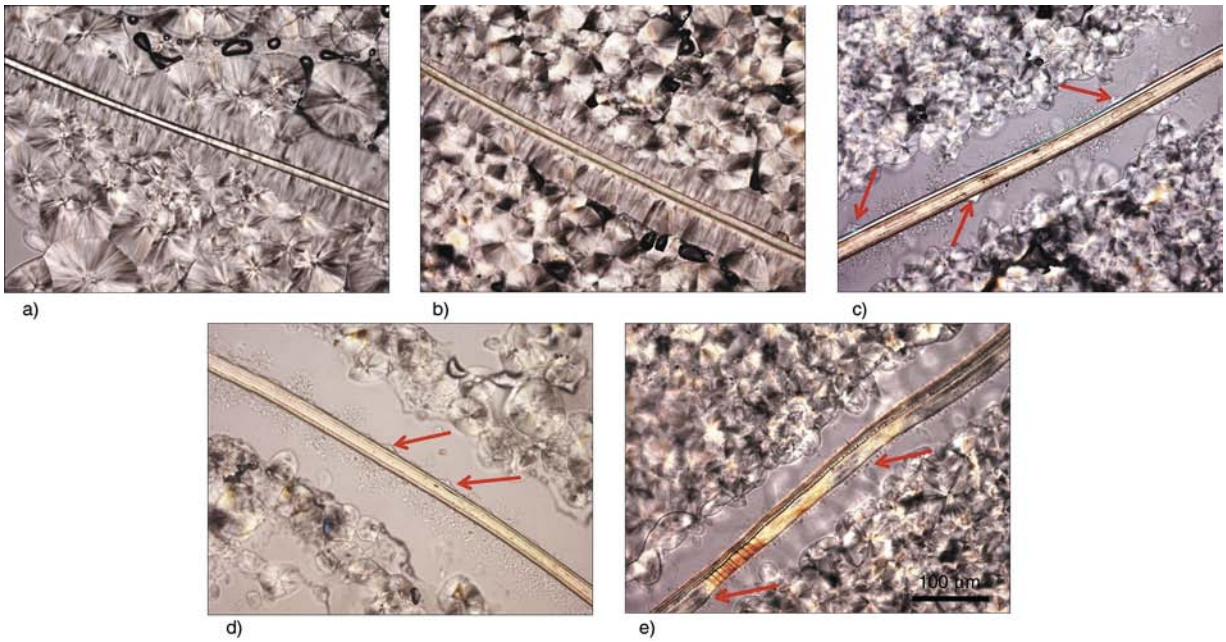

Figure 3. The optical micrographs of the samples after selective melting at 158°C: (a) 0-PET/iPP; (b) 0.5-PET/iPP; (c) 1-PET/iPP; (d) 1.5-PET/iPP; (e) 2-PET/iPP

crystallities left behind by the separate melting of β-modification.

To further verify the crystalline form of the transcrystallinity, WAXD measurement was carried out. Because of a smaller amount of β-transcrystallinity existing in single fiber reinforced composites, β-transcrystallinity might not be easily detected by WAXD and DSC. Therefore, 5 wt% PET fibers were introduced into iPP matrix to fabricate abundant β-transcrystallinity which can be detected easily by DSC and WAXD. Figure 4 shows the WAXD result of the selected composites. Generally, for all samples, three apparent α-crystal diffraction peaks appear at around 14.2, 16.9, and 18.7°, which correspond to α (110), α (040), and α (130), respectively. Furthermore, for 1-PET/iPP and 2-PET/iPP, it is obvious that there is an intense diffraction peak at approximately 16.1°, which corresponds to the β (300) reflection of β-crystal [26]. It indicates that a certain amount of β-modification was generated in these composites. However, as the case of 0.5-PET/iPP, there exists a very small β (300) diffraction peak at 16.1°, indicating that an extremely small content of β-form crystal was formed in this composite. Furthermore, any evidence of β-modification can not be found in WAXD results of 0-PET/iPP. Clearly, the WAXD result proves that β-NA loaded in the PET fibers can induce the formation of β-transcrystallinity. In addition, with the increasing content of β-NA loaded in PET fibers, the intensity of the reflection of β (300) increases.

To gain deeper insight into the effect of β-NA loaded in PET fiber on non-isothermal crystallization of the composites, the crystallization and melting characteristics of the composites were studied by DSC (details of the sample preparation and experimental procedures were described in Experimental Section). Figure 5 shows the DSC heating curves of all the samples. For the curves of 0-PET/iPP and 0.5-PET/iPP, there is only one melting peak at 166.2°C, revealing that α-crystal is dominated in these composites. However, for 1-PET/iPP, 1.5-PET/iPP and 2-PET/iPP, there exist double melting peaks, which are caused by different types of nucleation. The peak at the higher temperature (ca. 166.2°C) is evidently α-melting peak, and the other at the lower temperature (ca.152°C) is attributed to the melting of β-crystal. Once more, this result indicates that the β-NA in the PET fiber exhibits strong nucleating ability towards iPP matrix and leads to abundant β-modification, which is consistent well with the POM and WAXD results.

The non-isothermal crystallization curves are shown in Figure 6. One can observe that the onset crystallization temperature generally increases with the increasing content of β-NA loaded in PET fiber. For example, the onset temperature for 0-PET/iPP is ca.127°C, and that for 0.5-PET/iPP is a little higher

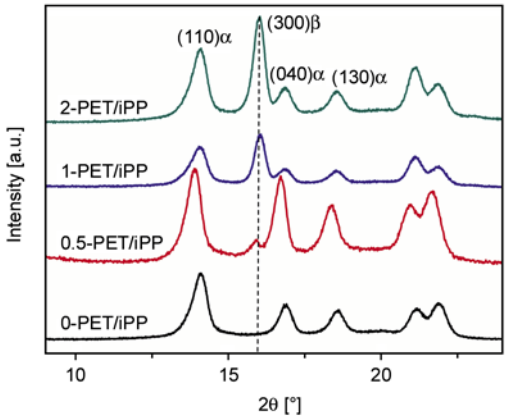

Figure 4. WAXD spectra of 0-PET/iPP, 0.5-PET/iPP, 1-PET/iPP and 2-PET/iPP composite samples

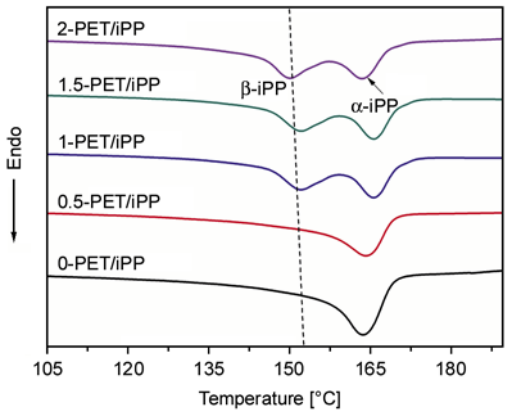

Figure 5. DSC melting curves of all the composites at a heating rate of 10°C/min

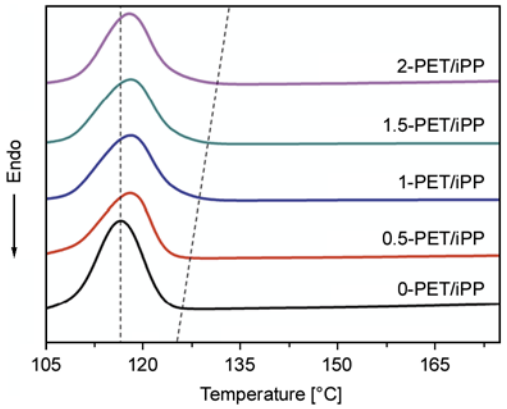

Figure 6. DSC cooling curves of all the composites at a cooling rate of 10°C/min

(ca. 128°C). However, onset temperatures for 1-PET/iPP, 1.5-PET/iPP and 2-PET/iPP are obviously above 130°C. In addition, it can be clearly seen that the crystallization peak temperature for 0-PET/iPP is ca. 116°C, but that for the other four samples are ca.118°C. Clearly, the increased onset crystallization temperature and crystallization peak temperature are related to the elevating content of the β-NA filled in PET fiber.

3.2. The mechanism for the formation of β-transcrystallinity in the presence of β-NA filled in PET fiber

It is scientifically and technologically significant to understand the origin of β-transcrystallinity in the presence of β-NA loaded in PET fiber. From the above experimental results, it is evident that the occurrence of β-transcrystallinity is undoubtedly related to the β-NA loaded in the PET fiber. More importantly, there is a critical content of β-NA required (i.e., 1 wt%) for the development of β-transcrystallinity. In other words, only the β-NA content exceeds this critical value, a certain amount of β-NA can be distributed on the surface of the PET fiber. Thus, the surface of the as-spun PET fibers with excessive β-NA content (take those containing 1 and 2 wt% as examples) were investigated by SEM, and the results are shown in Figure 7. In order to avoid the surface damage, no etching procedure was adopted. One observes that many aggregations of β-NA regularly distributed on the surface of the as-spun PET fiber containing 1 wt% β-NA (shown by arrows in Figure 7a). Furthermore, as shown by Figure 7a', numerous aggregations with smaller size are also distributed on the surface of PET fiber (shown by arrows). For the case of the PET fiber containing 2 wt% β-NA, although isolated aggregations of β-NA can be found on the surface of the as-spun PET fiber (shown by the arrows in Figure 7b), much larger aggregation (shown by circle) can be also observed due to the excessive β-NA added. More interestingly, the larger aggregation consists of many oval-shaped entities with uniform size (shown by the arrows in Figure 7b'). The SEM result indicates that β-NA can distribute on the surface of PET fiber after being spun.

Note that this kind of β-NA has modest solubility at 200°C, and can self-assemble into anisotropic entities during cooling [27]. Therefore, the aggregations in the region near PET fibers surface (shown in Figure 7) are a result of self-organization of partially molten β-NA during cooling process. In addi-

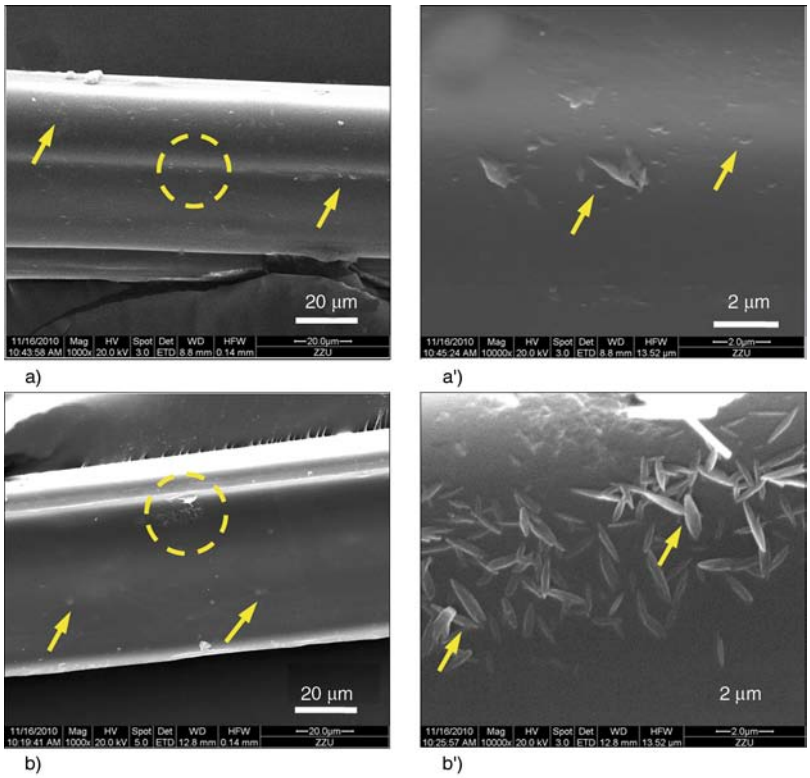

Figure 7. SEM images showing the surface of as-spun PET fiber containing different contents of β-NA. (a) 1 wt%; (b) 2 wt%; (a') and (b') are enlarged images of the cricle area in (a) and (b), respectively.

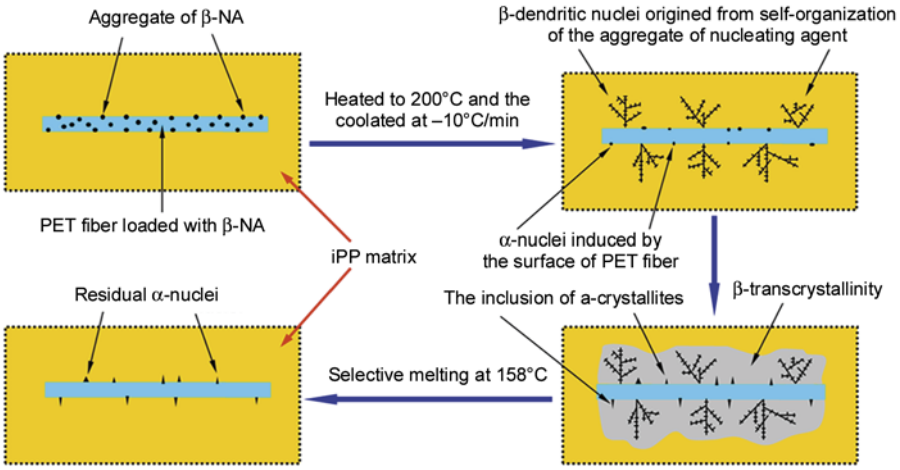

Figure 8. Schematic illustration of the interfacial morphology evolution of iPP reinforced by PET fiber loaded with β-NA and that after being selective melting

tion, during the process of self-organization, the β-NA loaded in PET fiber would go into the iPP component through such self-organization process and form dendritic structures [28]. Combined with the SEM images in this study, β-transcrystallinity can be understood as follows: during POM observation, when the composites were heated to 200°C and held for 5 min, β-NA decorated on the PET fiber can be molten partially. During cooling, molten β-NA would self-assemble into a more complicated dendritic structures which nucleates the subsequent β-transcrystallinity into the branch-like agglomerate (Figure 2c, 2d and 2e) [9, 27].

Another interesting thing is that, after selective melting, many dot-like α-nuclei appear on the surface of the fibers loaded with excessive β-NA (shown in Figure 3). It is well known that PET fiber can provide α-nucleating sites for iPP [16], which is also demonstrated in our study (see Figure 2a). Therefore, the PET fiber containing higher content of β-NA has dual nucleation ability, viz., it has both β nucleating ability and α nucleating ability. It is logical that the β-NA loaded in the PET fiber would lead to dense β-nuclei and enhance the growth of β-transcrystallinity, while the local surface without β-NA of the fiber induce the formation of α crystallites. Accordingly, such interfacial morphology evolution and that after selective melting in samples containing larger amount of β-NA can be schematically shown in Figure 8.

4. Conclusions

The effect of β-NA loaded in the PET fibers on the crystal morphology at the interface and in the bulk was investigated by POM, DSC and WAXD. The result shows, for 0-PET/iPP and 0.5-PET/iPP, the crystals in both iPP matrix and those at the interface are α-phase. Furthermore, nuclei in the two areas appear at the same time. For 0.5-PET/iPP, though it has a small fraction of β-NA in the PET fiber, there is rarely β-NA on the lateral surface of the fiber, so it is hard to induce β-transcrystallinity. However, for 1-PET/iPP, 1.5-PET/iPP and 2-PET/iPP, the nuclei surrounding the fiber occur earlier than that in the matrix, indicating that β-NA loaded in the PET fiber shows heterogeneous nucleation towards iPP matrix. Furthermore, if the content of β-NA exceeds a critical value (i.e., 1 wt%), the PET fiber loading β-NA shows nucleating duality. Meanwhile, the PET fiber loaded the content of β-NA above the critical value will show nucleating durability.

Acknowledgements

We would like to express our sincere thanks to NSFC (Grant: 50803060, 10872186, and 10872185) and the opening project of the key laboratory of polymer processing engineering, ministry of education of China.

References

[1] Tregub A., Harel H., Marom G., Migliaresi C.: The influence of thermal history on the mechanical properties of poly(ether ether ketone) matrix composite materials. Composites Science and Technology, **48**, 185–190 (1993).
DOI: 10.1016/0266-3538(93)90135-4

[2] Yue C. Y., Cheung W. L.: Interfacial properties of fibrous composites. Part II Determination of interfacial shear strength, interfacial coefficient of friction, and the shrinkage pressure on the fibre. Journal of Materials Science, **27**, 3181–3191 (1992).
DOI: 10.1007/BF01116008

[3] Nagae S., Otsuka Y., Nishida M., Shimizu T., Takeda T., Yumitori S.: Transcrystallization at glass fibre/polypropylene interface and its effect on the improvement of mechanical properties of the composites. Journal of Materials Science Letters, **14**, 1234–1236 (1995).
DOI: 10.1007/BF00291816

[4] Saujanya C., Radhakrishnan S.: Development of a transcrystalline phase in poly(propylene) at the PET interface. Macromolecular Materials and Engineering, **286**, 1–4 (2001).
DOI: 10.1002/1439-2054(20010101)286:1<1::AID-MAME1>3.0.CO;2-U

[5] Kitayama T., Utsumi S., Hamada H., Nishino T., Kikutani T., Ito H.: Interfacial properties of PP/PP composites. Journal of Applied Polymer Science, **88**, 2875–2883 (2003).
DOI: 10.1002/app.11805

[6] Kotek J., Raab M., Baldrian J., Grellmann W.: The effect of specific β-nucleation on morphology and mechanical behavior of isotactic polypropylene. Journal of Applied Polymer Science, **85**, 1174–1184 (2002).
DOI: 10.1002/app.10701

[7] Chen H. B., Karger-Kocsis J., Wu J. S., Varga J.: Fracture toughness of α- and β-phase polypropylene homopolymers and random- and block-copolymers. Polymer, **43**, 6505–6514 (2002).
DOI: 10.1016/S0032-3861(02)00590-6

[8] Chvátalová L., Navrátilová J., Čermák R., Raab M., Obadal M.: Joint effects of molecular structure and processing history on specific nucleation of isotactic polypropylene. Macromolecules, **42**, 7413–7417 (2009).
DOI: 10.1021/ma9005878

[9] Varga J., Menyhárd A.: Effect of solubility and nucleating duality of *N,N′*-dicyclohexyl-2,6-naphthalenedicarboxamide on the supermolecular structure of isotactic polypropylene. Macromolecules, **40**, 2422–2431 (2007).
DOI: 10.1021/ma062815j

[10] Lovinger A. J., Chua J. O., Gryte C. C.: Studies on the α and β forms of isotactic polypropylene by crystallization in a temperature gradient. Journal of Polymer Science: Polymer Physics Edition, **15**, 641–656 (1977).
DOI: 10.1002/pol.1977.180150405

[11] Varga J.: β-modification of isotactic polypropylene: Preparation, structure, processing, properties, and application. Journal of Macromolecular Science Part B: Physics, **41**, 1121–1171 (2002).
DOI: 10.1081/MB-120013089

[12] Varga J., Karger-Kocsis J.: Interfacial morphologies in carbon fibre-reinforced polypropylene microcomposites. Polymer, **36**, 4877–4881 (1995).
DOI: 10.1016/0032-3861(95)99305-E

[13] Jay F., Haudin J. M., Monasse B.: Shear-induced crystallization of polypropylenes: Effect of molecular weight. Journal of Materials Science, **34**, 2089–2102 (1999).
DOI: 10.1023/A:1004563827491

[14] Wang C., Liu C-R.: Transcrystallization of polypropylene composites: Nucleating ability of fibres. Polymer, **40**, 289–298 (1999).
DOI: 10.1016/S0032-3861(98)00240-7

[15] Sun X. L., Li H., Lieberwirth I., Yan S.: α and β interfacial structures of the iPP/PET matrix/fiber systems. Macromolecules, **40**, 8244–8249 (2007).
DOI: 10.1021/ma071382x

[16] Li H., Zhang X., Duan Y., Wang D., Li L., Yan S.: Influence of crystallization temperature on the morphologies of isotactic polypropylene single-polymer composite. Polymer, **45**, 8059–8065 (2004).
DOI: 10.1016/j.polymer.2004.09.032

[17] Li H., Jiang S., Wang J., Wang D., Yan S.: Optical microscopic study on the morphologies of isotactic polypropylene induced by its homogeneity fibers. Macromolecules, **36**, 2802–2807 (2003).
DOI: 10.1021/ma034062w

[18] Wang S-W., Yang W., Bao R-Y., Wang B., Xie B-H., Yang M-B.: The enhanced nucleating ability of carbon nanotube-supported β-nucleating agent in isotactic polypropylene. Colloid and Polymer Science, **288**, 681–688 (2010).
DOI: 10.1007/s00396-010-2194-x

[19] Kawai T., Iijima R., Yamamoto Y., Kimura T.: Crystal orientation of β-phase isotactic polypropylene induced by magnetic orientation of *N,N′*-dicyclohexyl-2,6-naphthalenedicarboxamide. Polymer, **43**, 7301–7306 (2002).
DOI: 10.1016/S0032-3861(02)00690-0

[20] Khanna Y. P.: Rheological mechanism and overview of nucleated crystallization kinetics. Macromolecules, **26**, 3639–3643 (1993).
DOI: 10.1021/ma00066a024

[21] Kotek J., Raab M., Baldrian J., Grellmann W.: The effect of specific β-nucleation on morphology and mechanical behavior of isotactic polypropylene. Journal of Applied Polymer Science, **85**, 1174–1184 (2002).
DOI: 10.1002/app.10701

[22] Dai K., Xu X-B., Li Z-M.: Electrically conductive carbon black (CB) filled in situ microfibrillar poly(ethylene terephthalate) (PET)/polyethylene (PE) composite with a selective CB distribution. Polymer, **48**, 849–859 (2007).
DOI: 10.1016/j.polymer.2006.12.026

[23] Xiao W., Wu P., Feng J.: Effect of β-nucleating agents on crystallization and melting behavior of isotactic polypropylene. Journal of Applied Polymer Science, **108**, 3370–3379 (2008).
DOI: 10.1002/app.27997

[24] Varga J.: β-modification of polypropylene and its two-component systems. Journal of Thermal Analysis and Calorimetry, **35**, 1891–1912 (1989).
DOI: 10.1007/BF01911675

[25] Menyhárd A., Varga J.: The effect of compatibilizers on the crystallisation, melting and polymorphic composition of β-nucleated isotactic polypropylene and polyamide 6 blends. European Polymer Journal, **42**, 3257–3268 (2006).
DOI: 10.1016/j.eurpolymj.2006.09.003

[26] Turner Jones A., Aizlewood J. M., Beckett D. R.: Crystalline forms of isotactic polypropylene. Die Makromolekulare Chemie, **75**, 134–158 (1964).
DOI: 10.1002/macp.1964.020750113

[27] Luo F., Geng C., Wang K., Deng H., Chen F., Fu Q., Na B.: New understanding in tuning toughness of β-polypropylene: The role of β-nucleated crystalline morphology. Macromolecules, **42**, 9325–9331 (2009).
DOI: 10.1021/ma901651f

[28] Varga J., Karger-Kocsis J.: The difference between transcrystallization and shear-induced cylindritic crystallization in fibre-reinforced polypropylene composites. Journal of Materials Science Letters, **13**, 1069–1071 (1994).
DOI: 10.1007/BF00277042